



MONASH University

**Understanding precipitation over the Southern Ocean through
observations and high resolution simulations at Macquarie Island**

Zhan Wang

Mathematical Sciences General

A thesis submitted for the degree of Doctor of Philosophy at

Monash University in 2016

School of Earth, Atmosphere and Environment

Copyright notice

© Zhan Wang 2016

I certify that I have made all reasonable efforts to secure copyright permissions for third-party content included in this thesis and have not knowingly added copyright content to my work without the owner's permission.

Abstract

This thesis presents analyses of the historic surface precipitation and other relevant meteorological records observed at Macquarie Island (MAC). A basic climatology of the surface precipitation (frequency and intensity) is built and compared against a reanalysis model (ERA-I) and satellite products (CloudSat). The relationship between the precipitation and the synoptic meteorology is explored. The orographic effects of the island are studied by high-resolution numerical simulations.

Macquarie Island (54.50 °S, 158.94 °E) is an isolated island with modest orography in the midst of the Southern Ocean with precipitation records dating back to 1948. These records are of particular interest due to the relatively large biases in the energy and water budgets commonly found in climate simulations and reanalysis products over the region. The surface precipitation is presented and compared against the ERA-I reanalysis. The annual ERA-I precipitation (953 mm) is found to underestimate the annual MAC precipitation (1023 mm) by 6.8 % from 1979 to 2011.

The frequency of the 3-h surface precipitation (MAC) is 36.4 % from 2003 to 2011. Light precipitation ($0.066 \leq P < 0.5 \text{ mm hr}^{-1}$) dominates this precipitation (29.7 %), while the heavy precipitation ($P \geq 1.5 \text{ mm hr}^{-1}$) is rare (1.1 %). Drizzle ($0 < P < 0.066 \text{ mm hr}^{-1}$) is commonly produced by ERA-I (43.9 %), but is weaker than the detectable threshold of MAC.

Warm rain intensity and frequency from CloudSat products were compared with those from MAC. These CloudSat products also recorded considerable drizzle (under the detectable threshold of MAC) at frequencies of 16%-30%, but the frequencies were not significantly different than MAC when $P \geq 0.5 \text{ mm hr}^{-1}$.

Heavy precipitation events were, in general, more commonly associated with fronts and cyclonic lows. Some heavy precipitation events were found to arise from weaker fronts and lows that were not adequately represented in the reanalysis products. Yet other heavy precipitation events were observed at points/times not associated with either fronts or cyclonic lows. Two case studies are employed to further examine this.

High-resolution numerical simulations (Weather Research/Forecasting Model: WRF) with and without terrain have been used to identify orographic effects for four cases representing common synoptic patterns at Macquarie Island, namely a cold front, a warm front, post-frontal drizzle, and a mid-latitude cyclone. Results show that clouds and precipitation can readily be perturbed by the island with the main enhancement of precipitation normally in the lee in accordance with a large Froude number flow. Overall the orographic effect on the precipitation record is not found to be significant, except for the enhancement of drizzle found in southwesterly winds.

Given the strong winds over the Southern Ocean and the shallow height of the island, the 3-D Froude number is found to be greater than one in most of the soundings (93.5%). Boundary layer flow commonly passes over the island with the greatest impact on the lee. For the 2-D cross wind flow, the frequency of the Froude number larger than one reduces to 83.7%.

Declaration

This thesis contains no material which has been accepted for the award of any other degree or diploma at any university or equivalent institution and that, to the best of my knowledge and belief, this thesis contains no material previously published or written by another person, except where due reference is made in the text of the thesis.



Signature:

Print Name: ...Zhan Wang.....

Date:9/20/2016.....

Publications during enrolment

Wang, Zhan, Danijel Belusic, Yi Huang, Steven T. Siems and Michael J. Manton, "Understanding orographic effects on surface observations at Macquarie Island", *Journal of Applied Meteorology and Climatology*, accepted.

Wang, Zhan, Steven T. Siems, Danijel Belusic, Michael J. Manton and Yi Huang. "A Climatology of the Precipitation over the Southern Ocean as Observed at Macquarie Island." *Journal of Applied Meteorology and Climatology* **54**. 12 (2015): 2321-2337, doi: 10.1175/JAMC-D-14-0211.1.

Thesis including published works declaration

I hereby declare that this thesis contains no material which has been accepted for the award of any other degree or diploma at any university or equivalent institution and that, to the best of my knowledge and belief, this thesis contains no material previously published or written by another person, except where due reference is made in the text of the thesis.

This thesis includes 1 original papers published in peer reviewed journals and 1 submitted publications. The core theme of the thesis is understanding precipitation over the Southern Ocean through observations and high resolution simulations at Macquarie Island. The ideas, development and writing up of all the papers in the thesis were the principal responsibility of myself, the student, working within the Monash University under the supervision of Steven Siems.

The inclusion of co-authors reflects the fact that the work came from active collaboration between researchers and acknowledges input into team-based research.

In the case of Chapter 2, 3, 4 and 5 my contribution to the work involved the following:

| Thesis Chapter | Publication Title | Status | Nature and % of student contribution | Co-author name(s) Nature and % of Co-author's contribution* | Co-author(s), Monash student Y/N* |
|----------------|---|-----------|--------------------------------------|---|-----------------------------------|
| 2 and 3 | A Climatology of the Precipitation over the Southern Ocean as Observed at Macquarie Island. | Published | 30%. <i>Collecting data</i> | 1) Steven Siems, Concept and writing first draft, 40% 2) Danijel Belusic Concept, 20% 3) Michael Manton Revision opinion, 5% 4) Yi Huang input into manuscript, 5% | No |

| | | | | | |
|---------|--|----------|--|---|----|
| 4 and 5 | Understanding orographic effects on surface observations at Macquarie Island | Accepted | 40%. Concept and collecting data and writing first draft | 1) Danijel Belusic concept 15% 2) Yi Huang, input into manuscript 10% 3) Steven Siems, concept and input into manuscript 30% 4) Michael Manton, Revision opinion, 5% | No |
|---------|--|----------|--|---|----|

I have renumbered sections of submitted or published papers in order to generate a consistent presentation within the thesis.

Student signature: 

Date: 9/20/2016

The undersigned hereby certify that the above declaration correctly reflects the nature and extent of the student's and co-authors' contributions to this work. In instances where I am not the responsible author I have consulted with the responsible author to agree on the respective contributions of the authors.

Main Supervisor signature: 

Date: 9/26/2016

Acknowledgments

I would firstly like to thank my supervisors, Steven Siems, Danijel Belusic and Yi Huang for the guidance, enthusiasm, encouragement and support during my candidature. This thesis certainly wouldn't have been possible without their insightful comments and suggestions along the way.

Thanks also to Michael Manton, who is the coauthor of our two papers during my candidature.

Thanks also go to Thomas Chubb, Luke Hande, Gareth Berry, and all my friends and colleagues at Monash University, who have provided support, both technically and socially, during my candidature.

Thanks also to John Haynes, who directed us on the CloudSat products.

My friends and family have been a constant source of love and support, always encouraging and never doubting. This thesis is dedicated to you.

Contents

| | |
|--|-----|
| Figure Captions..... | xi |
| Table Captions..... | xiv |
| Table of abbreviations | xv |
| 1. Introduction | 1 |
| 1.1. Unique features of the climate over the Southern Ocean | 1 |
| 1.2. Past field campaigns over the SO | 5 |
| 1.3. Satellite observations on precipitation over the SO | 8 |
| 1.4. Studies on Macquarie Island..... | 10 |
| 1.5. Model simulations of precipitation in the Southern Ocean | 13 |
| 1.6. Aims of this study..... | 16 |
| 2. A climatology of the precipitation over the Southern Ocean | 18 |
| 2.1. The atmospheric environment around Macquarie Island | 18 |
| 2.2. Macquarie Island and the weather observation station | 19 |
| 2.3. Observational datasets | 19 |
| 2.3.1. Macquarie island surface observations | 19 |
| 2.3.2. ERA-Interim precipitation products | 20 |
| 2.3.3. CloudSat precipitation products | 20 |
| 2.4. Scale and sampling aspects | 22 |
| 2.5. The seasonal cycle and annual trend of Macquarie Island precipitation | 26 |
| 2.6. The frequency and intensity of precipitation | 27 |
| 2.7. Wind roses, precipitation roses and Ekman spirals | 33 |

| | | |
|--------|---|-----|
| 2.8. | Summary | 36 |
| 3. | Precipitation and fronts..... | 39 |
| 3.1. | Identification of fronts and lows | 39 |
| 3.2. | Statistics of frontal and non-frontal precipitation..... | 43 |
| 3.3. | Selection of case studies..... | 47 |
| 3.3.1. | A case study of strong precipitation with a warm front..... | 47 |
| 3.3.2. | A case study of strong precipitation with a high system | 51 |
| 3.4. | Summary | 55 |
| 4. | Orographic effects on precipitation and atmospheric structure over Macquarie Island | 57 |
| 4.1. | The orographic effects on precipitation..... | 57 |
| 4.2. | Numerical simulations of over the SO | 59 |
| 4.3. | WRF model setup | 59 |
| 4.4. | Selection of case studies..... | 62 |
| 4.4.1. | A cold front case..... | 64 |
| 4.4.2. | A warm Front case | 78 |
| 4.4.3. | A drizzle case..... | 90 |
| 4.4.4. | A cyclone case | 100 |
| 4.5. | Summary | 105 |
| 5. | An Analysis of the Froude number over Macquarie Island..... | 108 |
| 5.1 | Definitions of 2-D and 3-D Froude number | 108 |
| 5.2 | The Froude number of the four case studies..... | 110 |
| 5.3 | A climatology of the Froude number..... | 111 |
| 5.4 | Summary..... | 114 |

| | | |
|------|---|-----|
| 6. | Conclusions | 116 |
| 6.1. | A climatology of the precipitation over the Southern Ocean..... | 116 |
| 6.2. | WRF simulations on the orographic effects of Macquarie Island | 119 |
| 6.3. | Future directions | 121 |
| | References | 123 |

Figure Captions

| | |
|--|----|
| Figure 1.1. The seasonal cycle of the SH storm track..... | 2 |
| Figure 1.2. The location of Macquarie Island | 11 |
| Figure 1.3. The terrain of Macquarie Island and the location of the ABoM station..... | 11 |
| Figure 2.1. The average monthly precipitation from MAC and ERA-I | 27 |
| Figure 2.2. Probability distribution function of warm-rain only intensity | 30 |
| Figure 2.3. Scatter plot of rain rates from MAC and two CloudSat products | 32 |
| Figure 2.4. The wind roses over Macquarie Island. | 34 |
| Figure 2.5. The precipitation rose over Macquarie Island | 35 |
| Figure 2.6. The wind rose showing the differences between the ERA-I and MAC..... | 36 |
| Figure 3.1. 2-month time series (July-August, 2002) of the identified fronts and lows | 42 |
| Figure 3.2. The decomposition of precipitation intensities..... | 44 |
| Figure 3.3. The percentage of the precipitation in the frontal window time..... | 45 |
| Figure 3.4. The percentage of the precipitation associated with fronts | 46 |
| Figure 3.5. Case study A over Macquarie Island on 16 March, 2008 | 49 |
| Figure 3.6. Case study B over Macquarie Island on 01 November, 2010 | 53 |
| Figure 4.1. WRF domains used in this study | 61 |
| Figure 4.2. The MSLP showing a cold front passing Macquarie Island | 64 |
| Figure 4.3. The surface weather records (MAC) and WRF simulations with and without terrain for the cold front case | 65 |
| Figure 4.4. The cloud top temperature from MODIS for the cold front case | 66 |
| Figure 4.5. The Skew-T chart for the cold front case | 67 |
| Figure 4.6. The precipitation and surface wind fields for the cold front case | 71 |
| Figure 4.7. Cross sections from the WRF simulations for the cold front case | 73 |

| | |
|--|-----|
| Figure 4.8. The vertical wind profile for the cold front case | 74 |
| Figure 4.9. The cloud top temperature over Macquarie Island for the cold front case | 76 |
| Figure 4.10. The horizontal (a) and vertical (b) wind field from the simulation at 23:20 UTC 9 October, 2008 | 77 |
| Figure 4.11. 2 m temperature (a) and MSLP (b) for the warm front case | 79 |
| Figure 4.12. The cloud top temperature from MODIS in the warm front case | 80 |
| Figure 4.13. The Skew-T chart for the warm front case | 81 |
| Figure 4.14. The surface weather records (MAC) and WRF simulations with and without terrain for the warm front case | 83 |
| Figure 4.15. The precipitation and surface wind fields from WRF simulations for the warm front case | 85 |
| Figure 4.16. Cross sections from the WRF simulations for the warm front case..... | 87 |
| Figure 4.17. The vertical wind speed for the warm front case..... | 88 |
| Figure 4.18. The vertical wind profile for the cold front case | 89 |
| Figure 4.19. MSLP for the drizzle case..... | 91 |
| Figure 4.20. The Skew-T chart for the drizzle case | 92 |
| Figure 4.21. The surface weather records (MAC) and WRF simulations with and without terrain for the drizzle case | 93 |
| Figure 4.22. The precipitation from 100 m WRF simulations for the drizzle case | 95 |
| Figure 4.23. The precipitation and surface wind fields from 1 km WRF simulations for the drizzle case | 96 |
| Figure 4.24 MODIS IR for the drizzle case..... | 97 |
| Figure 4.25. The vertical wind speed and sea surface temperature for the drizzle case | 98 |
| Figure 4.26. The cross-section of liquid water mixing ratio for the drizzle case | 99 |
| Figure 4.27. The vertical wind profile for the cold front case | 100 |

| | |
|--|-----|
| Figure 4.28. MSLP for the cyclone case | 101 |
| Figure 4.29. The Skew-T chart for the cyclone case | 102 |
| Figure 4.30. The surface weather records (MAC) and WRF simulations with and without terrain for the cyclone case | 103 |
| Figure 4.31. The precipitation from 1 km WRF simulations in the warm air mass | 104 |
| Figure 4.32. The precipitation from 1 km WRF simulations in the cold air mass | 105 |
| Figure 5.1. The Probability Density Function of the Froude number | 112 |
| Figure 5.2. The pie chart diagram showing the frequency of encounter winds from different sectors with and without precipitation | 114 |

Table Captions

| | |
|--|-----|
| Table 2.1 Instruments of the MAC surface observations..... | 20 |
| Table 2.2. The frequency of the thermodynamic state of precipitation from the radar columns in the CloudSat product..... | 25 |
| Table 2.3. The frequency of the thermodynamic state of the precipitation within a segment in the CloudSat product..... | 25 |
| Table 2.4. The precipitation intensity for 3-h MAC and ERA-I..... | 29 |
| Table 2.5 Contingency table of precipitation occurrences using the CloudSat PC product and surface observations (MAC)..... | 31 |
| Table 2.6 Contingency table of precipitation occurrences using the CloudSat RP product and surface observations (MAC)..... | 32 |
| Table 3.1. Counting table for two frontal identifying algorithms..... | 42 |
| Table 3.2. Hourly precipitation records from Macquarie Island for 2010 case study. | 55 |
| Table 4.1. A summary of WRF simulated cases..... | 63 |
| Table 5.1. Froude numbers in the case studies..... | 111 |

Table of abbreviations

| | |
|-------------|---|
| AAD | Australian Antarctic Division |
| ABoM | Australian Bureau of Meteorology |
| ACCESS | Australian Community Climate and Earth-System Simulator |
| ACE-1 | First Aerosol Characterization Experiment |
| ACRE | Antarctic Clouds and Radiation Experiment |
| AIRS | Atmospheric Infrared Sounder |
| ASP | Adams (2009) Surface Pressure frontal identification method |
| ASTEX | Atlantic Stratocumulus Transition Experiment |
| BRJ | Berry, Reeder and Jakob (2011) frontal identification method |
| CALIOP | Cloud-Aerosol Lidar with Orthogonal Polarization |
| CALIPSO | Cloud-Aerosol Lidar and Infrared Pathfinder Satellite Observations |
| CAPE | Convective Available Potential Energy |
| CCN | Cloud Condensation Nuclei |
| c.i. | contour interval |
| CIN | Convective Inhibition |
| CPR | The Cloud Profiling Radar |
| DARDAR-MASK | raDAR/liDAR-MASK |
| DEEPWAVE | Deep Propagating Gravity Wave Experiment |
| D_p | aerosol diameter |
| DPR | Dual-frequency Precipitation Radar |
| ECMWF | European Centre for Medium Range Weather Forecasts |
| ERA-I | ECMWF Re-Analysis Interim |
| FIRE 1 | First International Satellite Cloud Climatology Project Regional Experiment |
| Fr | Froude number |
| GLOMA | Global Model of Aerosol Processes |
| GPCP | Global Precipitation Climatology Project |
| GPM | Global Precipitation Measurement |
| H | mountain height |
| HIAPER | High-Performance Instrumented Airborne Platform for Environmental Research |
| IFS | Integrated Forecasting System |
| ISCCP | International Satellite Cloud Climatology Project |
| ITCZ | Intertropical Convergence Zone |

| | |
|----------|---|
| JAXA | Japan Aerospace Exploration Agency |
| L | Latent heat of condensation of water |
| LES | Large-Eddy Simulation |
| LFC | Level of Free Convection |
| MAC | Macquarie Island |
| MERRA | Modern-Era Retrospective Analysis for Research and Applications |
| MISR | Multangle Imaging Spectroradiometer |
| MODIS | Moderate Resolution Imaging Spectro radiometer |
| MSLP | Mean Sea Level Pressure |
| MSP | Multiple variables with Surface Pressure frontal identification method |
| N | Brunt-Väisälä frequency |
| NASA | National Aeronautics and Space Administration |
| NCAR | National Center for Atmospheric Research |
| NCEP | National Center for Environmental Prediction |
| NFS | National Science Foundation |
| NOAA | National Oceanic and Atmospheric Administration |
| NWP | numerical weather predictio |
| P | Precipitation rate |
| PBL | Planetary Boundary Layer |
| PC | CloudSat 2C - COLUMN - PRECIP (R04) products |
| PDF | Probability Density Function |
| qs | saturation mixing ratio |
| qw | total water mixing ratio |
| R | ideal gas constants for dry air |
| RANS | Reynolds-Averaged Navier-Stokes equation |
| RP | 2C-RAIN-PROFILE (R04) |
| RRTMG | Rapid Radiative Transfer Model for GCMs |
| SLW | Supercooled Liquid Water |
| SO | Southern Ocean |
| SOCEX | Southern Ocean Cloud Experiment |
| SOCRATES | Southern Ocean Cloud Radiation and Aerosol Transport Experimental Studies |
| SRTM | Shuttle Radar Topography Mission |
| T | Temperature |
| TIROS | Television Infrared Observation Satellite |
| TRMM | Tropical Rainfall Measuring Mission |

| | |
|-------------|------------------------------------|
| U | cross mountain wind speed |
| UASs | Unmanned Aerial Systems |
| UTC | Coordinated Universal Time |
| WRF | Weather Research/Forecasting Model |
| YOTC | Year of Tropical Convection |
| YSU | Yonsei University |
| Ze | radar reflectivity |
| Γ | moist adiabatic lapse rate |
| γ | mountain horizontal aspect ratio |
| ξ_{250} | 250-hPa vorticity |

1. Introduction

1.1. Unique features of the climate over the Southern Ocean

The Southern Ocean (SO) stretches from the edge of Antarctica to $\sim 50^\circ$ S, covering a vast area, 15% of earth surface. The weather over the SO is mainly driven by mid-latitude cyclones and their associated frontal systems, which are responsible for much of the variability in the atmosphere over the SO (Trenberth, 1991). Using the 6-hourly National Center for Environmental Prediction–National Center for Atmospheric Research (NCEP–NCAR) global reanalysis spanning the period of 1958–97, Simmonds and Keay (2000) studied the SO storm tracks and found that the most intense region was located to the south of 60° S in all seasons and in the Indian and West Pacific Ocean sectors in autumn and winter. Hoskins and Hodges (2005) studied the SO storm tracks through an analysis of the Eulerian variances of time-filtered fields for a variety of upper and lower tropospheric variables based on the 40-yr European Centre for Medium Range Weather Forecasts (ECMWF) Re-Analysis (ERA-40) data (Uppala et al. 2005). They found that in summer, a single, circular, strong storm track was commonly present between 40° S and 60° S (Figure 1.1a), whereas in winter, the storm track was more asymmetric with a spiral around the Antarctica and an outer spiral in the sector of the strong subtropical jet (Figure 1.1b).

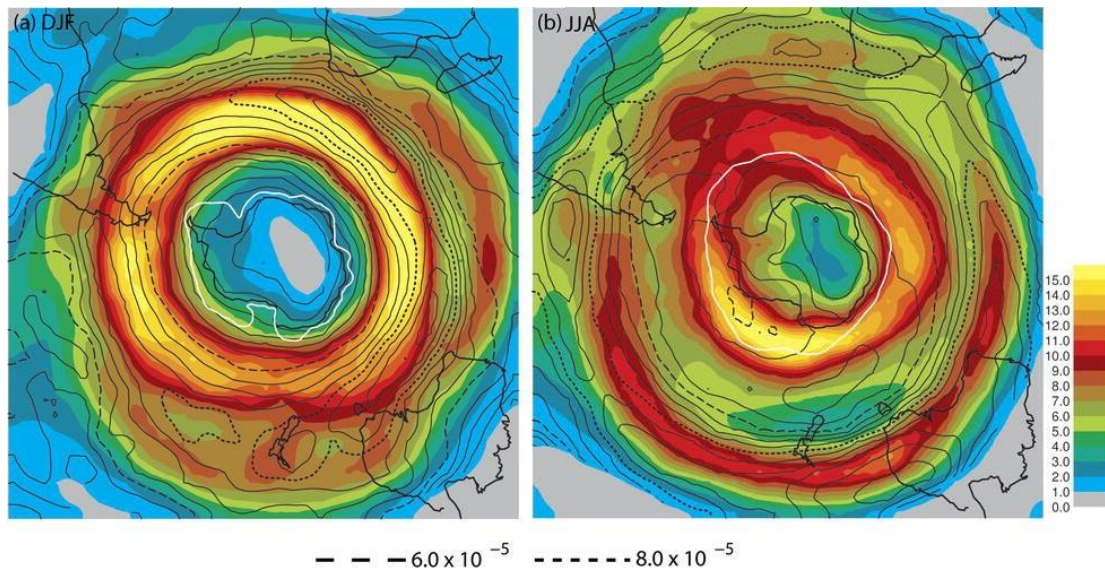


Figure 1.1. Upper-tropospheric seasonal cycle of the SH storm track based on 250-hPa vorticity (ξ_{250}): track density (color) and mean intensity (line contour) for (a) DJF (summer), (b) JJA (winter). Track density is number density per month per unit area, and mean intensity is absolute relative to removed background with contour interval (c.i. = 0.5×10^{-5}). The 50% sea ice boundary is delineated by the white line for each season.

Due to the absence of land, the moist marine environment makes the SO a region with the largest fractional cloud cover on earth (Mace et al. 2007), as well as the most frequent precipitation over the global oceans (Ellis et al. 2009). Bennartz (2007) analysed two and a half year observations from Moderate Resolution Imaging Spectro radiometer (MODIS, Platnick et al. 2003) and found up to 90% of the liquid water clouds were likely to be precipitating over the SO.

The region in the middle of SO, known as the ‘furious 50’s’ has the strongest annually-averaged mean wind speed on earth (Vinoth and Young 2011). Strong winds produce large waves that, when coupled together, generate sea spray

(Murphy et al. 1998; Jennings et al. 1998). Korhonen et al. (2010) employed the ERA-40 reanalyses to find the acceleration of the westerly jet over the SO from the early 1980s. This increase in wind speed would lead to a higher sea spray flux, resulting in a 22% increase of Cloud Condensation Nuclei (CCN) concentrations between 50 and 65°S from the Global Model of Aerosol Processes (GLOMAP; Mann et al. 2010) simulations (Spracklen et al. 2005).

Various satellite observations of the cloud-top thermodynamic phase including MODIS, raDAR/liDAR (DARDAR-MASK; Delanoë and Hogan 2010) and Cloud-Aerosol Lidar and Infrared Pathfinder Satellite Observations (CALIPSO; Hu et al. 2009) suggest that clouds composed of supercooled liquid water (SLW) are dominant over the SO (Morrison et al. 2011; Huang et al. 2012a). This feature is significantly different from that over the North Atlantic, where glaciation is more prevalent (Huang et al. 2015). The space borne observations are further supported by limited in-situ measurements, where SLW has been detected throughout the entire depth of clouds that were often hundreds of meters thick (Chubb et al. 2013; Morrison et al. 2010; Ryan and King 1997). Chubb et al. (2013) further found that the precipitation under the SLW clouds (cloud-top temperature down to -22 °C) was in various thermodynamic phases (glaciated, mixed-phase or even entirely supercooled liquid), highlighting our very limited understanding of the nature of precipitation over the SO. Understanding the phase of precipitation over the SO is a challenge for satellite observation and reanalyse simulations.

Cloud condensation nuclei (CCN) are sparse in a pristine marine boundary layer, but are substantially greater downwind of a continent. Hudson and Xie (1999)

analysed more than 80 hours airborne CCN measurements in the First International Satellite Cloud Climatology Project (ISCCP) Regional Experiment (FIRE 1) in the northeast Pacific and the Atlantic Stratocumulus Transition Experiment (ASTEX) and found that the CCN concentration in the Northern Hemisphere was enhanced by a factor of 5 near the continent and this enhancement could extend 1500 km from land over the oceans. Kanitz et al. (2011) employed an aerosol lidar aboard the research vessel Polarstern, cruising over the Atlantic between 50°N and 50°S in 2009 and 2010, and found less anthropogenic aerosols in the southern hemisphere than in the northern hemisphere. Hudson and Xie (1998) studied the airborne observations over the SO during the First Aerosol Characterization Experiment (ACE-1; Bates et al. 1998a) and found that CCN concentrations were affected by proximity to land. They also found that the warmer sea surface at the lower latitudes generally produced more dimethyl sulphide as a source of CCN. Besides the geographical variability, the CCN concentration also has large seasonal variability over the SO (Gras 1995). Yum and Hudson (2004) analysed data from 10 Southern Ocean Cloud Experiment (SOCEX) I flights and 8 SOCEX II flights off the west coast of Tasmania and found that the average summertime CCN concentration was more than a factor of 5 higher than wintertime for all ranges in the clean maritime (baseline) environment characteristic of the Southern Ocean.

Charlson et al. (1987) hypothesized that the marine biogenic dimethyl sulphide accounts for the formation of CCN in the remote marine boundary layer. This hypothesis is referred to as the CLAW hypothesis, which also includes climate regulation of cloud albedo, radiation and sea surface temperature as

consequences after the changes of the concentration of CCN, as well as the climate feedback to dimethyl sulphide emissions from phytoplankton. This hypothesis has largely been supported by the sulphur-driven seasonal CCN cycle observed at Cape Grim, Tasmania (Ayer and Gras 1991; Ayer et al. 1997). However, dimethyl sulphide emission is not the only source of remote marine boundary layer CCN; organic aerosol particles derived from phytoplankton and other organics in the ocean surface have also been widely found in marine boundary layer (O'Dowd et al 2004; Bigg 2007). It was hypothesized that they are injected into the atmosphere through bubble bursting on the sea surface (Facchini et al. 2008; Leck and Bigg 2005). Quinn and Bates (2011) reviewed studies in the past two decades on verifying the CLAW hypothesis, including observations in the marine boundary layer, laboratory studies and model simulations, and argued that the CLAW hypothesis should be retired because the composition of marine boundary layer CCN is more complex than just atmospheric sulphur, and the biota-climate regulation driven by atmospheric sulphur is not dominant in both observation and simulation results.

1.2 Past field campaigns over the SO

Our understanding of clouds and precipitation over the SO is limited due, to a significant degree, to sparse observations in this region. In-situ observations of the atmosphere over the SO are rare due to its remote location and harsh operating conditions, and have generally been limited to relatively sparse, isolated field campaigns.

ACE-1 (Bates et al. 1998a) in November and December of 1995 was the first of a

series of experiments quantifying the chemical, physical, radiative, and cloud nucleating properties of maritime aerosol (Bates et al. 1998a). The aerosol number size distribution from 5 to 10000 nm diameter (D_p) were observed on a National Oceanic and Atmospheric Administration (NOAA) ship *Discoverer* in the lower marine boundary layer south of Tasmanian (Bates et al. 1998b), and found:

- (i) The background marine boundary layer aerosol includes four distinct modes: an ultrafine mode ($D_p = 5\text{--}20$ nm), an Aitken mode ($D_p = 20\text{--}80$ nm), an accumulation mode ($D_p = 80\text{--}300$ nm), and a coarse mode ($D_p > 300$ nm).
- (ii) The ultrafine mode particles are produced in the free troposphere or upper boundary layer and mixed down into the lower boundary layer during convective mixing associated with cloud pumping and cold frontal passages.
- (iii) Long term increasing of oceanic emissions of dimethyl sulfide accounts for the mean diameter growth of the Aitken and accumulation mode particles.
- (iv) Coarse mode particles are comprised primarily of sea salt, but the instantaneous wind speed can only explain one third of the variance in the coarse mode number concentration in the observed marine boundary layer.
- (v) Anthropogenic influences are minimal in background conditions. As a result, maximum cloud droplet concentrations ranged between 45 and 200 cm^{-3} .

SOCEX I & II (Boers et al. 1996; Boers and Krummel 1998) observed the microphysical and radiative properties of stratocumulus in the pristine background region over the SO and found:

- (i) The typical values of the cloud droplet concentration are $\sim 100 \text{ cm}^{-3}$ and $\sim 200 \text{ cm}^{-3}$ for maritime and continental clouds (Gultepe and Isaac, 2004), while the average cloud droplet concentration near cloud base over the SO is normally less than 50 cm^{-3} in the austral winter, due to the absence of CCN.
- (ii) Drizzle formation reduces cloud albedo and optical depth during the droplet coalescence process.
- (iii) The cloud droplet effective radius recorded is among the highest ever reported as a consequence of the low cloud droplet concentration.
- (iv) The summertime droplet concentration is about three times that in wintertime, while the effective radius in winter is about 42% larger than that in the summertime.

During ACE-1 (Bates et al. 1998a) and SOCEX I & II (Boers et al. 1996; Boers and Krummel 1998), a multiple layer atmosphere structure in the lower troposphere was commonly observed. As reported by Russell et al. (1998), during ACE-1 a well-defined boundary layer driven by wind shear was recorded to the height of 500–700 m, with an inversion in both moisture and temperature observed at approximately 1900 m marking the free troposphere. Between them resided a layer with intermittent turbulence and cloud cover, which was defined as a 'buffer layer'. This multiple layer structure was also found in SOCEX II (Boers et

al. 1998): a 'mixed layer' below the height of 920 hPa, an 'intermediate layer' between 920 and 890 hPa, and a 'stratiform layer' from 890 to 860 hPa (Jensen et al. 2000). They also found wind speeds in this 'buffer layer' were less than those in the underlying mixed layer and the overlying free troposphere. The wind shear, vertical temperature gradient and mixing ratio gradient across the 'buffer layer' were also remarkable.

In recent years, the HIAPER (High-Performance Instrumented Airborne Platform for Environmental Research) Pole-to-Pole Observations (HIPPO) (Wofsy 2011) made in-situ observations over the SO in different seasons between 2009 and 2011 that included basic cloud microphysics observations. Chubb et al. (2013) found high quantities of SLW in different seasons and different meteorological conditions over the SO. Chubb et al. (2016) found exceptionally high (100–200 cm^{-3}) cloud droplet number concentrations between 55°S and 60°S over the SO, in wintertime, which cannot be explained by neither the long-range transport of continental aerosol, nor dimethyl sulfide emission from the ocean surface (SOCEX II, Boers et al. 1998). Sea spray aerosol may explain the elevated aerosol concentrations in the winter, which still need to be examined by a compositional analysis of the aerosol. Although there have been isolated field projects conducted in the past decade, the lack of cloud-targeting strategies and long term observations have limited our knowledge on the microphysics over the SO.

1.3. Satellite observations on precipitation over the SO

The Global Precipitation Climatology Project (GPCP) includes multiple precipitation and precipitation-related products in monthly time scale from 1979

(Adler et al. 2003) and daily time scale from 1996 (Huffman et al. 1997). The Television Infrared Observation Satellite (TIROS) Operational Vertical Sounder (TOVS) sounding data, with a transition to the Atmospheric Infrared Sounder (AIRS) are primary data sets used for the high latitude ocean area such like SO. Yuan and Miller (2002) studied the temporal and spatial variation of precipitation patterns over the global ocean, using the (GPCP) version 2 monthly data set, in a $2.5^{\circ} \times 2.5^{\circ}$ latitude-longitude gridded for the period 1979 to 1999. A strong seasonal cycle of precipitation was observed for the oceans in the Southern Hemispheres. The precipitation in the Southern Hemispheres also varied significantly with latitude, with latitudinal maxima at 56°S , 39°S and 4°S .

A coordinated group of Earth-observing satellites closely follow one after another within seconds to minutes along the same polar orbit (A-Train; Stephens et al. 2002). These near-simultaneous observations from different satellites provide a wide variety of observations for the same atmospheric activity, which can be used to improve our understanding of the cloud and precipitation over the SO. As one of the A-Train satellites, CloudSat is the first satellite with active space-borne sensor that has the capability to observe precipitation over a global scale. The Cloud Profiling Radar (CPR; Stephens et al. 2002) on CloudSat has been the most sensitive sensor to detect light rain and drizzle. Ellis et al. (2009) found from a CPR precipitation product (2C-COLUMN-PRECIP; Haynes et al. 2009) that, globally, the precipitation occurrence was most frequent between 50°S and 60°S , with precipitation fraction in 2C-COLUMN-PRECIP around 40%. Stephens et al. (2010) compared the CPR liquid precipitation product (2C-COLUMN-PRECIP) with that from five different global numerical models and

found that they are largely consistent for the precipitation accumulation over the mid-latitude ocean, but the frequency of precipitation from these models (daily integrated accumulations of precipitation in a model grid) is approximately twice that from CPR, with the mean model intensity lies between 1.3 and 1.9 times less than the averaged observations. Neither the GPCP nor CloudSat products have been verified by in-situ observations for the SO.

1.4. Studies on Macquarie Island

Macquarie Island (54.50°S 158.94°E) is a small, remote island in the midst of the SO (Figure 1.2) with a rich, quality record of both surface and upper air observations that has been maintained by the Australian Bureau of Meteorology (ABoM) and dates back to 1948. Macquarie Island is a north-south oriented narrow island, about 34 km long and 5 km wide (Jovanovic et al. 2012). Most parts of the island are around 100–250 m in elevation, and the highest point of 410 m is in the south (Figure 1.3). The observation station (station number: 300004) is located in the northernmost part of the island on a narrow isthmus at an elevation of 6 m above sea level.

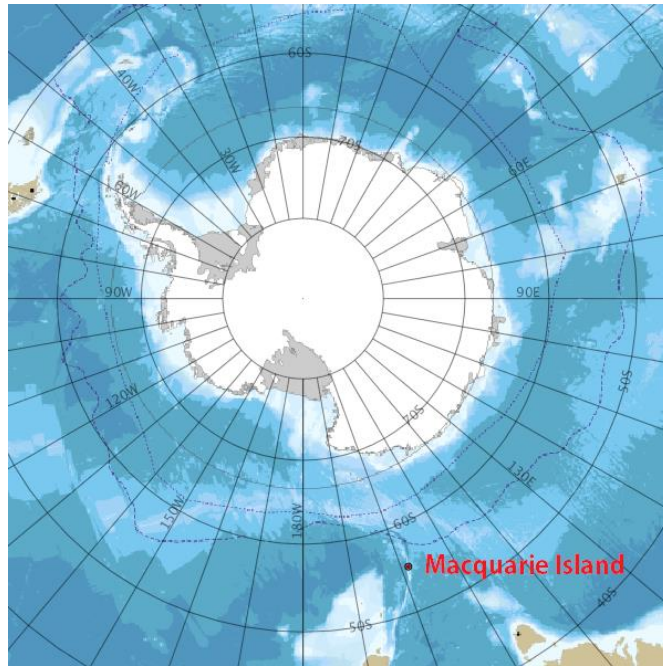


Figure 1.2. Location of Macquarie Island

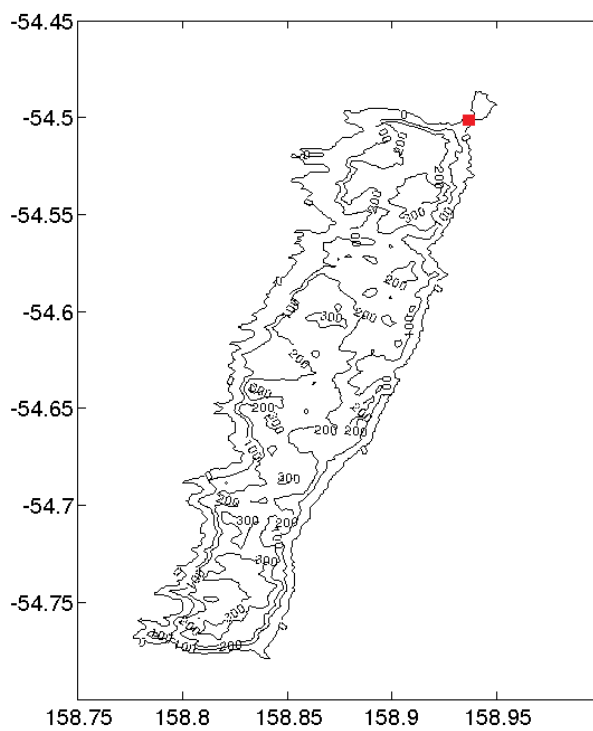


Figure 1.3. The terrain of Macquarie Island, the red point indicates the location of the ABoM station.

In recent years the observations recorded at Macquarie Island have become quite valuable in helping develop an understanding of the meteorology over the SO. For example, Hande et al. (2012a) analysed the thermodynamic structure of the routine upper air soundings to quantify the strong wind shear in the boundary layer over the SO and a corresponding bias in the ECMWF Re-Analysis Interim (ERA-I, Dee et al 2011) product and Year of Tropical Convection (YOTC; Moncrieff et al. 2012) product. They also found that the 'buffer layer' defined by Russell et al (1998) occurs 33.7% of the time in MAC soundings.

Adams (2009) examined the trends in the surface observations highlighting a 35% increase in the annual precipitation over a 38-year period from 1971-2008. Such strong trends were not evident in the ERA-40 reanalysis (Adams 2009). Jovanovich et al. (2012) reported similar trends in precipitation for the station. Adams (2009) went further to highlight a modest increase in the winds over Macquarie Island over this time frame and a corresponding drying of the boundary layer air. Hande et al. (2012b) analyzed the sounding record of MAC from 1991 to 2011, and identified a statistically significant increase in the winds over Macquarie Island of $2.99 \text{ cm s}^{-1} \text{ year}^{-1}$. Over the same period of time the ERA-I reanalysis recorded a decrease of $2.21 \text{ cm s}^{-1} \text{ year}^{-1}$ (Hande et al. 2012b). Huang et al. (2012b) compared the upper air soundings over Macquarie Island against both CloudSat and raDAR/liDAR MASK product, and suggested that the satellite products underestimate the fraction of boundary layer clouds in the lowest kilometer of the boundary layer, due to the surface clutter contamination.

The routine observations over Macquarie Island will be of increasing value for future field activities over the SO, such as the proposed ACRE (The Antarctic

Clouds and Radiation Experiment) and SOCRATES (Southern Ocean Cloud Radiation and Aerosol Transport Experimental Studies) campaign, where additional ground-based observations, including microwave radiometers and surface broadband radiometers, and boundary layer observations from unmanned aerial systems (UASs) have been proposed.

Although a single station may be a limited representation of the meteorology over the SO, Macquarie Island is on the storm track (Streten 1988; Simmonds and Keay 2000), which is an ideal place that experiences variety of synoptic conditions. The station locates in the island of 410 m height and has exposure to the prevailing westerly winds (Hande et al. 2012a). However, it is well appreciated that orography can readily perturb winds, cloud cover and precipitation. With the strong winds and high relative humidity, even modest orography has the potential to create local perturbations to the clouds, precipitation and thermodynamic structure and call into question the reason for observed trends. Thus, any potential orographic effect on measurements over Macquarie Island needs to be further explored and understood.

1.5. Model simulations of precipitation in the Southern Ocean

Currently, our understanding of the clouds over the SO is limited. Large biases in the energy budget in both state-of-the-art reanalyzes and coupled global climate models were found over the SO (Trenberth and Fasullo 2010), resulting from underestimation of cloud albedo and of cloud cover. Previous studies suggest that climate models generally over-estimate the frequencies of drizzle and underestimate the intensities of heavy precipitation events, when compared with

satellite observations (e.g. Franklin et al. 2013; Catto and Nicholls 2013).

These biases in the representation of SO clouds and precipitation affect the simulation of both the regional and global climate. Hwang and Frierson (2013) found that the underestimate of cloud fraction and cloud thickness over the SO leads to an overestimation of the Southern Hemisphere temperature, and subsequently, a southward shift in the tropical precipitation belt. This southward shift can cause the double Intertropical Convergence Zone (ITCZ) bias in the deep tropic, which remains a major error in most state-of-the-art global climate models (Hwang and Frierson 2013).

Bodas-Salcedo et al. (2012) compared cloud properties and radiative fluxes estimates from ISCCP against those in the atmosphere-only version of the Met Office model, and found that low- and mid-level clouds in the cold-air sector of the mid-latitude cyclones are responsible for most of the bias. Naud et al. (2012) compared the SO cloud cover from the Modern-Era Retrospective Analysis for Research and Applications (MERRA; Rienecker et al. 2011) reanalyses against MODIS and the Multiangle Imaging Spectroradiometer (MISR) observations, and found that the dynamic and thermodynamic characteristics of the cyclones were simulated well. They suggested that the bias in the cloud cover was likely caused by the microphysics and/or boundary layer schemes. Huang et al. (2014; 2015) also found low- and mid-level clouds were underestimated in Weather Research/Forecasting Model (WRF; Skamarock et al. 2008) and the Australian Community Climate and Earth-System Simulator (ACCESS) simulations, due to a lack of moisture in the boundary layer. Bodas-Salcedo et al. (2012) recently argued that the under representation of SLW has caused biases in the radiative

simulation over the SO.

Understanding the development of precipitation over the SO remains an open scientific question. The widespread presence of SLW may significantly alter the precipitation processes and could potentially account for the discrepancy between MAC and ERA-40 found by Adams (2009). The development of precipitation can be split into 'warm' and 'cold' microphysical processes. Put simply, in 'warm' clouds, the liquid droplets grow by condensation in a supersaturated environment and then by the collision and coalescence with other cloud droplets. In 'cold' clouds, ice crystals can grow by either the sublimation of vapour or by riming and aggregation. In a supercooled warm rain process, although the temperature is below 0 °C, liquid hydrometeors are produced through a warm rain process, because the available ice nuclei are too few or inactive to create solid hydrometeors at temperatures experienced. The supercooled warm rain process has been observed and simulated in several studies. Rosenfeld et al. (2013) observed supercooled rain in pristine conditions in Alaska and northern California, with extremely low concentrations (0.03L^{-1}) of ice crystals in layer clouds with the temperatures as low as -21°C . Rasmussen et al. (2002) studied the microphysical processes of SLW precipitation using the National Center for Atmospheric Research–Pennsylvania State University Mesoscale Model version 5 model, and suggested that low ice-crystal concentrations ($<0.08\text{ L}^{-1}$) is a necessary condition for drizzle formation. However, our knowledge about ice nuclei, cloud condensation nuclei (CCN) and the formation of the supercooled stratocumulus is still very limited.

Due to its widespread influence and persistent bias, the SO has become a

frontline concern of the climate community to the point where the Geosciences advisory panel to the U.S. National Science Foundation (NFS, 2014) recently identified the atmospheric processes over the SO under one of their four research frontiers. This suggests a pressing need for a better understanding of cloud, aerosol, and precipitation processes in this climatically important region.

1.6 Aims of this dissertation

Precipitation has a significant effect on mid- and low level clouds over the SO, which are responsible for the main bias of water cycle and energy budget in regional and global climate. The precipitation over the SO is also unique, because it may be generated from the clouds composed of SLW with few ice nuclei and a variety of CCN. Hence it is necessary to improve our understanding of the precipitation over the SO. Aims of this study and the rest chapters in this dissertation are listed below:

- Chapter 2: The surface precipitation observed at Macquarie Island is analysed to build a basic climatology of the precipitation over the SO. The frequency and intensity of the precipitation are compared against the reanalysis model (ERA-I) and satellite products (CloudSat) that are commonly employed to evaluate climate and weather simulations.
- Chapter 3: The relationship between precipitation and various synoptic systems (e.g. fronts) over Macquarie Island is explored.
- Chapter 4: Potential orographic effects of the island on the observations are investigated using high-resolution numerical model (WRF)

simulations with and without terrain. Four cases representing typical synoptic situations at Macquarie Island, namely a cold front, a warm front, drizzle, and a mid-latitude cyclone, are investigated.

- Chapter 5: An analysis of Froude number over Macquarie Island is undertaken to further appreciate the potential for orographic forcing at the station.
- Chapter 6: Conclusions

2. A climatology of the precipitation over the Southern Ocean

A climatology of the precipitation over the SO has been built to improve our understanding of the climate and atmospheric processes in this research frontier region. The frequency and intensity of the precipitation observed at Macquarie Island has been analysed and directly compared against CloudSat and ERA-I precipitation products that are relied upon for an understanding and modeling of the SO dynamics, clouds, and precipitation. Much of the work in this chapter has been published in Wang et al. (2015).

2.1. The atmospheric environment around Macquarie Island

The climate of Macquarie Island is moderated by the surrounding ocean, with a weak annual cycle of SST and clouds (Huang et al 2012a). The surface temperature at the station ranges from 1 to 9 °C in July and 5 to 13 °C in January, yet snow is common in winter (Streten 1988). There is no diurnal cycle or sea breeze signature for such a small and narrow island. Most winds are from the west and northwest and the 10 m wind speeds are commonly between 8 to 12 m s⁻¹ since 1970 (Adams 2009). Ekman spirals are common over Macquarie Island, with a frequency of occurrence of 53% from 1995 through to 2011 (Hande et al. 2012b). The circumpolar storm track dominates the climate over the SO (Simmonds and Keay 2000) and brings most of the intense precipitation ($P > 1 \text{ mm hr}^{-1}$) over Macquarie Island. The mid-latitude cyclones or fronts pass across this island approximately every five or six days through the year (Streten 1988), more frequently in the winter and less frequently in the summer.

2.2. Macquarie Island and the weather observation station

Macquarie Island is a north-south oriented narrow island, about 34 km long and 5 km wide (Jovanovic et al. 2012). Most parts of the island are around 100–250 m in elevation, and the highest point of 410 m is in the south (Figure 1.3). An Australian Bureau of Meteorology (ABoM) weather observation station (station number: 300004) has been in operation since 1948 and is maintained by the Australian Antarctic Division (AAD). The station is located in the northernmost part of the island on a narrow isthmus at an elevation of 6 m above sea level, and has exposure to the prevailing westerly winds (Hande et al. 2012a). A ridge of ~200 m height is less than 3 km to the west-southwest of the station. It has a potential to be an upwind barrier for the station in the southwesterly winds. Similarly, an 80 m high hill to the northeast may affect northerly flow.

2.3. Observational datasets

2.3.1. Macquarie island surface observations

Standard surface observations (Table 2.1) are recorded along with twice-daily upper air soundings. Jovanovic et al. (2012) details the metadata of these records from 1950 to 2009 and the quality control measures. For example, rain rates were measured by a rain gauge and regularly compared with the pluviograph records. The precipitation records were tested to be homogeneous by using total cloud amount and sea level pressure, as well as RCLimDex software (Zhang and Yang 2004). The combination of glaciated precipitation (snow/ice) and high winds has the potential to lead to an under reporting of precipitation, particularly during the cold seasons.

| Parameters | Instruments |
|---------------------------------|--|
| Surface air temperature | Dobbie dry bulb mercury thermometer |
| Surface pressure | Vaisala PTB220B barometer |
| Wind speeds and wind directions | An anemometer on 10 m agl |
| Precipitation | Rimco TBRG rain gauge |
| Snow | 203 mm (8in) - 200mm capacity snow gauge |

Table 2.1 Instruments of the MAC surface observations

2.3.2. ERA-Interim products

ERA-Interim (ERA-I) is the latest global atmospheric reanalysis product developed by ECMWF, covering the period from 1979 onwards (Dee et al. 2011). The spatial resolution of the data set is $0.75^{\circ} \times 0.75^{\circ}$ on 60 vertical levels. The gridded data include 3-hourly surface fields and 6-hourly upper-air atmospheric fields. ERA-I provides stratiform and convective precipitation products, as well as the total precipitation record, which is the sum of the stratiform and convective precipitation. The temporal resolution of the ERA-I precipitation data allows for a direct comparison with the hourly MAC surface precipitation records that have been summed to either a 3-hour or 6-hour time interval. Topographical information of Macquarie Island is not included in ERA-I.

2.3.3. CloudSat precipitation products

Prior to the Global Precipitation Measurement (GPM) mission, the CloudSat

Cloud Profiling Radar (CPR; Stephens et al. 2002) onboard the A-Train satellite constellation had been the most sensitive sensor to detect light rain and drizzle. Berg et al. (2010) reported that a significant amount of light rainfall and drizzle over subtropical and mid-latitude oceans was missed by the Tropical Rainfall Measuring Mission (TRMM) but captured by CloudSat. Ellis et al. (2009) employed a CPR precipitation product (2C-COLUMN-PRECIP; Haynes et al. 2009) to study the precipitation frequency over the global oceans; a peak in the frequency of precipitation was observed between 50 °S and 60 °S. Further, they highlighted that at such high latitudes much of the precipitation was actually classified as snow/ice or mixed phase, which brings more uncertainties to the precipitation rate in the satellite observations. Stephens et al. (2010) compared the CPR liquid precipitation product with that from five different global numerical models and found that the time-integrated accumulation was largely consistent for the mid-latitudes (30° N~ 60° N and 30° S~ 60° S) oceans. The frequency of precipitation from these models, however, is approximately twice that from CPR, with the intensity being correspondingly weaker. Mitrescu et al. (2010) details a second CloudSat precipitation product (2C-RAIN-PROFILE), which has a specific focus on quantifying the intensity of light precipitation. An initial climatology found that ‘very light’ precipitation ($0 < P < 1 \text{ mm hr}^{-1}$) was dominant over the SO, commonly with a frequency in excess of 15 %.

The CloudSat precipitation data employed in this study are the 2C-COLUMN-PRECIP (R04) (hereafter PC, Haynes et al. 2009) and 2C-RAIN-PROFILE (R04) (hereafter RP, Mitrescu et al. 2010; Lebsock and L’Ecuyer, 2011) products. The PC product provides the presence, and often intensity, of precipitation derived

from estimates of the path-integrated attenuation (PIA) of the radar signal, which is determined using an empirical relationship between the clear sky surface backscattering cross-section, surface wind speed, sea surface temperature, and atmospheric temperature and moisture profiles over the oceans. Surface rain rate is retrieved by assuming the invariability of vertical rainfall profiles. The more recently developed RP product incorporates the vertical variability of rainwater and drop size distributions, in addition to PIA and the observed reflectivity profiles. In this study we have examined all segments (2007-2010) from the five tracks nearest MAC station. In total 417 segments are analyzed (Note that a battery anomaly within the satellite caused missing data for 40 days in December of 2009 and January of 2010).

2.4. Scale and sampling aspects

The detective threshold of the surface observation on the precipitation at Macquarie Island is 0.2 mm hr^{-1} . Accordingly, at this time scale 'no precipitation' at MAC actually defines a precipitation rate of $(0 \leq P < 0.2 \text{ mm hr}^{-1})$. We define 'light' precipitation as $(0.2 \leq P < 0.5 \text{ mm hr}^{-1})$, 'moderate' precipitation as $(0.5 \leq P < 1.5 \text{ mm hr}^{-1})$ and 'heavy' precipitation as $(1.5 \text{ mm hr}^{-1} \leq P)$, which represents the most extreme events observed at MAC from 2003 to 2011. As other precipitation products over Macquarie Island, like those from a reanalysis product, are not limited by this 0.2 mm hr^{-1} detection threshold, we define 'drizzle' in ERA-I and satellite products a positive quantity of precipitation below the MAC detective threshold $(0 < P < 0.2 \text{ mm hr}^{-1})$.

For comparison purposes, longer time averaging periods (3-h and 6-h) are also examined in this Chapter. The minimum MAC detection rate drops accordingly

(0.066 mm hr⁻¹ and 0.033 mm hr⁻¹, respectively). The definitions of drizzle and light precipitation also shift accordingly. Specifically, when working with 3-h observations, drizzle is defined as ($0 \leq P < 0.066$ mm hr⁻¹) and light precipitation is defined as ($0.066 \leq P < 0.5$ mm hr⁻¹). The definitions of moderate and heavy precipitation are constant throughout this paper.

The temporal and spatial geometry of model products, surface observations and satellite products are vastly different, confounding any direct comparison. The CPR measurement for a single column is approximately 1.1 km along track and 1.3 km wide. The CPR orbit segments analysed here were measured in tens of seconds thus producing a near-instantaneous, one-dimensional cross-section. Precipitation rates used in this study are averages of the precipitation columns along the segments. The ERA-I precipitation product covers a time period of 3 hours and is two-dimensional ($0.75^\circ \times 0.75^\circ$). Stephens et al. (2010) discussed in detail the difficulty in directly comparing CloudSat observations to those from a reanalysis product due to differences in temporal and spatial geometry. A-Train segments of both 1-fold (the model grid length) and 3-fold (3 times of the model grid length) were analyzed to explore the sensitivity of the results to the scaling factor.

One can conceptually employ a mean wind speed over the station to turn the surface observations into a one-dimensional spatial sample. The mean surface wind speed of Macquarie Island was ~ 10 m s⁻¹ from 2003 to 2011, while the wind speed at 900 hPa was ~ 16 m s⁻¹. A 3-h accumulation from the surface MAC observations covers roughly 140 km, which is on the same order of magnitude as these 0.75° and 2.5° A-Train segments. The 3-h MAC records are employed when

comparisons are made with the CloudSat products in this thesis.

The temperature in the CloudSat rainfall profile are retrieved from the ECMWF, which has not enough vertical resolution near the surface to specify the height of freezing level (Haynes et al. 2009). As a result, it is difficult to interpret the melting rate of any ice/snow and its density between the freezing level and surface. CPR can detect the sleet without an estimation of its precipitation rate. While this does not affect the analysis of the frequency of precipitation, it does affect the intensity. As a result, our analysis of the intensity using the PC and RP products is limited to when rain is designated for the lowest layers. When the precipitation is deemed to be either mixed-phase or glaciated for the lowest layers, no precipitation rate is retrieved. Tables 2.2 and 2.3 detail the frequencies with which mixed-phase and glaciated radar columns were encountered, overall and by segments of 2.5° length (267 radar columns). Note that the 2C-SNOW-PROFILE (Mitrescu et al. 2010) dataset does provide an explicit measure of the intensity of frozen precipitation, but is not discussed here due to the very limited number of observations available.

Over Macquarie Island, mixed-phase precipitation is more frequently recorded than glaciated (Table 2.2 and 2.3). 'Glaciation segments' only occur 5.45 % of the time in winter, so including the 2C-SNOW-PROFILE would not eliminate any seasonal bias. Although more than 60 % of all individual radar columns are 'clear' in any precipitation in each season (Table 2.2), segments that contain at least one glaciation or mixed phase radar column among the 267 radar columns are more commonly observed than the 'clear' only segments, especially in winter (Table 2.3). Radar columns identified as "certain" (unattenuated near-surface

reflectivity of 0 dBZ or higher), "probable" (unattenuated near-surface reflectivity between -7.5 and 0 dBZ), and "possible" (unattenuated near-surface reflectivity < -7.5 dBZ) have been employed here (Haynes et al. 2009).

| radar columns | <i>Dec</i> | <i>Jan</i> | <i>Feb</i> | <i>Mar</i> | <i>Apr</i> | <i>Jun</i> | <i>Jul</i> | <i>Aug</i> | <i>Sep</i> | <i>Oct</i> | <i>Nov</i> |
|----------------------|------------|------------|------------|------------|------------|------------|------------|------------|------------|------------|------------|
| composition | <i>May</i> | | | | | | | | | | |
| Clear | 81.33 % | | | 69.05 % | | | 68.25 % | | | 66.62 % | |
| Warm rain | 11.53 % | | | 17.47 % | | | 11.44 % | | | 15.17 % | |
| Glaciation | 0.00 % | | | 0.11 % | | | 3.12 % | | | 1.91 % | |
| Mixed phase | 7.14 % | | | 13.37 % | | | 17.19 % | | | 16.31 % | |

Table 2.2. The frequency of the thermodynamic state of precipitation from the radar columns (including 'certain', 'probable', 'possible') of PC product over the four years 2007-2010.

| Segment composition | <i>Dec</i> | <i>Jan</i> | <i>Feb</i> | <i>Mar</i> | <i>Apr</i> | <i>May</i> | <i>Jun</i> | <i>Jul</i> | <i>Aug</i> | <i>Sep</i> | <i>Oct</i> | <i>Nov</i> |
|----------------------------|------------|------------|------------|------------|------------|------------|------------|------------|------------|------------|------------|------------|
| Clear | 27.47 % | | | 14.15 % | | | 10.00 % | | | 10.91 % | | |
| Warm rain | 32.97 % | | | 39.62 % | | | 25.45 % | | | 20.00 % | | |
| Glaciation | 0.00 % | | | 0.00 % | | | 5.45 % | | | 0.91 % | | |
| Other | 39.56 % | | | 46.23 % | | | 59.10 % | | | 68.18 % | | |

Table 2.3. The frequency of the thermodynamic state of the precipitation within a 267 radar-columns segment (2.5°). 417 segments are considered over the four years 2007-2010. "Warm rain" represents the segments consist of the pixels flagged as "warm rain" or "clear"; "glaciation" represents segments consist of the radar columns flagged as "glaciation" or "clear"; "others" includes the mixed phase and segments consist of the radar columns flagged as "warm rain" or

"glaciation".

While it is not possible to calculate the annual mean precipitation rate from CloudSat due to the mixed phase bias, it is still readily possible to record and analyze the frequency of precipitation (e.g. Ellis et al. 2009). And the precipitation rate of the warm rain is also available to analyze.

2.5. The seasonal cycle and annual trend of Macquarie Island precipitation

The historic monthly precipitation (1979-2011) at Macquarie Island is relatively flat through much of the year (~80 mm per month) with a single peak (~100 mm per month) in early autumn (March and April) (Figure 2.1). The ERA-I average monthly precipitation (1979-2011) similarly peaks in the autumn with minima in both July and December with a weak increase in between. Over this common period the average annual precipitation for the surface observations is 1023 mm per year, which is slightly greater than that from ERA-I (953 mm per year). Focusing on the early surface observations (1948-1978), the shape of the annual cycle changes little but the annual average precipitation decreases to 971 mm per year, consistent with the analysis of Adams (2009). The precipitation accumulation decreases in every month, but only the decrease for August is significant.

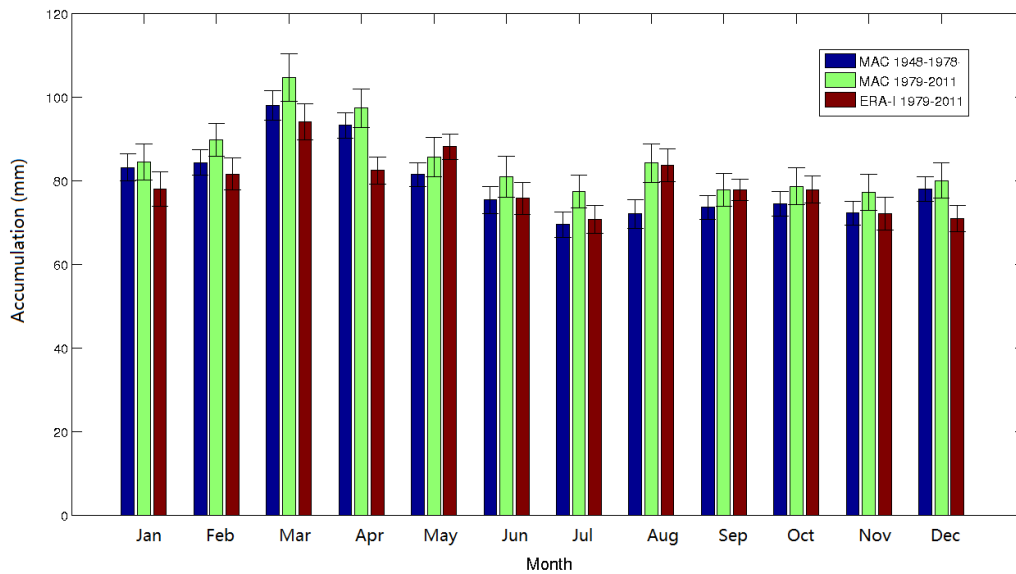


Figure 2.1. Average monthly precipitation (MAC 1948-1978, MAC 1979-2011 and ERA-I 1979-2011). Error bars show the standard errors calculated from the accumulation in each month.

2.6. The frequency and intensity of precipitation

Because the CloudSat data is available from late 2006, we have limited the analysis to the four-year period 2007-2010, in which a direct temporal comparison of the frequency of precipitation (defined in Section 2.4) can be made for the 3-h MAC observations, ERA-I and the CPR radar columns. The overall frequency of the MAC precipitation is 36.8 %. If each month is again treated as an independent sample, the 95 % confidence interval for this value is [35.1 %, 38.5 %]. The frequency of the 3-h ERA-I precipitation is 31.9 % [29.8 %, 33.9 %]. Here we have enforced a minimum threshold for ERA-I precipitation of 0.066 mm hr^{-1} to be consistent with the surface observations. The mean precipitation rate from MAC (0.32 mm hr^{-1}) is larger than that from ERA-I (0.29

mm hr⁻¹), and the monthly variability [0.31, 0.33] (mm hr⁻¹) is also underestimated by ERA-I [0.29, 0.30] (mm hr⁻¹).

The frequency for the CPR PC rain ('certain', 'probable' and 'possible' radar columns) is 30.5 % with a 95 % confidence interval as [27.1 %, 33.9 %], but reduces to 21.5 % with a 95 % confidence interval as [18.4 %, 24.6 %] if 'possible' is omitted. The mean rain rate of 'certain' radar columns only is 1.24 mm hr⁻¹ with a 95 % confidence interval as [1.19, 1.29] (mm hr⁻¹). This value is larger than the segment mean rain rate because it excludes the clear radar columns which occupy more than 60% of the columns in the rain segments. The mean rain rates of 'probable' and 'possible' radar columns are 0.28 [0.27, 0.29] and 0.13 [0.12, 0.14] (mm hr⁻¹), respectively. As the CPR RP product only employs 'certain' radar columns to avoid the drizzle that does not potentially reach the surface (Lebsock et al. 2011), its precipitation frequency is quite low at 16.3 %.

A probability density function (PDF) of the precipitation rate can be calculated for the MAC observations (3-h time intervals, 2003-2011) and the 3-h ERA-I precipitation product (Figure 4a). For the MAC observations, 'no detectable' precipitation ($0 \leq P < 0.066$ mm hr⁻¹) is encountered 63.6 % of the time, and the frequency falls off quickly as the precipitation rate increases from light (29.7 %) to moderate (7.7 %) to heavy (1.1 %) precipitation. ERA-I produces frequencies of 23.6 %, 43.8 %, 27.6 %, 4.6 % and 0.3 % for 'no precipitation', drizzle ($0 \leq P < 0.066$ mm hr⁻¹), light, moderate and heavy precipitation, respectively. The frequency of heavy precipitation from ERA-I is less than that from MAC. This implies a systematic difference between the data from a single surface station and the averaging in a model grid, because 3-h is shorter than a storm's life time.

Pfeifroth et al. (2013) compared monthly precipitation data from ERA-I with those from the rain gauges in Pacific, and found that ERA-I systematically underestimates high precipitation rates.

| Intensity (mm hr ⁻¹) | 0 | 0-0.066 | 0.066-0.5 | 0.5-1 | >1 |
|----------------------------------|------|---------|-----------|-------|-----|
| MAC (%) | 63.6 | | 29.7 | 7.7 | 1.1 |
| ERA-I (%) | 23.6 | 43.8 | 27.6 | 4.6 | 0.3 |

Table 2.4. The precipitation intensity for 3-h MAC and ERA-I from 2003 to 2011.

Given that both the PC and RP products do not produce the rain rate when mixed-phase or ice precipitation radar columns are encountered, it is not possible to directly extend the comparison to these CPR products. It is possible, however, to make such a PDF for a very limited selection of segments when neither CloudSat products reported mixed-phase or ice precipitation columns. Only 176 out of the 417 3-fold segments meet this criterion, these reduced data sets are hereafter referred to as RP1, RP3, PC1 and PC3 as both the 1-fold and 3-fold length segments are analyzed. These CloudSat PDFs may then be compared against that from the corresponding 176 3-h MAC observations (Figure 2.2). Note that such calculations introduce a strong seasonal bias as more snow/ice flags were recorded during the winter and spring seasons (Tables 2.2 and 2.3). Further note that the rain rates have been set to 0 for any "possible" radar columns for the PC1 and PC3 data sets to be consistent with the studies of Ellis et al. 2009 and Stephens et al. 2010. The MAC observations produce frequencies of 67.2 % for 'no detectable' precipitation, which is similar to 'no precipitation' ($P = 0 \text{ mm hr}^{-1}$) RP1 (66.5 %), but higher than those of RP3, PC1 and PC3.

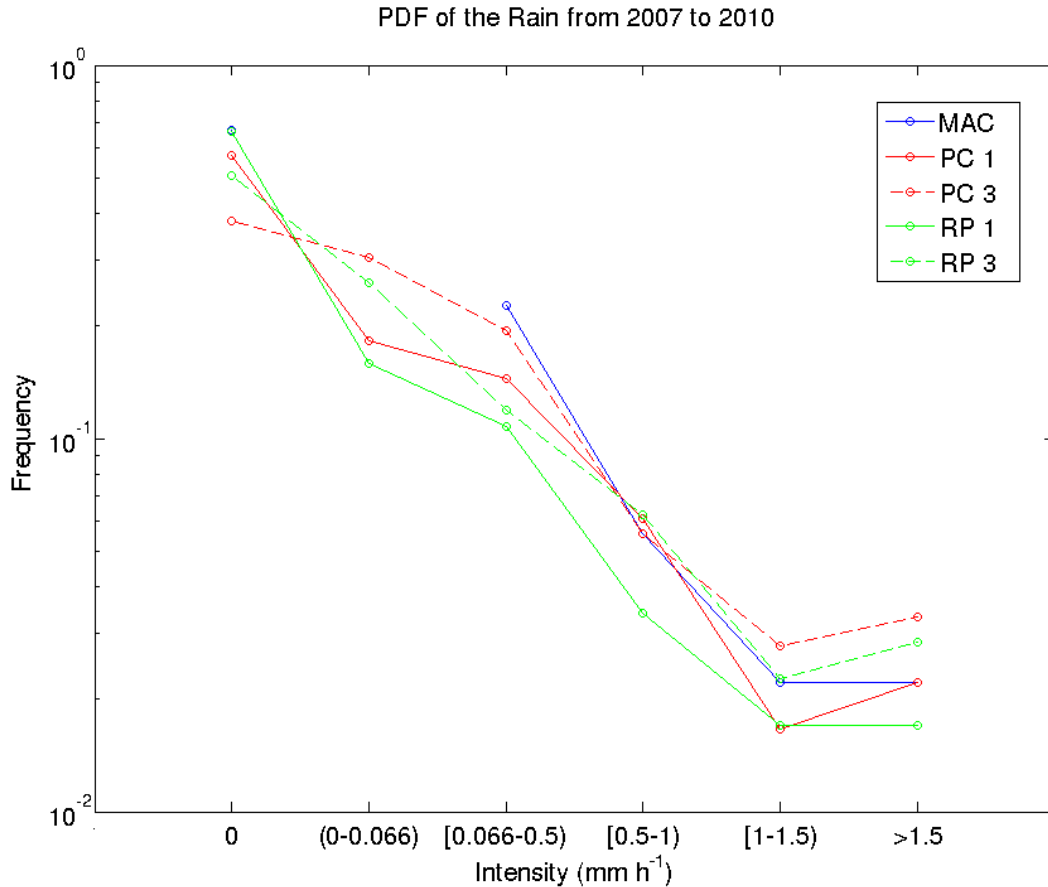


Figure 2.2. Probability density function (PDF) of warm-rain only intensity (limiting CloudSat to 176 warm rain or clear cases and the corresponding 3-h MAC cases). PC 1 and RP 1 represent 0.75° latitude segments in the CloudSat products and PC 3 and RP 3 represents 2.5° latitude segments.

The CPR RP very likely underestimates the occurrence of light precipitation (defined as $[0.066, 0.5)$ mm h^{-1}) but compares reasonably well (given the inherent space-time difficulties) for higher precipitation rates. This is perhaps not completely surprising since CPR RP derives precipitation rates only for radar columns where precipitation is "certain". The CPR PC may also be underestimating light precipitation, but any underestimate is small (compared to that of the CPR RP). Given the ambiguity of the MAC soundings at intensities

below 0.066 mm hr^{-1} , it is not worthwhile to label any one of the CloudSat products as superior to the others. Rather, the limited surface observations would generally provide some confidence to these satellite observations for this region of the SO.

The individual match-ups between MAC and the CloudSat products at a smaller time and spatial scale were further investigated using simple contingency tables at various intensity thresholds. Mean rain rates from 141 ‘rain only’ segments of only 50 km length were retrieved from the nearest 3 orbits to MAC, and were matched with the corresponding 1-h MAC observations. At this scale, both the PC (Table 2.5) and RP (Table 2.6) products show approximately 90 % of agreement (‘hits’+‘miss’) with MAC in all the comparisons using different minimum detection thresholds (0.2 mm hr^{-1} , 0.5 mm hr^{-1} and 1.0 mm hr^{-1}). MAC records slightly more precipitation events than either CloudSat product. The differences between RP and PC are significant in light precipitation, while not significant in heavy precipitation. Because the PC product includes the ‘probable’ precipitation radar columns, it includes more light precipitation and has higher frequency.

| <i>Threshold</i> | | <i>PC</i> | | <i>Threshold</i> | | <i>PC</i> | | <i>Threshold</i> | | <i>PC</i> | |
|-------------------------------|------------|------------|-----------|-------------------------------|------------|------------|-----------|-------------------------------|------------|------------|-----------|
| <i>0.2 mm hr⁻¹</i> | | <i>Yes</i> | <i>No</i> | <i>0.5 mm hr⁻¹</i> | | <i>Yes</i> | <i>No</i> | <i>1.0 mm hr⁻¹</i> | | <i>Yes</i> | <i>No</i> |
| <i>MAC</i> | <i>Yes</i> | 10.6 % | 9.9 % | <i>MAC</i> | <i>Yes</i> | 5.0 % | 4.3 % | <i>MAC</i> | <i>Yes</i> | 2.9 % | 1.4 % |
| | <i>No</i> | 2.1 % | 77.4 % | | <i>No</i> | 2.1 % | 88.6 % | | <i>No</i> | 0.7 % | 95.0 % |

Table 2.5. Contingency table showing the comparison of precipitation occurrences using the CloudSat PC product and surface observations (MAC) for the 141 clear and warm rain cases in the 50 km segments over three different thresholds: 0.2 mm hr^{-1} , 0.5 mm hr^{-1} and 1.0 mm hr^{-1} .

| <i>Threshold</i> | | <i>RP</i> | | <i>Threshold</i> | | <i>RP</i> | | <i>Threshold</i> | | <i>RP</i> | |
|-------------------------------|------------|------------|-----------|-------------------------------|------------|------------|-----------|-------------------------------|------------|------------|-----------|
| <i>0.2 mm hr⁻¹</i> | | <i>Yes</i> | <i>No</i> | <i>0.5 mm hr⁻¹</i> | | <i>Yes</i> | <i>No</i> | <i>1.0 mm hr⁻¹</i> | | <i>Yes</i> | <i>No</i> |
| <i>MAC</i> | <i>Yes</i> | 7.1 % | 13.5 % | <i>MAC</i> | <i>Yes</i> | 2.8 % | 6.4 % | <i>MAC</i> | <i>Yes</i> | 2.1 % | 2.1 % |
| | <i>No</i> | 0.7 % | 78.7 % | | <i>No</i> | 1.4 % | 89.4 % | | <i>No</i> | 0.0 % | 95.8 % |

Table 2.6. Contingency table showing the comparison of precipitation occurrences using the CloudSat RP product and surface observations (MAC) for the 141 clear and warm rain cases in the 50 km segments over three different thresholds: 0.2 mm hr⁻¹, 0.5 mm hr⁻¹ and 1.0 mm hr⁻¹.

A scatter plot (Figure 2.3) also shows these individual match-ups between MAC and CloudSat. Again, the RP product missed more light precipitation recorded by MAC [0.2, 0.8) mm hr⁻¹ than the PC product. Paired t-tests including 141 pairs of rain rates in PC and MAC find that the difference is not significant at the 95 % confidence level, but the difference between RP and MAC is significant.

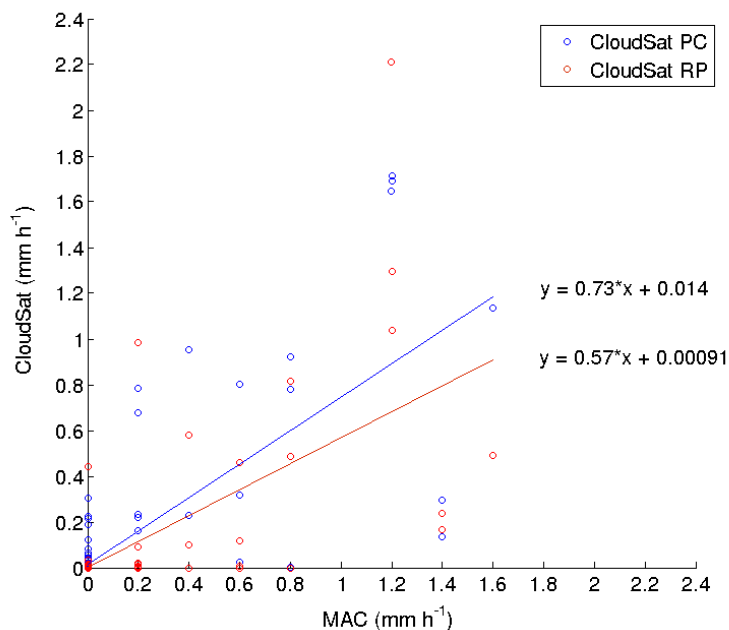


Figure 2.3. Scatter plot of rain rates from MAC and two CloudSat products (PC

and RP) in 50 km segments from 141 clear and rain cases. Two lines are the linear fits of rain rates from MAC and the two CloudSat products.

2.7. Wind roses, precipitation roses and Ekman spirals

Using the 900 hPa winds and surface precipitation from 2003 to 2011, a precipitation rose (Figure 2.5) reveals that the vast majority of the surface precipitation (MAC) occurs at relatively weak precipitation rates. Not surprisingly, precipitation arrives predominantly from the west. At this coarse 6-h time scale, light precipitation is present 43.8 % of the time, moderate precipitation is present 5.8 % of the time, and heavy precipitation is present 0.7 % of the time. No precipitation was recorded for the remaining 49.7 % of the 6-h time blocks. To first order this is comparable to the statistics from ERA-I, which has precipitation present at 48.1 %, 4.3 % and 0.2 % for light, moderate and heavy precipitation, respectively. ERA-I also produces a large amount (35.4 %) of drizzle ($0 < P < 0.033 \text{ mm hr}^{-1}$), which is too weak to be recorded by MAC. The wind roses plotted from MAC records shift evidently from the results of ERA-I, at 1000 hPa and 975 hPa level. Ekman spiral and orographic effects may account for this surface wind shift.

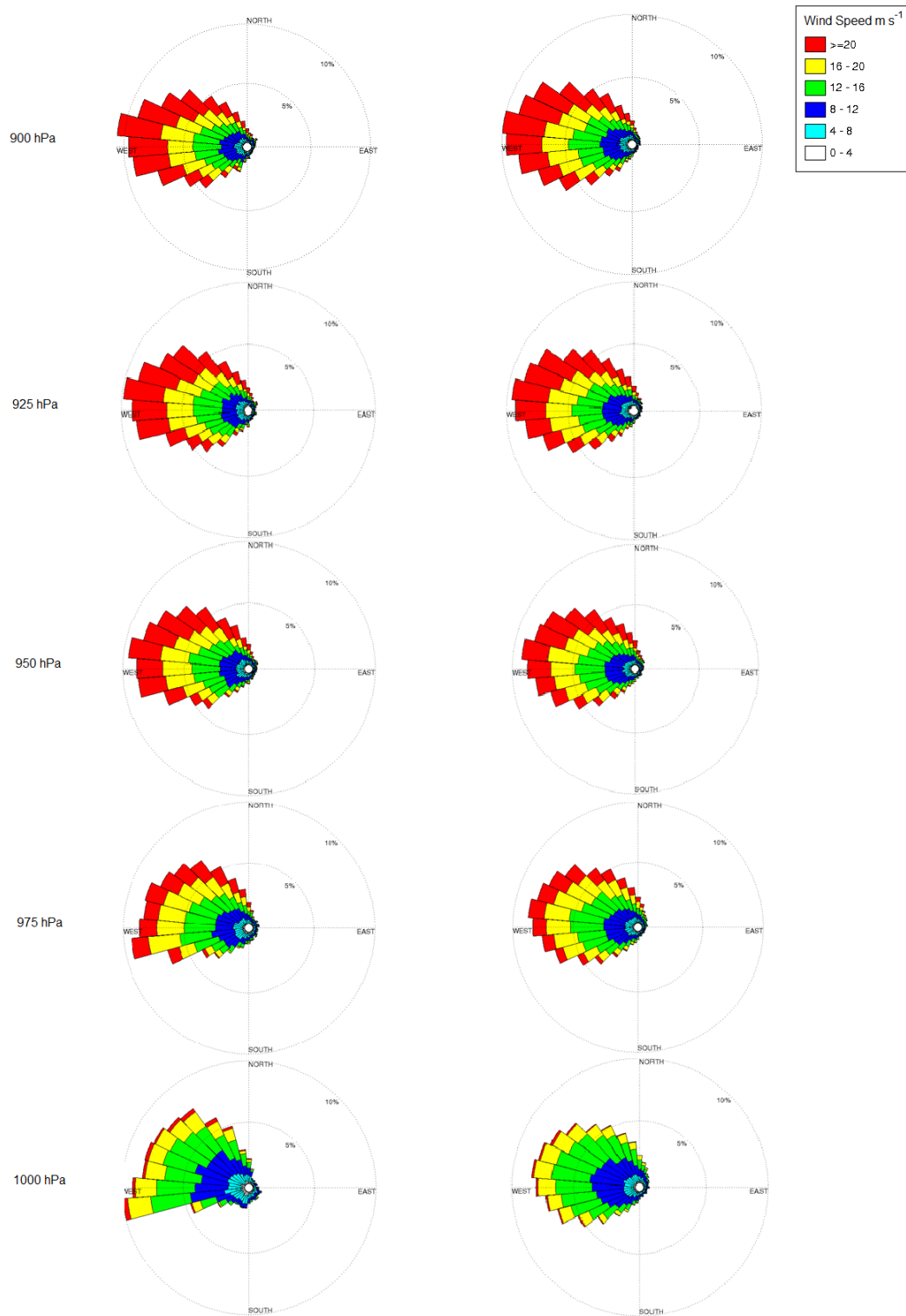


Figure 2.4. Wind roses and precipitation roses over Macquarie Island. (a) Wind roses from sounding (left) and ERA-I data (right), on different pressure levels from 900 hPa to 1000hPa, from 2003 to 2011.

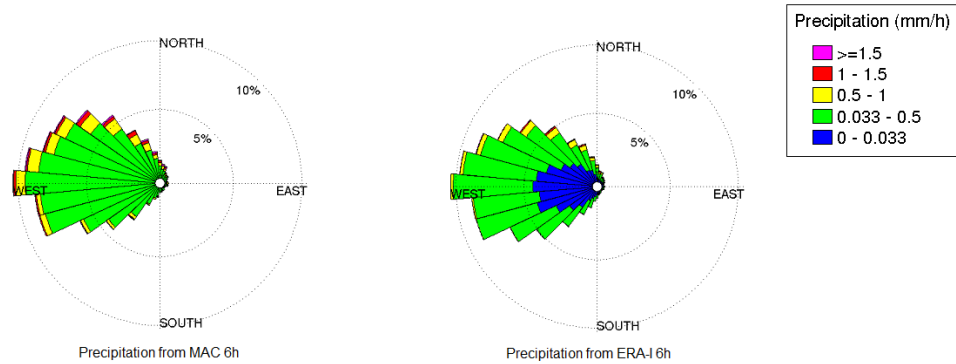


Figure 2.5. Precipitation roses from MAC (left) and ERA-I records (right) with wind on 900hPa from ERA-I, from 2003 to 2011.

Hande et al. (2012b) examined the thermodynamic structure of the Macquarie Island soundings from 1995-2011 and found Ekman spirals in 61% of the cases with northerly winds, and only 31% for the southerlies. They hypothesized that this difference is caused by the northerlies near the surface advecting warm air over the cold water and resulting in mostly stable boundary layers. However, our results suggest that the orographic effects should also be taken into account for the blocking of the southerly wind component. Figure 2.6 shows the orographic effects on the surface wind direction. The wind direction from the MAC records is compared with ERA-I in which the orographic effects of Macquarie Island are absent because of the coarse model resolution. If we ignore absolute differences between ERA-I and MAC of less than 10° , we see that a clockwise rotation prevails over an anticlockwise rotation. The main obstacles are to the southwest and northeast of the station. The clockwise rotation is relatively homogeneous on the open water between the west and north, which might result from the Ekman spirals; while the magnitude of turning at the 270° is remarkable, which represents the air turning around the 300 m ridge immediately to the southwest

of the station, where the terrain effect amplifies the Ekman turning. To the other side of the ridge, the wind from the south turns anticlockwise, which offsets the Ekman spiral.

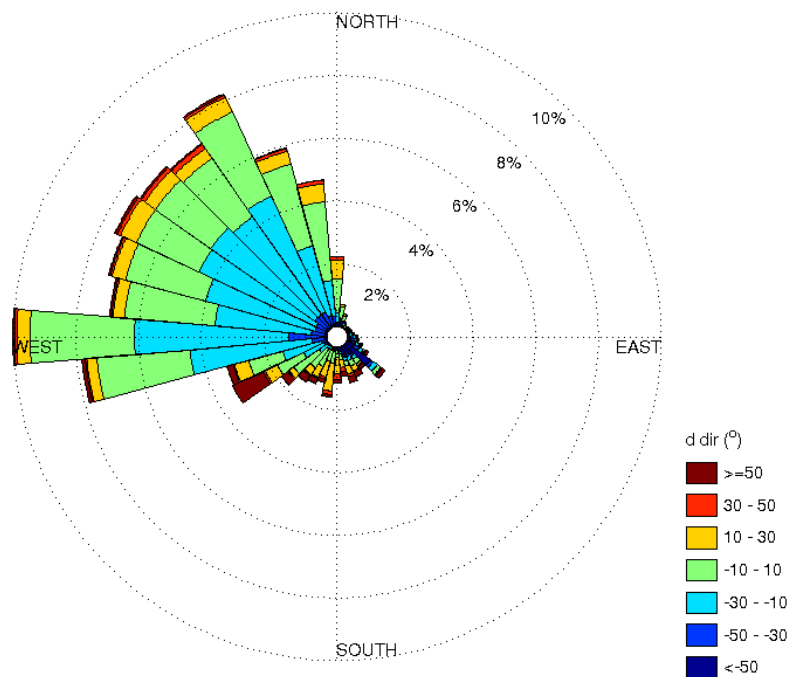


Figure 2.6. The wind rose at 10 m for 2003-2011. The wind rose represents the occurrence of the wind direction from the MAC records; the colours represent the ERA-I differences from the MAC record. Each bin is 10° .

2.8. Summary

The several decades of meteorological observations from Macquarie Island (54.50°S 158.94°E) are a valuable tool in the effort to understand the energy and water budgets over the SO. These precipitation records, have been analyzed to improve understanding of the physical nature of the local precipitation, and then compared to the precipitation products of CloudSat (PC and RP) and ERA-I,

although the different temporal and spatial geometry of these products hinders a robust comparison.

The annual cycle of the long-term precipitation records (1979-2011) displays a peak in March, but is relatively flat for the rest of the year. ERA-I also records a peak in March, but shows much greater variability throughout the year. Annually averaged from 1979 to 2011, ERA-I underestimates the precipitation as observed at Macquarie Island by approximately 6.8 %.

From 2003 to 2011, the frequency of the 3-h MAC precipitation is 36.4 %. The frequency decreases with an increase of the precipitation intensity, from 29.7 % for the light precipitation, to 1.1 % for the heavy precipitation. The overall frequency of the ERA-I precipitation is only slightly lower (32.7 %) than MAC in these 9 years. The light precipitation in ERA-I (27.6 %) is also comparable with MAC, but ERA-I produces less heavy precipitation (0.3 %) and a considerable amount (43.9 %) of drizzle. This drizzle is below the detectable threshold of MAC.

From 2007 to 2010, The CloudSat PC and RP products were limited to segments that only included 'warm' rain (i.e. mixed-phase and glaciated precipitation were omitted). This filtering led to a seasonal bias in the results and a relatively small pool of 176 segments for the analysis. Following Stephens et al. (2010), segments were considered at 1-fold ($\sim 0.75^\circ$) and 3-fold ($\sim 2.5^\circ$) the length of the ERA-I grid resolution. These CPR products overestimated the frequency of 'no precipitation' ($P = 0 \text{ mm hr}^{-1}$) and drizzle compared to MAC (Figure 2.2), especially at the shorter segment length. The frequencies of light precipitation were correspondingly underestimated, particularly for the RP product. Paired t-

tests including 176 pairs of rain rates in CloudSat products (PC and RP) and MAC find that only the 3-fold PC statistics to be significantly different than that of MAC at the 95 % confidence level.

At higher temporal (1-h) and spatial ($\sim 0.5^\circ$) resolution, individual match-ups between MAC and CloudSat products show approximately 90 % of agreement in event detections ('hits'+ 'miss'). The PC product shows marginally greater skill for light precipitation than the RP product primarily because it has a higher frequency as the algorithm includes 'probable' precipitation radar columns, whereas the RP product only includes 'certain'.

Ekman spirals are common in the PBL over Macquarie Island. If the air mass has a southerly or southwesterly origin, the island can change the surface airflow and force it to turn clockwise west of the island and anti-clockwise south of the island. In the former case, the terrain effect amplifies the Ekman turning, while in the latter case the Ekman spiral and terrain effect offset each other.

3. Precipitation and fronts

The cold front is a zone where cold, dry stable air replaces warm, moist, conditionally unstable subtropical air; the warm front is the leading edge of advancing warm, moist, subtropical air replaces the retreating cold air (Ahrens 2007). Cold fronts typically move faster and are more steeply sloped than warm fronts. Adams (2009) partially attributed the increasing trend in rainfall over Macquarie Island to an increase in cyclonic activity. As the synoptic meteorology over the SO is dominated by the circumpolar storm track, it is of interest to identify how much precipitation occurs due to frontal activity and how much is not immediately associated with fronts. The analysis of Catto et al. (2012) finds that fronts contribute to up to 90% of the heavy precipitation events on the storm tracks over the SO. In the study by Catto et al. (2012), fronts were identified by the method of Berry et al. (2011) on the ERA-I reanalysis. In this chapter, we employ the MAC surface observations to explore this work. The analysis of Catto et al. (2012) is limited by notable inconsistency in identifying fronts with respect to the various algorithms. Relatively weak fronts cannot be adequately represented in the reanalysis products. An example of a heavy precipitation event associated with a weak front is explored in the following first case study. Even more, heavy precipitation events cannot be associated with either fronts or cyclonic lows, which is shown in the second case study. Much of this research has also been published in Wang et al. (2015).

3.1. Identification of fronts and lows

There are a variety of means of identifying fronts and mid-latitude cyclones, each

with its own strengths and weaknesses; we consider four such methods. Historically, the ABoM produces synoptic weather charts every 12 hours including major cyclones and associated cold fronts over the SO, which are primarily based on coarse global numerical weather prediction (NWP) output and satellite observations (hereafter referred to as the ABoM method). Such forecasts commonly capture only prominent synoptic scale events, with a potential of missing smaller transient mesoscale events.

Berry et al. (2011; hereafter referred to as the BRJ method) produced a climatology of fronts from the global reanalysis product ERA-40. Fronts were defined by the gradient in the horizontal wet bulb potential temperature at 850 hPa. This method identifies cold, warm and quasi-stationary fronts, with the overall peak frequency in fronts found along the storm tracks over the SO and North Pacific and North Atlantic.

Adams (2009) used the local surface pressure (p) measurements to identify when low-pressure systems were passing over Macquarie Island (hereafter referred to as the ASP method). Specifically, a positive second derivative of pressure with respect to time (d^2p/dt^2) was used to identify times when the pressure was concave upwards. No distinction was made between warm, cold and stationary fronts, and low-pressure systems. When a preselected threshold of the surface pressure was passed (e.g. $d^2p/dt^2 > 0.2 \text{ hPa h}^{-2}$), a 'cyclonic activity event' was defined. The number of events identified by the ASP definition was found to increase from roughly 10 per month in 1970 to 15 per month in 2008 (Adams 2009).

We have modified the ASP method to identify the fronts by further incorporating the surface observations of wind direction and temperature in 3-h time series ($d^2p/dt^2 > 0.1 \text{ hPa h}^{-2}$, $dT/dt < -0.2 \text{ }^\circ\text{C hr}^{-1}$, and $d\text{dir}/dt < -5 \text{ }^\circ\text{hr}^{-1}$; hereafter referred to as the MSP method.) These thresholds are deduced from two training periods during the winter of 2002 and summer of 2003. The changes of pressure, wind direction and temperature in 3-h time series during the frontal passage time (from ABoM) have been recorded and their maxima have been used as the identification thresholds.

For the cyclonic lows, the decrease of surface pressure has been used to identify the cyclones passing directly overhead ($dp/dt < -8 \text{ hPa hr}^{-1}$). This is also deduced from the winter of 2002 and summer of 2003, when cyclonic lows were recorded by ABoM and the surface pressure observations.

Given the coarse temporal resolution in the production of the daily Mean Sea Level Pressure (MSLP) charts, it is not practical to make such a calculation using the ABoM definition of fronts. They are, however, included in the initial discussion to better appreciate the occurrence of fronts over Macquarie Island.

These various definitions of fronts and cyclonic activity commonly identify the same strong events, but are not always consistent during other periods as illustrated by a two-month sample (Jul and Aug 2002) (Figure 3.1a). During these two months, ABoM identified 26 fronts, which is relatively consistent in number with BRJ (24 fronts), though not necessarily the same front or with the same timing. Both of these methods rely on an analysis or reanalysis product. ASP (30 fronts) and MSP (29 fronts) show few differences here, as they both primarily

use time series of the surface pressure (Table 3.1). The corresponding surface observations (pressure, wind direction, temperature and precipitation) highlight the variability of the meteorology along the storm track (Figure 3.1c).

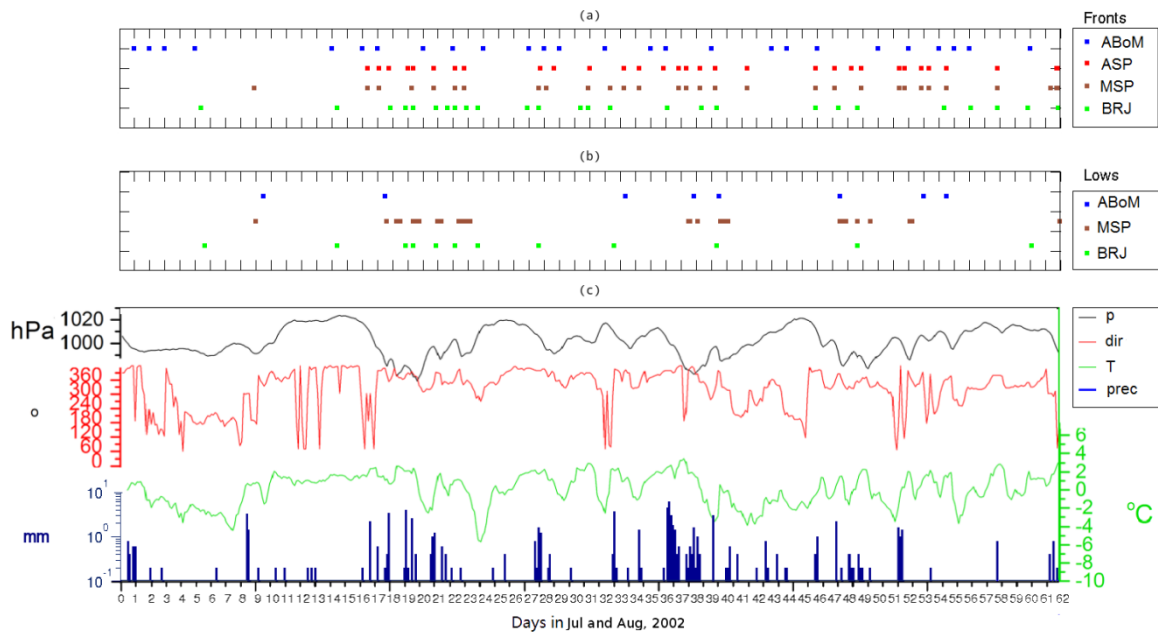


Figure 3.1. 2-month time series (July-August, 2002) of the identified (a) fronts and (b) lows using different definitions (ABoM, ASP, MSP, BRJ), with (c) the corresponding time series of surface precipitation and thermodynamic variables (p, dir and T).

| | | MSP | |
|-----|---|-----|-----|
| | | Y | N |
| ASP | Y | 26 | 4 |
| | N | 3 | 211 |

Table 3.1. Counting table for MSP and ASP frontal identifying algorithm in July and August, 2002. The temporal resolution for each counting is 3 hours.

3.2. Statistics of frontal and non-frontal precipitation

For all of these methods, MAC observations of precipitation recorded in the six hours before or after a front are regarded as being associated with that front (or cyclonic low). Also, even though the CPR product is able to distinguish between frontal and non-frontal rainfall, this distinction is not employed due to the limitations of the precipitation rate and the limited sample size.

Employing the MAC observations alone, the fraction of the precipitation associated with 'cyclonic activity' (which includes fronts and cyclonic lows) can be calculated using either the ASP or MSP definitions (Figure 3.2). The ASP definition finds that roughly half of the light precipitation events occur during periods of 'cyclonic activity' and increases steadily to over 80 % for heavy precipitation events. The MSP definition finds considerably less precipitation to be associated with frontal passages at all intensities. Surprisingly, the amount of precipitation events associated with cyclones – as opposed to fronts – remains relatively steady even as the intensity of the precipitation is increased.

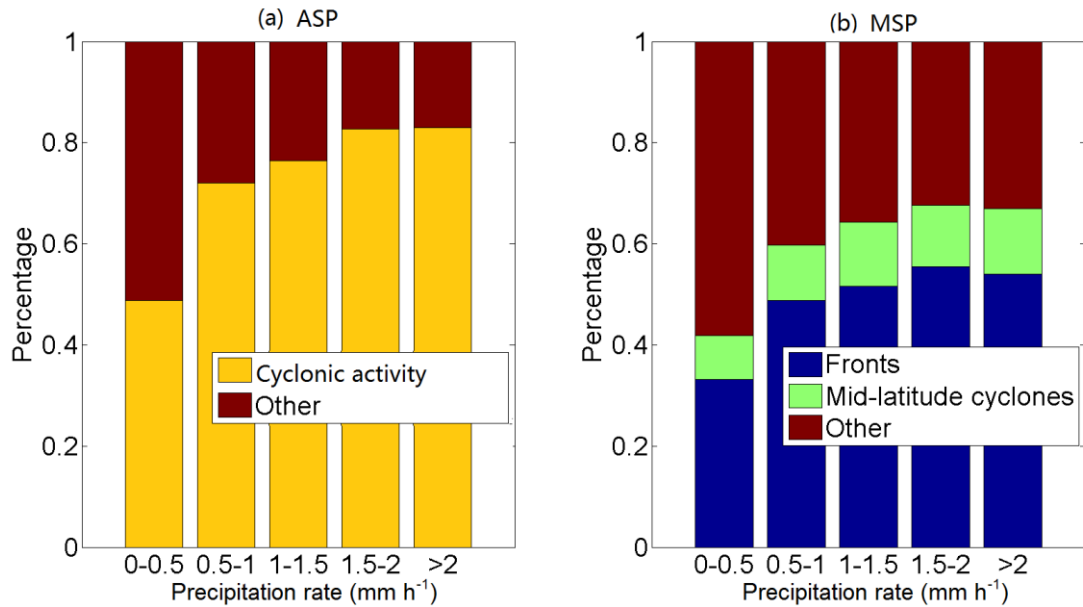


Figure 3.2. Rainfall decomposition into different intensities with (a) ASP definitions (identifying fronts with a threshold of the second derivative of surface pressure) and (b) MSP definitions (identifying fronts with a threshold of the second derivative of surface pressure and the first derivative of wind direction and temperature) using precipitation data from MAC from 2003 to 2011.

The impact of the time window (a time interval around the frontal passage time) on the percentage of the frontal precipitation is shown in Figure 3.3. ASP identifies more frontal precipitation than MSP at the same window time. Both of their slopes decrease with the window time, which implies that there is more precipitation near the defined frontal time. These two lines become roughly linear when window time is larger than 12 hours, which implies that the effect of the local front is no longer evident and only the duration of the window defines the amount of precipitation. Naud et al. (2012) found precipitation associated with the Southern Hemisphere extra-tropical cyclones tends to fall within a 10

degree range across the front. If this distance is divided by the mean wind speed of 16 ms^{-1} on 900 hPa, the time is also approximately 12 hours. Catto et al. (2012) employed GPCP daily precipitation dataset (Huffman et al. 1997) with BRJ frontal identifying method in $2.5^\circ \times 2.5^\circ$ grid, and found that 68% of the in mid-latitude precipitation comes with fronts and this value increases to 90% in the major oceanic storm tracks. Macquarie Island is located in the region, where the proportion of precipitation associated with fronts ranges from 80% to 90%. Although we used different precipitation dataset (MAC) and frontal identifying method (ASP and MSP) in Figure 3.3, this proportion also ranges from 80% to 90% with a window time of 24 hours, which is consist with that in Catto et al. (2012).

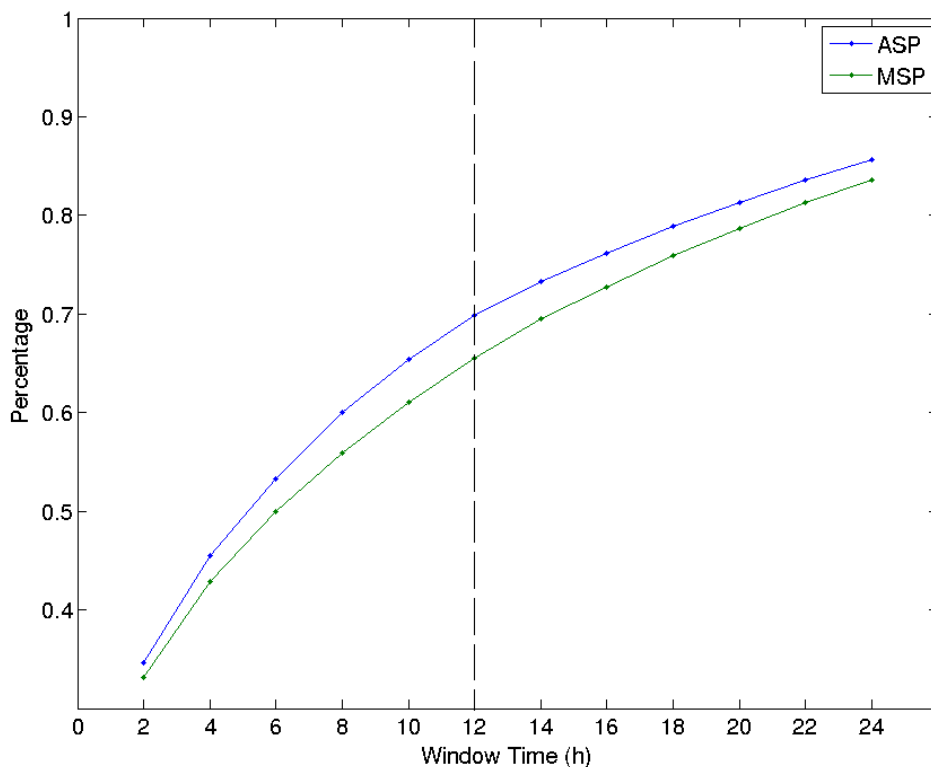


Figure 3.3. The percentage of the precipitation in the frontal window time using ASP and MSP method.

The BRJ classification may be used with any reanalysis product; in this work we use the ERA-I reanalysis to be consistent with the comparison between ERA-I and MAC in Chapter 2. Any surface precipitation record can be decomposed according to this classification. In Figure 3.4 the precipitation decomposition is constructed for the precipitation from ERA-I and MAC. The precipitation in a 6-hour time range from a cold, warm or stationary front has been regarded associated with a front. These decompositions are consistent with ASP and MSP decompositions. At weak precipitation rates, the ‘other’ class is dominant. As the precipitation rate increases, the precipitation event is more likely to be associated with a cold front. This relationship between intensity of the precipitation rate and the occurrence of a frontal event is stronger when the ERA-I precipitation is used.

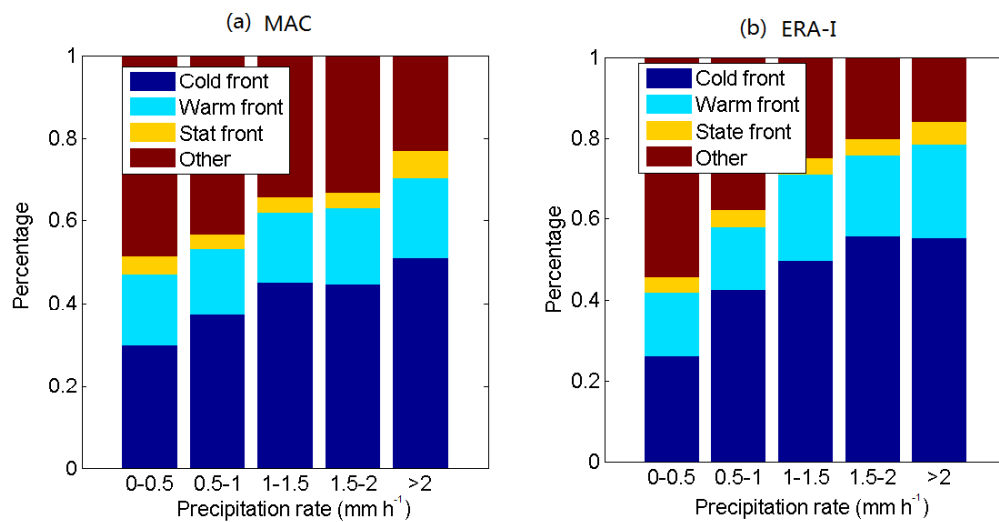


Figure 3.4. The percentage of the precipitation associated with cold, warm and stationary fronts, and others in different intensities with the BRJ definition using precipitation data from (a) MAC and (b) ERA-I from 2003 to 2011.

3.3. Selection of case studies

Figure 3.1 highlighted that there is notable inconsistency in identifying fronts with respect to the various algorithms. An example of warm front is explored in the following first case study. Figure 3.4 suggests that roughly 20 % of the extremely heavy precipitation ($P > 2 \text{ mm hr}^{-1}$) is not associated with a front or cyclonic activity. A second case study is presented for such an 'other' class event. The two case studies enable an effort to tie together the various precipitation products at Macquarie Island (MAC, ERA-I, RP and PC) with the meteorology of the SO.

3.3.1. A case study of strong precipitation with a warm front

An eastward moving low-pressure system on 16 March 2008 is examined as an example in this section. The MSLP analysis at 00 UTC (Figure 3.5) displays a weak shortwave trough to the west of the island, which was actually not classified as 'cyclonic activity' or a front by any of the algorithms (ASP, MSP, BRJ or ABoM). The changes in wind direction and temperature are witnessed at about 00 UTC. Although there is a pressure change, it does not pass the ASP second derivative threshold. A strong high-pressure system is located over the Tasman with a ridge extending to the south across much of the SO and over Macquarie Island. The 700 hPa analysis (not shown) also indicates that Macquarie Island is located behind the upper-level ridge. The MODIS image of cloud-top temperature at ~03:50 UTC reveals a thick cold (230 K) cloud band approaching Macquarie Island from the west. Macquarie Island is underneath the front edge of the cloud band. The sounding at 23 UTC 15 March exhibits a

shallow unstable layer below 870 hPa, and an increase of moisture in the mid-troposphere. The winds swing from northwesterly below 900 hPa to westerly and southwesterly aloft.

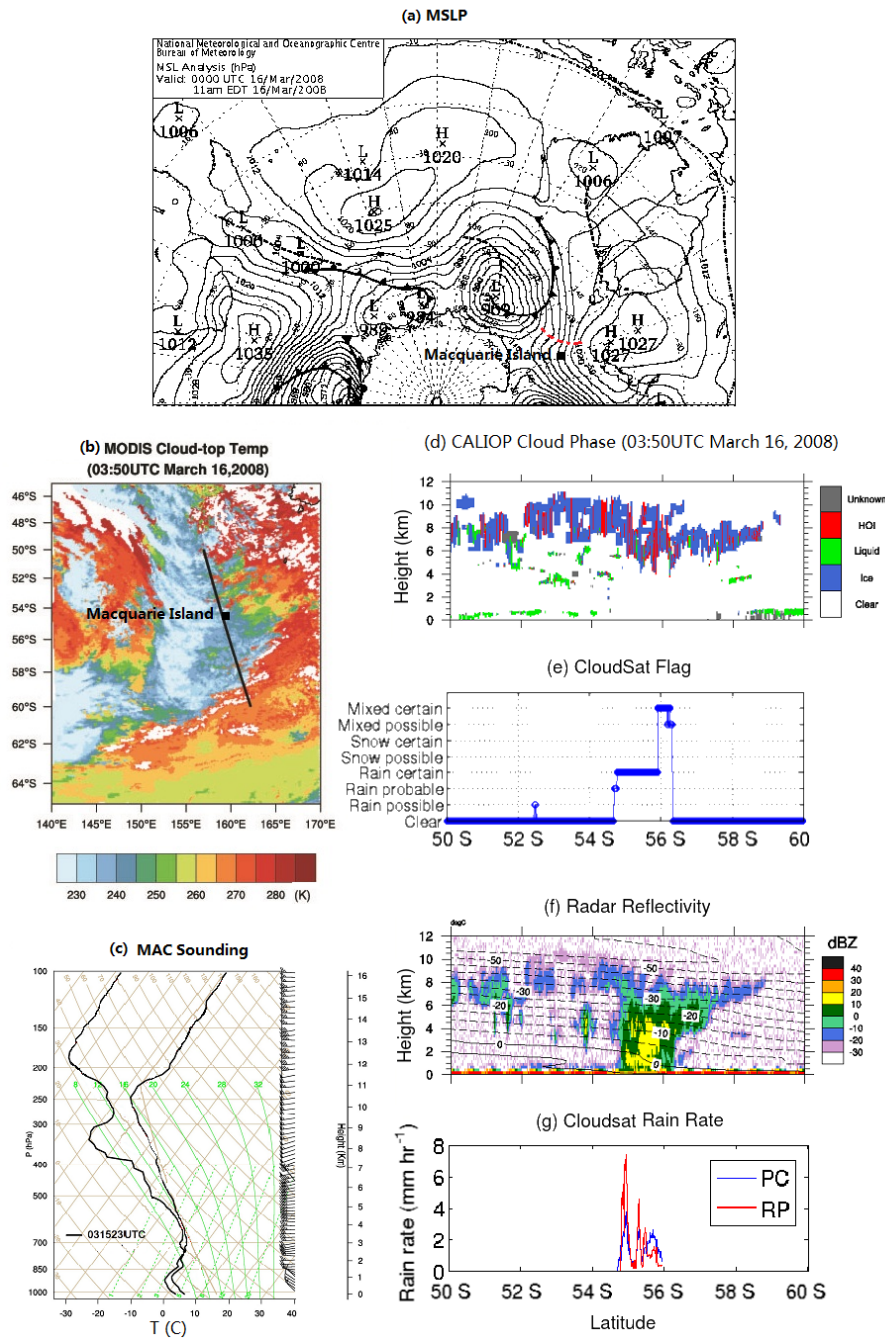


Figure 3.5. The first case study over Macquarie Island on 16 March, 2008 with (a) Mean Sea Level Pressure from ABoM (The dash line shows the location of the trough), (b) MODIS cloud-top temperature, (c) Macquarie Island Soundings, (d) CALIOP Categorization (HOI: horizontally oriented ice), (e) Precipitation Flags from CloudSat PC, (f) CPR Reflectivity, and (g) Rain Rates from CloudSat PC and RP.

An A-Train segment passes through the leading edge of the thick cloud band (Figure 3.5). The Cloud-Aerosol Lidar with Orthogonal Polarization (CALIOP) cloud thermodynamic phase (Hu et al. 2009) and the CPR radar reflectivity depict a thick, high-altitude anvil across most of the segment, with radar reflectivity higher than -10 dBz between 55 and 56 °S, which demonstrates a convection. The lidar signal is likely to be fully attenuated in this region. The CALIOP cloud phase suggests that much of the evident cloud top at ~4 km altitude is composed of liquid water. Boundary layer clouds at altitudes below 1 km are observed to both the north and south of the convective region. The radar reflectivity above an altitude of 8 km is relatively weak ($Z_e < -10$ dBz). The radar is unable to pick up the low-altitude boundary layer clouds due to their proximity to the surface and the resulting surface clutter (Marchand et al. 2009). The ECMWF temperature analysis is overlaid on Figure 3.5f. The freezing level falls from around 3 km at 50 °S to below 500 m at 60 °S with the steepest drop occurring through the heavy convection. The low-elevation clouds to the south of this point are, composed of supercooled liquid water, according to the CALIOP cloud phase.

Looking over the entire segment, both the CPR precipitation product (PC and RP) shows a relatively modest precipitation event limited to the convective region. Note that no precipitation is recorded south of 56 °S, where the boundary layer temperature has dropped to below 0 °C. Both the CPR precipitation product records precipitation along this segment but has designated this precipitation as 'mixed phase'.

The 6-h average MAC rain rate is 0.57 mm hr⁻¹. Over the last three hours the

average rain rate is 0.73 mm hr^{-1} . The CPR precipitation products (taken at 3:53 UTC) record a moderate event (0.66 mm hr^{-1} from PC and 0.82 mm hr^{-1} from RP) in a 2.5° segment of the granule. The corresponding ERA-I record is 0.46 mm hr^{-1} . At this point in time, none of the methods used in this study identifies a frontal passage or cyclonic activity, highlighting the difficulty in defining such events and the speed at which they can develop over the SO.

3.3.2 A case study of strong precipitation with an anti-cyclone

The second case study examined (01 November 2010) appears to be an exception to the conventional view of heavy precipitation being tied to fronts in the mid-latitudes, for this event is not associated with a front. The average CPR PC rain rate at $\sim 03:50$ UTC is 2.06 mm hr^{-1} , which is actually the greatest rainfall rate recorded for 52 segments that pass closest to Macquarie Island from 2007 to 2010. The MSLP at 00 UTC (Figure 3.6) indicates that Macquarie Island is located at the outskirts of a strong anti-cyclone centered near the southern edge of New Zealand. The high-pressure system is accompanied by an elongated trough up through the Tasman to the northwest, an approaching front to the far west, and a frontal passage to the far south. This synoptic pattern creates a sharp pressure gradient across Macquarie Island, constricting the flows to form a tropospheric “jet” from the north to Macquarie Island, which is shown by the wind vectors in Figure 3.6c. Different from the first case, the east-located high enables the transport of moisture and heat from the warmer water, facilitating a rapid saturation of the fast moving, cooling air. The routine sounding at 23 UTC 23 October (Figure 3.6 c) shows a deep, moistened atmosphere with the air mass below 700 hPa being completely saturated. The strong, constant northwesterly

wind throughout the troposphere suggests the joint influence of the extending upper-level trough and the high.

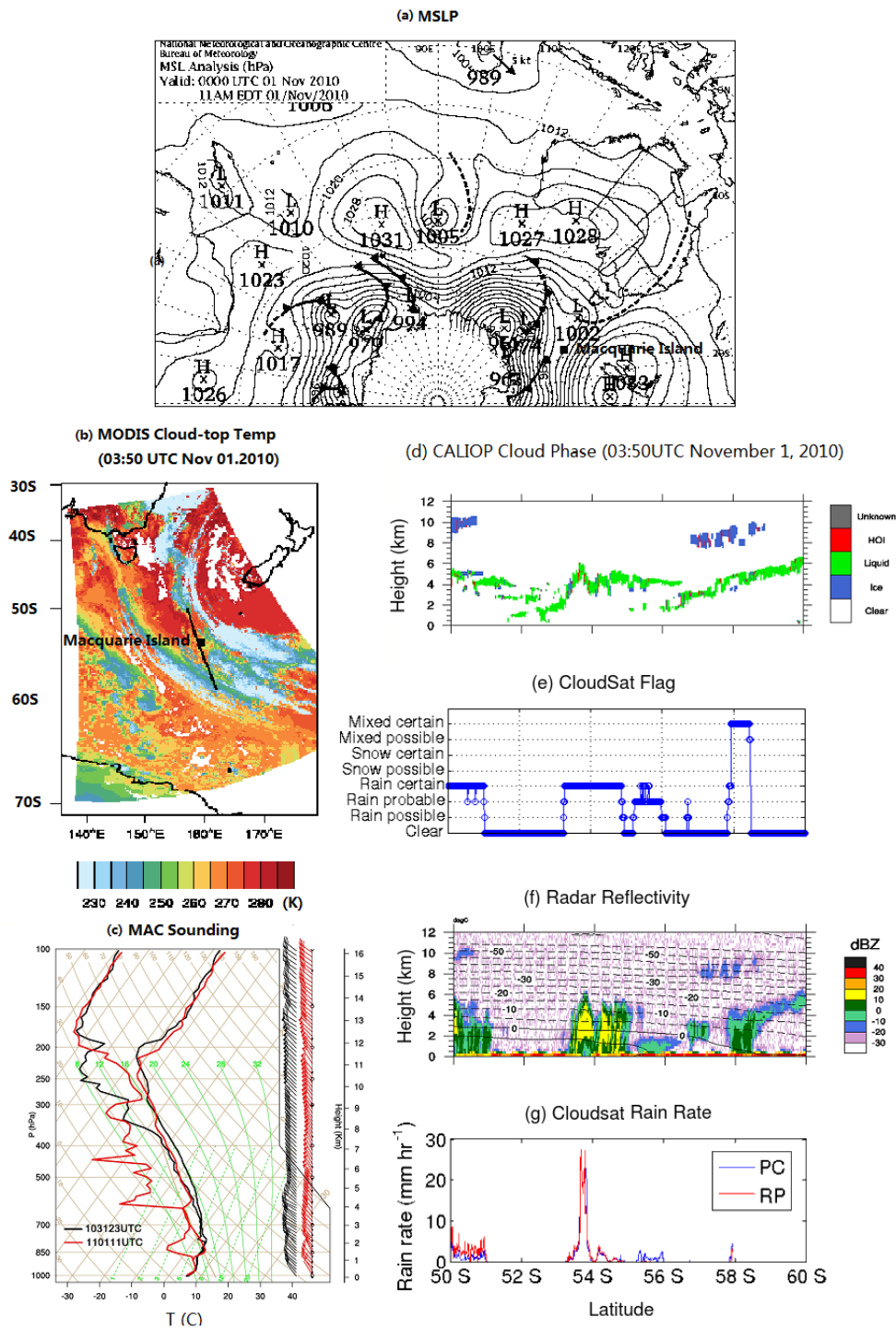


Figure 3.6. The second case study over Macquarie Island on 01 November, 2010 with (a) Mean Sea Level Pressure, (b) MODIS cloud-top temperature, (c) Macquarie Island Soundings, (d) CALIOP Categorization (HOI: horizontally oriented ice), (e) Precipitation Flags from CloudSat PC, (f) CPR Reflectivity, and (g) Rate Rates from CloudSat PC and RP.

The MODIS image of cloud-top temperature at ~03:50 UTC is consistent with the synoptic analysis (Figure 3.6b), suggesting that an anti-cyclonic flow is dominant at this time. The MODIS cloud-top temperature shows streaks of cold cloud tops ($-40\text{ }^{\circ}\text{C}$) within this field. CALIOP, on the other hand, portrays a field of mid-altitude clouds composed of SLW. There are patches of high-altitude cirrus near $50\text{ }^{\circ}\text{S}$ and $58\text{ }^{\circ}\text{S}$, but none near Macquarie Island. The CloudSat radar portrays active convection to a height of $\sim 5\text{ km}$ at this time near $54\text{ }^{\circ}\text{S}$. Convection near $50\text{ }^{\circ}\text{S}$ and $58\text{ }^{\circ}\text{S}$ is evident, too. It is interesting that CloudSat misses much of the cloud near $52\text{ }^{\circ}\text{S}$ that is captured by CALIOP. This is consistent with clouds composed of small droplets that are insufficiently reflective for the radar to detect.

The hourly precipitation rate observed at MAC (Table 3.2) averages to 1.4 mm hr^{-1} over the 3-h period (02:00-04:00 UTC), or 0.6 mm hr^{-1} if only the last three hours (03:00-05:00 UTC) are used. The CloudSat rain rate for the segment is 2.06 mm hr^{-1} from PC and 2.37 mm hr^{-1} from RP, even though the actual rain rate is probably higher because some of the columns reach the maximum retrievable rain rate or the CPR (Haynes et al. 2008). The rain rate from PC is weaker than that from RP at the peak near $54\text{ }^{\circ}\text{S}$, and PC records 'probable' rain on $56\text{ }^{\circ}\text{S}$, but that is rejected by CloudSat RP.

| Date | Time (UTC) | Precipitation Rate (mm h ⁻¹) |
|------------|------------|--|
| 2010.11.01 | 0:00 | 3.4 |
| | 1:00 | 1.4 |
| | 2:00 | 2.6 |
| | 3:00 | 0.8 |
| | 4:00 | 0.8 |
| | 5:00 | 0.2 |

Table 3.2. Hourly precipitation records from Macquarie Island for 2010 case study.

South of 58 °S, the boundary layer temperature has decreased to below freezing, which means that neither the PC nor RP rain rates are available. Near Macquarie Island, however, intense rainfall is evident. The corresponding 3-h ERA-I record (at 06:00 UTC) is 0.53 mm hr⁻¹, which is a large value for the ERA-I records over the SO (as shown in Table 2.4). Given the uniqueness of the meteorology of this event, it is not surprising that a front (or cyclonic low) was not diagnosed from any of the various methods. It would be interesting to further explore the potential for such an event to be linked to the moisture transportation as an Antarctic ‘atmospheric river’ (e.g. Tsukernik and Lynch 2013).

3.4 Summary

Fronts or cyclonic activity are associated with light precipitation roughly half of the time and increased to roughly 80 % of the time for heavy precipitation. It was further noted that the definition of fronts was commonly inconsistent over the SO, especially for weaker events. Also a non-trivial fraction (~20 %) of the heavy

precipitation is not closely associated with frontal systems.

Two cases studies have been examined to tie together the synoptic meteorology and the various precipitation observations, which highlight the difficulties in ground-validation of the satellite observations due to mismatches in sensitivity and sampling between remote and in-situ measurements and the necessity of a rigorous evaluation. The various precipitation products (MAC, PC, RP and ERA-I) consistently record heavy precipitation for both cases, even though neither event was classified as being associated with a frontal passage or a cyclonic low.

4. Orographic effects of Macquarie Island

It is well appreciated that winds, cloud cover and precipitation can readily be affected by any significant orography. Over the SO boundary layer, with the strong winds and high relative humidity, even modest orography has the potential to create local perturbations to the clouds, precipitation and thermodynamics. For example, the airborne observation in the Deep Propagating Gravity Wave Experiment (DEEPWAVE; Fritts et al. 2015) found strong high-altitude gravity waves over the SO even when orographic forcing was weak. In this chapter we examine the nature of the orographic forcing arising from Macquarie Island. Our primary focus is on the surface precipitation records at the station, although our analysis is expanded to the meteorology near the island. We employ high-resolution numerical simulations (with and without terrain) to isolate the effect of the orography on the dynamics and local meteorology.

4.1 Orographic forcing on precipitation

The influence of orography on precipitation, in particular, has long been recognized. For example, Browning et al. (1974) studied orographic effects on precipitation during the passage of cold fronts over West Britain. Smith (1979) showed that the orographic effect on precipitation over small hills is different from that over mountains, where the rainfall maxima is near the hilltop instead of the upslope region. Johansson and Chen (2003) analyzed 15 years of precipitation records from 370 stations in Sweden and found that precipitation increased with wind speed on the upwind side and there was less variation in precipitation on the leeward side, where wind speed did not strongly affect the

amount of precipitation. Houze (2012) detailed twelve different mechanisms that can influence orographic precipitation including upslope enhancement, blocking effects of the terrain and the “seeder-feeder” mechanism.

The Froude number (Fr) or its inverse, a non-dimensional mountain height (Smith 1989), has been used as a key parameter for defining whether an airflow passes over or around a mountain/obstacle. When $Fr > 1$, the current is forced over the mountain, as a result, gravity waves and lee waves are common. When the $Fr < 1$, the magnitude of any gravity wave is drastically reduced and the flow is primarily disturbed horizontally rather than vertically. Smolarkiewicz et al. (1988) used the 3-D Froude number for isolated three-dimensional mountains on the island of Hawaii. More details about Froude number used in this study are in Chapter 5. Besides the Froude number, Watson and Lane (2012) used a series of idealized, high-resolution simulations to show that precipitation is also sensitive to the shape of the mountain.

Numerical simulations have been widely used to study the orographic effects on flow dynamics and precipitation. The resolution of numerical simulations has become finer and finer, with ever increasing numerical capabilities. Nugent et al. (2014) used WRF (Weather Research/Forecasting Model) to study the tropical orographic convection in Dominica and the effects of wind speed on the generation of convection. High-resolution (~100 m) meso-scale simulations are necessary to capture the smaller-scale features that could influence the distribution of orographic-forced precipitation.

4.2 Numerical simulations of over the SO

In recent years a number of studies have been undertaken with numerical simulations of clouds and precipitation over the SO in the neighborhood of Tasmania (Morrison et al. 2010; Huang et al. 2014; 2015). These simulations have demonstrated limited skill in representing the boundary layer structure, including cloudiness, commonly citing a lack of skill in the reanalysis products employed for model initialization. Not surprisingly, the simulations presented herein also show limited skill in replicating some aspects of the surface observations, particularly precipitation. As our primary motivation is to study the orographic forcing, cases were selected to represent the common synoptic patterns discussed in Chapter 3 that give rise to various types of precipitation. Errors in the timing and intensity of the precipitation are not surprising nor of primary interest in this study.

4.3. WRF model setup

Given the importance of surface and boundary layer observations over Macquarie Island, it is necessary that we identify and appreciate any biases that may exist in these records arising from orographic forcing. In this study, a series of high-resolution (100 m) numerical simulations have been undertaken to investigate any orographic effect across a range of common meteorological conditions (i.e. warm front, cold front, mid-latitude cyclone and non-frontal transient drizzle). Surface precipitation, as measured at the ABoM station, is the primary focus of these simulations, given its necessity in closing the energy and water budgets over this region of the SO. The analysis is expanded to examine

orographic forcing to boundary layer winds, temperature, cloud cover and the generation of gravity waves across the island.

The Weather Research and Forecasting Model (WRF, version 3.5) is a sophisticated numerical model that solves the nonhydrostatic Euler equations in a terrain-following coordinate system (Skamarock and Klemp 2008). In this study, five domains centred on Macquarie Island with one-way nesting are configured with 70 vertical levels extending from the surface to approximately 5000 hPa over the ocean. The first five levels from the surface are set at 10, 41, 91, 152, 214 meters, and the vertical spacing continues to increase with the height to the top. The nested horizontal grid spacings of 9000, 3000, 1000, 333.33 and 111.11 m are set for domains of 100×100, 100×100, 199×199, 150×100, 100×100 grid points, respectively (Figure 4.1). Simulations were configured with the Rapid Radiative Transfer Model for GCMs (RRTMG) shortwave and longwave radiation scheme (Mlawer et al. 1997; Iacono et al. 2008), the Noah land surface model (Chen and Dudhia 2001), the Yonsei University (YSU; Hong and Lim 2006) planetary boundary layer (PBL) scheme, the Thompson (Thompson et al. 2008) microphysical scheme, and the Kain-Fritsch cumulus scheme (Ma and Tan 2009). Note that the cumulus scheme is used only on the coarsest domain. This setup has been chosen based on the previous WRF simulations over Tasmania and the SO in Huang et al. (2014). Terrain information is from the Shuttle Radar Topography Mission (SRTM; Farr et al. 2007), which includes digital topographic data for 80% of the Earth's land surface between 60° N and 56° S. For Macquarie Island, the horizontal resolution is 90 m.

The Year of Tropical Convection (YOTC; Moncrieff et al. 2012) data are used for initialization and boundary conditions. The YOTC database includes 6-hourly global analyses and over 30 model-based subgrid tendencies from ECMWF Integrated Forecasting System (IFS) on a 25-km grid (16 km for January 2010–April 2010) and 91 pressure levels for the 2-yr period May 2008–April 2010, with real field campaign focusing on the community interest and the common meteorological events.

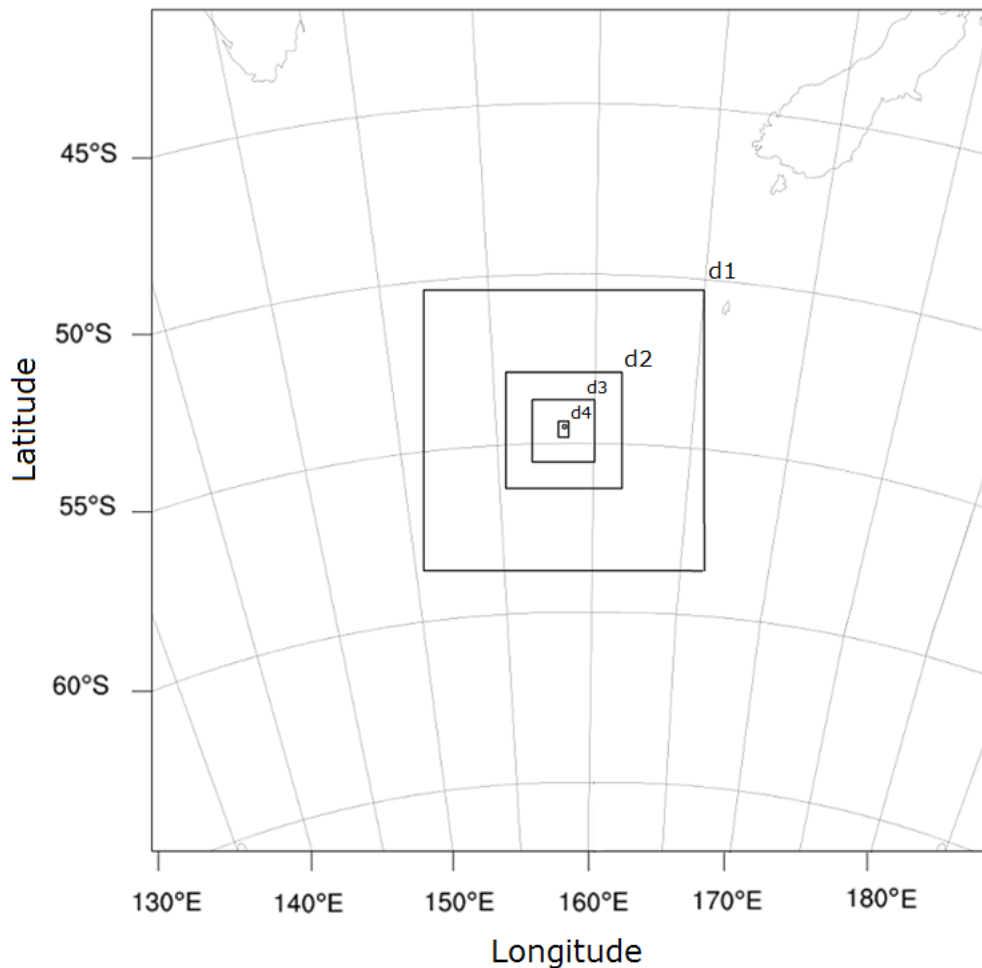


Figure 4.1. WRF domains used in this study

Neither the Reynolds-Averaged Navier-Stokes equation (RANS) models nor the

Large-Eddy Simulation (LES) models are fully appropriate for high-resolution simulations with the grid spacing of several hundred meters, as the size of energy-containing eddies is close to the model filter scale (Wyngaard 2004). Nevertheless, here we use the YSU scheme as a RANS-type turbulence closure for the innermost domain. In the YSU scheme, the turbulent fluxes in each model grid are estimated from the mean atmospheric variables and their gradients using the eddy diffusion equations. Nonlocal fluxes are also introduced in a parameterized nonlocal term (Hong and Lim 2006). Since the nesting is one-way, the spatial structures are always compared with lower resolution domains for consistency. The innermost domain is used only for exploration of the close surroundings of the weather station in two contrasting simulations: with and without terrain. The nearest grid-point to MAC in WRF simulation is used for the comparison with the surface observation.

The spin-up time in the simulations is 12 hours. Presented results are 12 hours after the initialization of the model unless stated otherwise. 100 m resolution is used in the simulation of cold front, warm front and drizzle case, with a 20-minute time interval, which is chosen for the accumulation of precipitation. A coarser resolution (1 km) with 1-hour time interval for accumulation of precipitation was used for the cyclone case, as this class does not significantly contribute to the total precipitation at the station (Figure 4.2).

4.4. Selection of case studies

Four case studies (Table 4.1), namely a cold front, a warm front, drizzle, and a mid-latitude cyclone, are chosen to represent the common synoptic

meteorology/precipitation types (Wang et al. 2015). Due to limited space, only the cold and warm frontal cases are presented in detail, as they are often associated with strong precipitation (Catto et al. 2012). The "cyclone" category differs from the frontal categories in terms of the significant wind pattern changes over the station associated with the passage of the low center. The four cases were simulated both with and without the Macquarie Island terrain such that any orographic effects on the airflow field and distribution of precipitation can be isolated.

| Case | Model start date | Time of simulation | Wind direction on 500m | Highest resolution (m) | Mean Wind speed (m s^{-1}) | Mean N (s^{-1}) | Fr (3-D) |
|------------|------------------|--------------------|------------------------|------------------------|---------------------------------------|----------------------------|----------|
| Cold Front | 2008-10-09 | 24h | NW | 100 | 24.8 | 0.0171 | 5.29 |
| Warm front | 2010-03-14 | 36h | W | 100 | 9.32 | 0.0196 | 1.90 |
| Drizzle | 2009-05-30 | 36h | SW | 100 | 14.8 | 0.0128 | 4.76 |
| Cyclone | 2009-05-06 | 24h | | 1000 | 9.19 | 0.0164 | 2.24 |

Table 4.1. A summary of WRF simulated cases

Both surface observations (Table 2.1) and upper air soundings are employed to evaluate the simulations. The frequency of the cases was discussed with the long-term MAC sounding records and the ERA-I product.

4.4.1. A cold front case

A cold front passed Macquarie Island from the west on 9 October 2008 (Figure 4.2) between 12:00 and 24:00 UTC, according to the ABoM MSLP. The surface observations of winds and pressure suggest that the major shift arrived at approximately 16:00 UTC (Figure 4.3) with a weaker, secondary shift arriving four hours later at 20:00 UTC. Ryan and Wilson (1985) reported similar multi-stage periods of convection during the passage of cold fronts over the SO, consisting of prefrontal mid-level cloud bands and a postfrontal low-level cloud band. The core of the cyclone is far to the south of MAC near the Antarctic coast, and a high pressure system is located over the Tasman Sea far to the north of the island. This case study offers an ideal, isolated frontal passage for study.

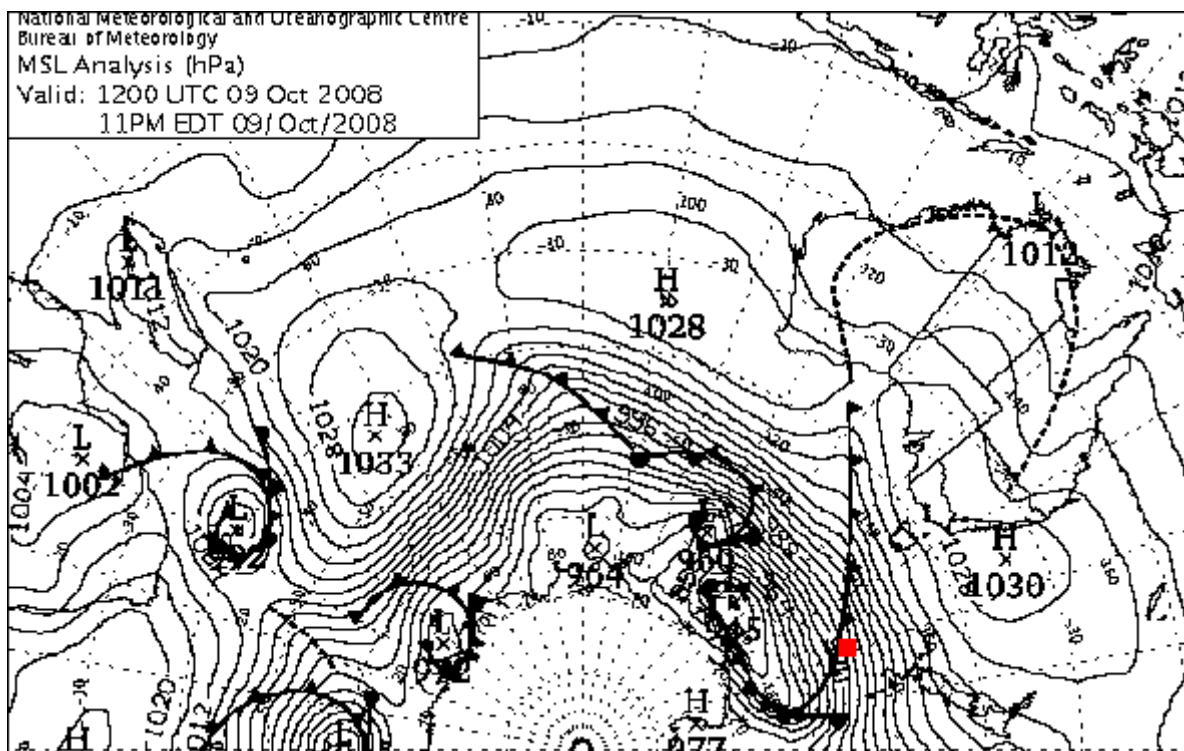


Figure 4.2. The ABoM Mean Sea Level Pressure (MSLP) chart showing a cold front passing Macquarie Island (the red point) at 12:00 UTC 9 October, 2008.

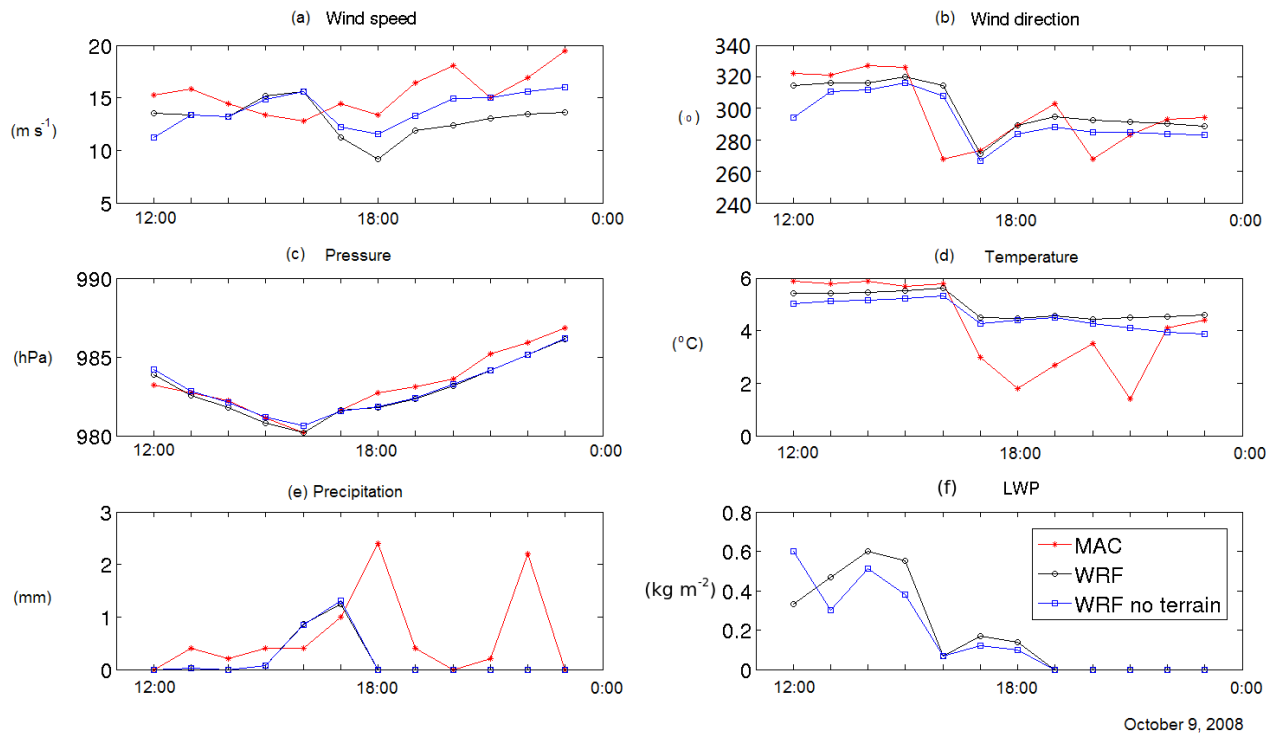


Figure 4.3. (a) 10 m wind speed, (b) wind direction, (c) surface pressure, (d) 2m temperature, (e) surface precipitation and (f) liquid water path from surface weather records (MAC), and 100 m resolution WRF simulations with and without terrain for the cold front case on 9 October, 2008.

The MODIS image of cloud-top temperature at 23:45 UTC reveals thick, cold (<228 K) cloud across the Tasman Sea (Figure 4.4). Lower/warmer and more broken cloud fields lie behind the main frontal clouds, which had passed Macquarie Island at the time of the image. The MAC sounding (Figure 4.5) is taken through a heavy pre-frontal cloud band at 12:00 UTC 9 Oct 2008, which is roughly four hours before the front arrives. Saturation is observed through the boundary layer up to a weak inversion, located near 850 hPa, with a moist free troposphere extending to over 600 hPa. Strong (~60 kts) westerly winds are recorded through the troposphere, as is common over the Southern Ocean

(Hande et al. 2012b). In spite of the saturated lower troposphere, no surface precipitation was recorded at this time (Figure 4.3e).

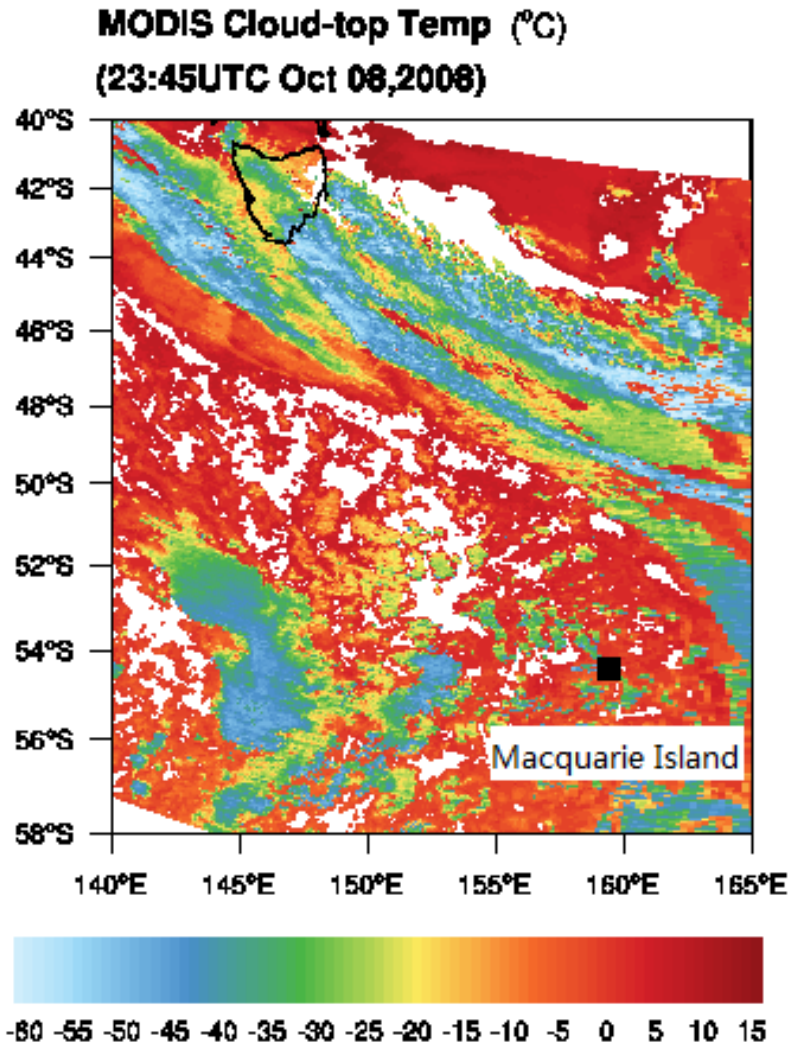


Figure 4.4. Cloud top temperature from MODIS for the cold front case at 23:45 UTC, 9 October 2008

we see that the simulation similarly produces a saturated environment up to roughly 850 hPa, albeit a few degrees colder. The free troposphere air immediately above the inversion is drier than observed. The simulated winds are roughly consistent with those observed. It is possible that there are important physical processes that are not being represented in the simulations. For example, it is possible that ice falling from upper level clouds could create a seeder-feeder effect to initiate/enhance precipitation, particularly in the neighbourhood of the fronts embedded in the storm track. The limited in-situ and remote observations available are not sufficient to either confirm or reject such a hypothesis.

Turning now to the simulated surface meteorology (Figure 4.3), some discrepancies are immediately evident. The timing of the initial frontal passage at 16:00 UTC is captured reasonably well, but the intensity of the simulated temperature drop and wind shift is somewhat weaker than observed. Also the peak precipitation rate is roughly half of that observed and arrived roughly an hour too early. However, the secondary shift in the winds and temperature is completely missed in the WRF simulation. No precipitation was simulated through this time, either, contrary to observations. As a general summary, the WRF simulation is able to capture the major meteorological aspects of this frontal passage, although the simulation underestimates the amount of surface precipitation and it completely fails to capture a second stage to the frontal passage.

Leaving the physical observations behind, the sensitivity of the WRF simulations to the terrain is now explored. First and foremost, no significant difference,

compared to WRF no-terrain simulation, is observed in the surface precipitation through the duration of the simulations. Weak differences are apparent in the winds and temperature with wind speed arguably showing the greatest difference between the terrain and no-terrain simulations. In particular, the winds in the noterrain case shift to a more westerly heading after the initial frontal passage at 16:00 UTC. The simulated liquid water path above the station is also examined, although there are no physical observations available for evaluation purposes. Liquid water path (LWP) is the measure of the weight of the liquid water droplets in the atmosphere above a unit surface area on the earth, given in units of kg m^{-2} (Burrows et al. 2011). LWP in these simulations is shown in Figure 4.3f to represent the development clouds. It is interesting that in the pre-frontal simulation period before 16:00 UTC, the simulated liquid water path is relatively large and large discrepancies are shown between the two simulations. These differences effectively cease with the frontal passage at 16:00 UTC, with only weak differences thereafter. The simulations produce virtually no clouds after 19:00 UTC (Figure 4.3f), consistent with the absence of any surface precipitation in the simulations.

Looking beyond the surface station, we now examine the orographic effects on other parts of the island. The orographic effects on the distribution of precipitation and the wind field are evident in the lee of the island at the time of frontal passage at 16:00 UTC (Figure 4.6). The accumulated precipitation over 20 minutes is presented to smooth over high frequency oscillations yet still be short enough to reflect the connection to the dynamics. The simulated front arrives from the west with relatively intense precipitation, separating the wind field into

two regions (Figure 4.6a). Although there is no difference in simulated precipitation at the MAC station with or without terrain, the precipitation is enhanced immediately in the lee of the island and reduced further downwind (Figure 4.6b) when the terrain is included. Figure 4.6c (and 4.6d) shows the wind field and precipitation (and difference) from the highest resolution domain (100 m), noting no difference in the immediate neighbourhood of the surface site.

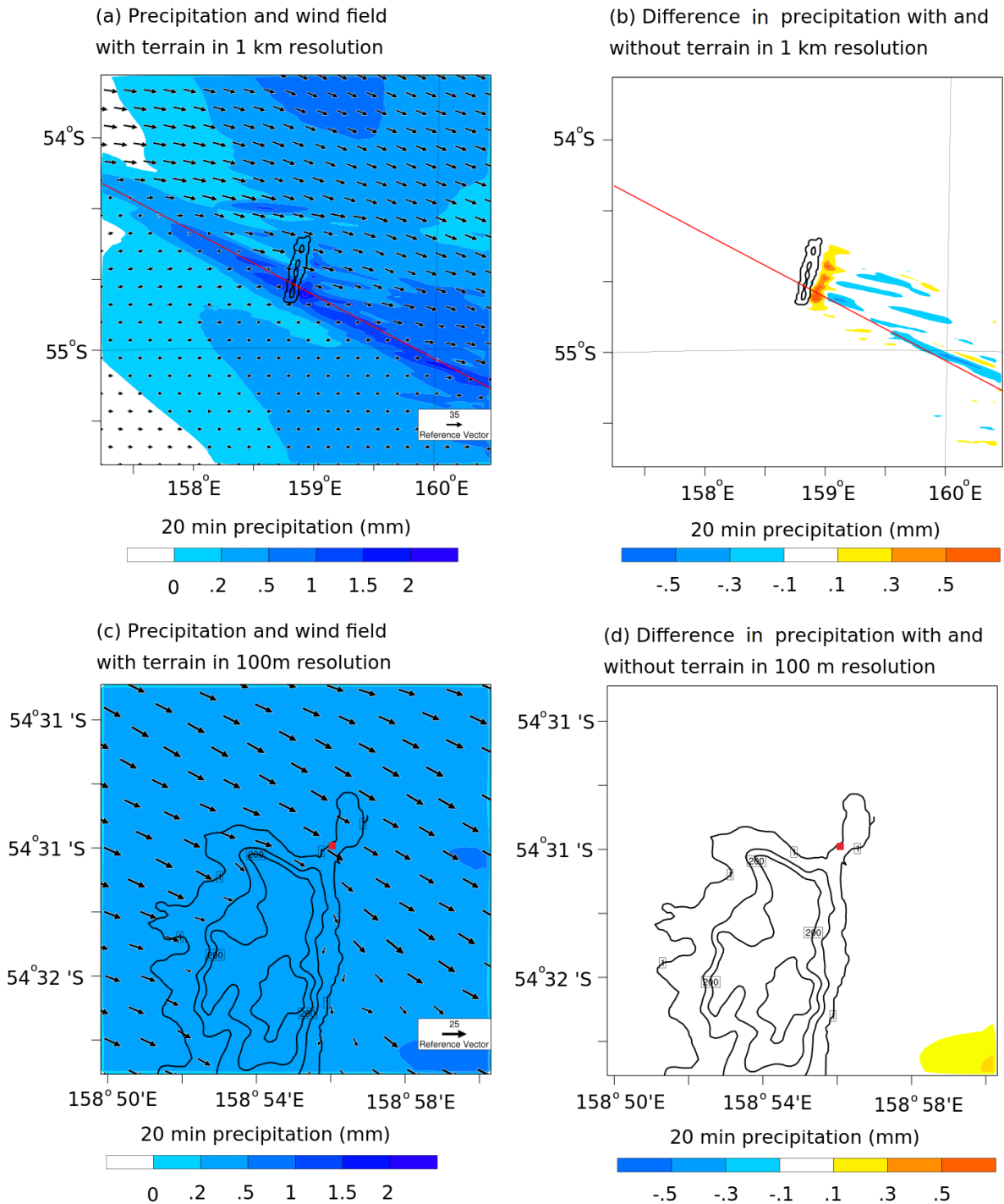


Figure 4.6. Precipitation and wind fields from WRF simulations for the cold front case at 16:00 UTC 9 October, 2008. (a) The 20 min surface accumulated precipitation and the wind field from the 1 km domain at 300 m above ground. (b) The differences of the precipitation between the simulations with and without

terrain for the same domain (using precipitation in no terrain simulation subtract from precipitation in the terrain simulation). Red lines within Figure 4.6 (a and b) denote the cross sections shown in Figure 4.7. (c) and (d) The corresponding precipitation and the surface wind field from the 100 m domain at 50 m above ground. The red squares mark the location of the MAC station.

In order to better understand the mechanism of the orographic enhancement on the precipitation, variables (shown in Figure 4.7) in the cross section across the most precipitating area (indicated in Figure 4.6) have been studied. A shallow convective system associated with warm rain below 1 km (Figure 4.7a), liquid water below 2 km (Figure 4.7c), ice between 4 and 6 km (Figure 4.7e) and upward vertical motion (Figure 4.7g) is passing over the island from the west. We can see the lee-side enhancement of the precipitation simulation with terrain (Figure 4.7a). Differences in the leeward rain field are closely correlated to the differences in the warm cloud field (Figure 4.7d and 4.7f), while the ice clouds do not contribute to evident precipitation. Looking at the vertical velocity (Figure 4.7e), we see that the island sets off relatively weak gravity waves in the lee of the island. These gravity waves propagate roughly 60 km downwind from the island in the simulations (Figure 4.7g) accounting for the differences in the cloud field and the precipitation. The enhancement of precipitation caused by lee-side convergence, is consistent with the enhanced clouds and ice over the top of island and transported by the strong wind. The Froude number (3-D) in this case is as large as 5.26 from the simulation, which is consistent with precipitation advection as well as the wide spread gravity waves on the downwind side.

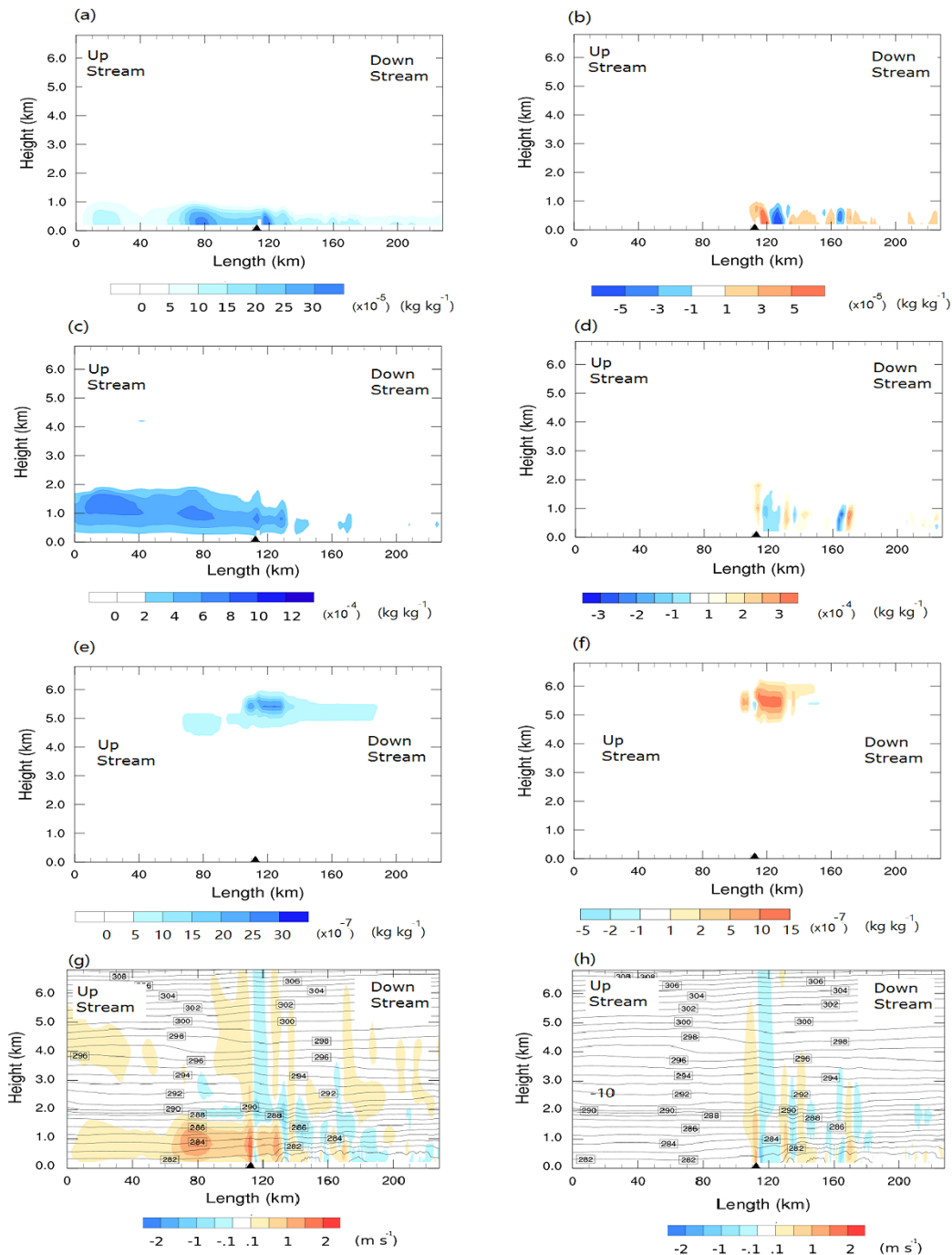


Figure 4.7. (a) Rain mixing ratio, (c) liquid water mixing ratio, (e) ice mixing ratio, and (g) vertical wind speed with potential temperature cross sections from the 1 km domain simulation (with terrain) in the cold front case at 16:00 UTC, 9 October, 2008. Differences in the simulations with and without terrain are shown in the right column (b, d, f, h).

Wind speeds in the WRF simulation without terrain are largely consistent with the MAC sounding and ERA-I results, and higher than that with the terrain below 500m, which is comparable with the island height (Figure 4.8a). Both the WRF simulation with terrain and the MAC sounding show the wind is from northwest on the surface and turns gradually to the west on 1000 m, which is underestimated by ERA-I and missed by the WRF simulation without terrain.

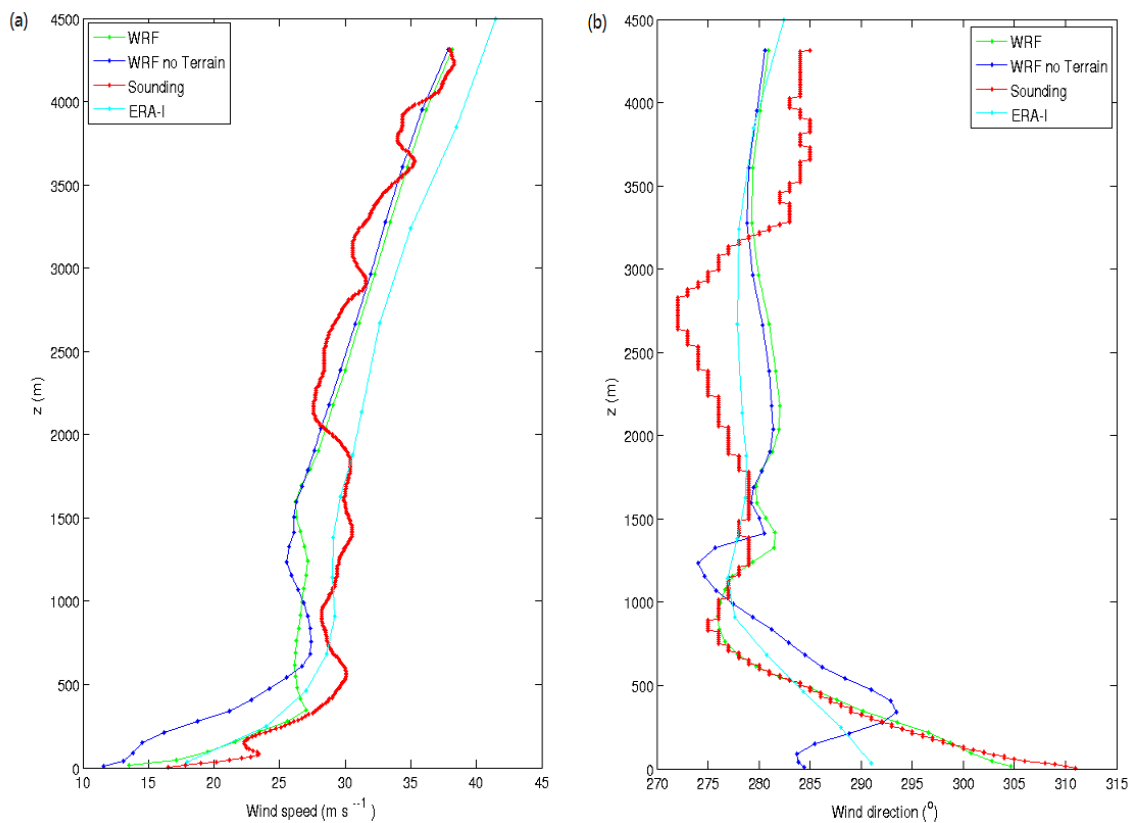


Figure 4.8. (a) The wind speed and (b) wind direction from 100 m domain WRF simulations, MAC sounding and ERA-I over the station at 12:00 UTC, 9 October, 2008.

During the post-frontal period, the simulation with terrain produces neither cloud field nor precipitation (Figure 4.9), yet for this case study, the MODIS

imagery (Figure 4.4) clearly reveals warm, low-level clouds in the post-frontal environment. Huang et al. (2014) noted difficulty in WRF simulation of boundary layer clouds over the Southern Ocean in the neighbourhood of Tasmania. They suggested that the model deficiency may be associated with the insufficient surface moisture flux. Given our simulations' failure to generate clouds in this post-frontal period, it is not possible to comment on any orographic impact on altering the precipitation intensity or distribution. We do note, however, that while clouds were evident from MODIS in the post-frontal period, the observed surface precipitation was very weak after the passage of the second stage of the front around 23:00 UTC. The Froude number (3-D) was 4.86 from the simulation, with gravity waves propagating roughly 30 km downwind from the island in the simulations (Figure 4.10).

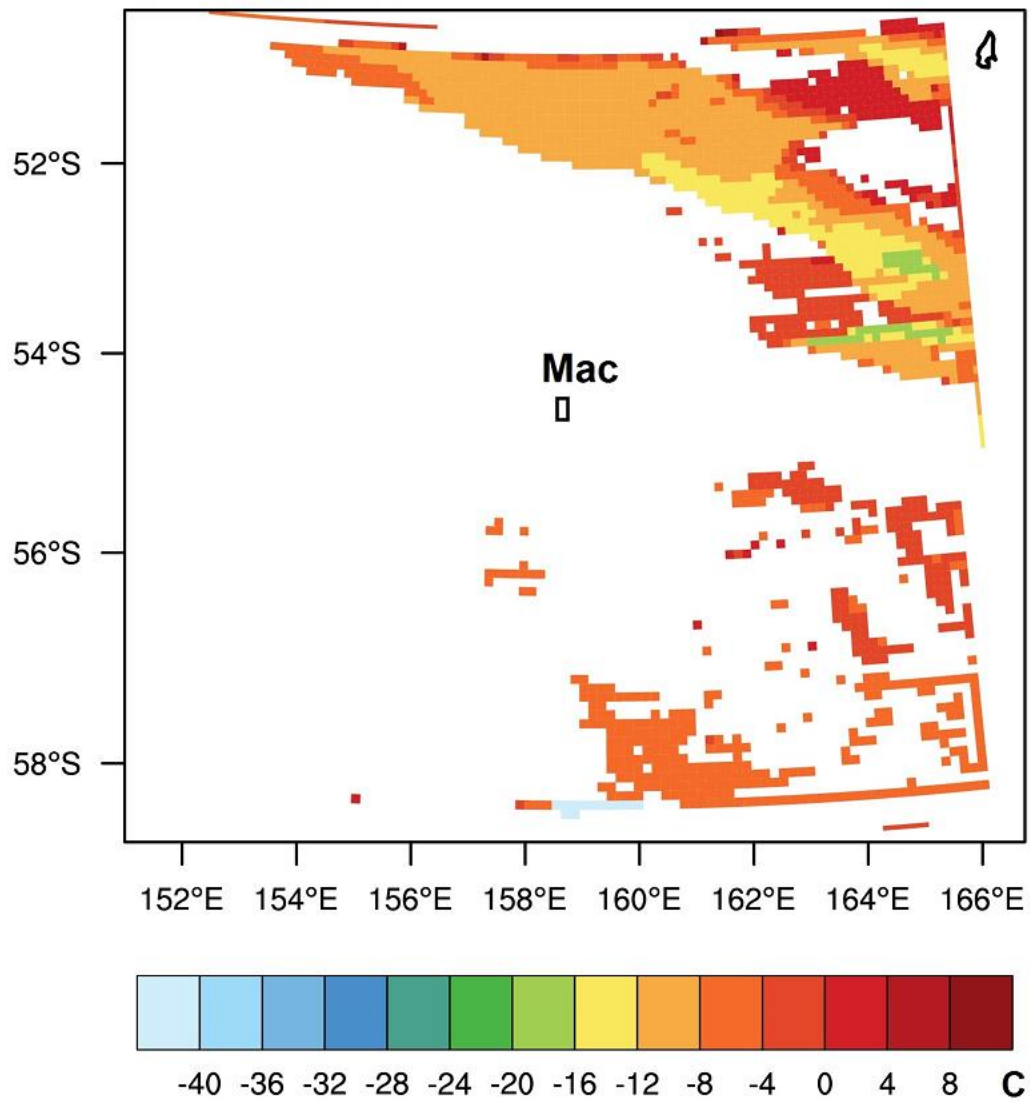


Figure 4.9. Cloud-top temperature over Macquarie Island at 23:00 UTC 9 October, 2008, from 1km resolution WRF simulation with terrain.

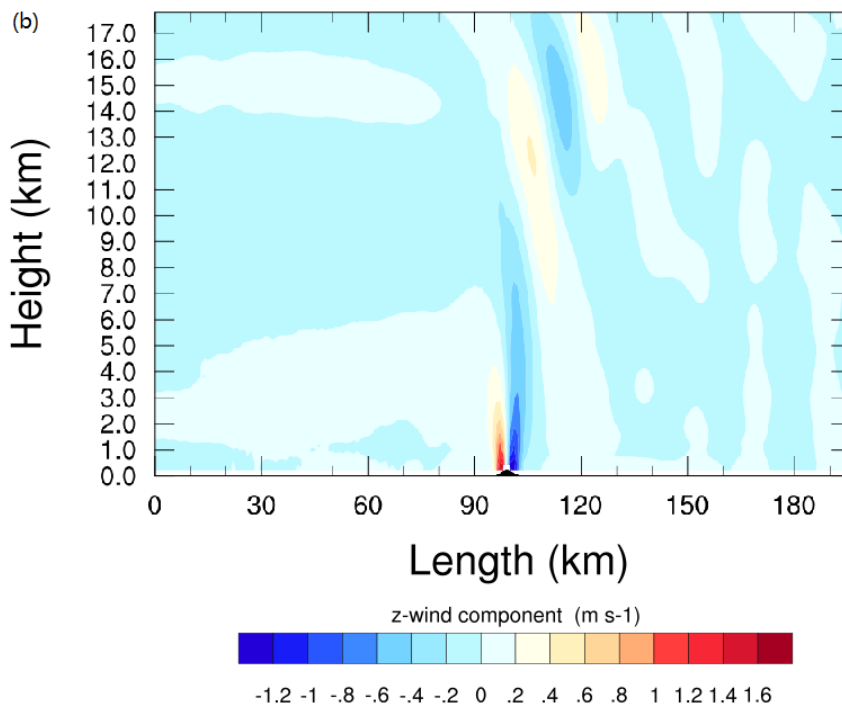
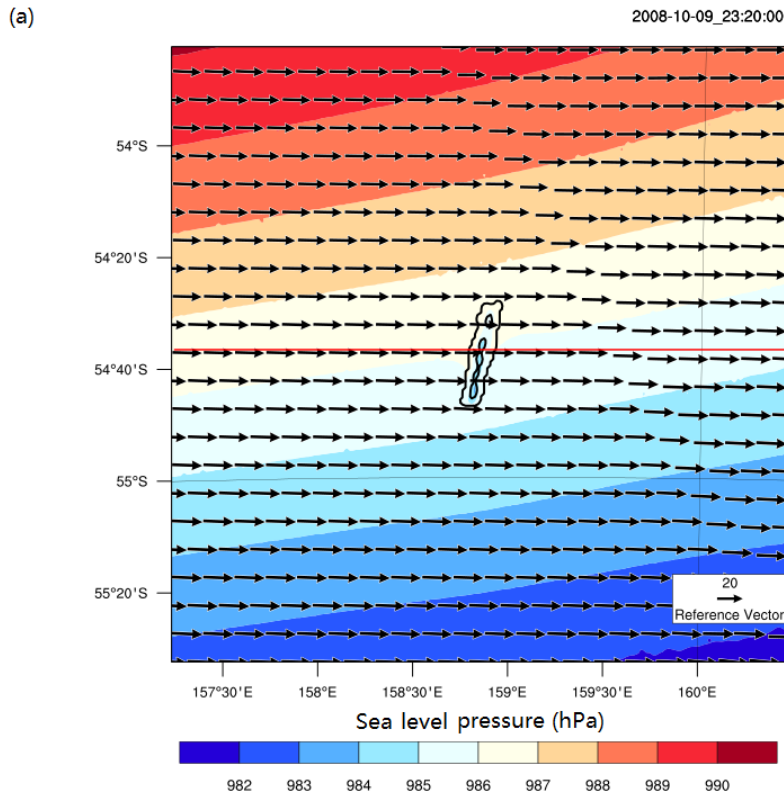


Figure 4.10. (a) The horizontal wind field at 500m height and the sea level pressure from the 1 km simulation domain (with terrain). Red line within Figure

4.10a denotes the cross section shown in Figure 4.10a. This cross section has been chosen along the wind direction to show the downwind gravity waves. (b) Longitudinal section of the vertical wind from the 1 km simulation domain (with terrain) at 23:20 UTC 9 October, 2008.

As a general summary, the WRF simulation is able to capture the major meteorological aspects of this frontal passage, although the simulation underestimates the amount of surface precipitation and it completely fails to capture a second stage to the frontal passage. The enhancement of precipitation in the lee is caused by the downwind transportation of the water droplets from the enhanced clouds over the top of island. The pre-frontal Froude number (3-D) from the simulation is as large as 5.26, which indicates that the air flow passes over the island and leads to the precipitation advection as well as the widely spread gravity waves on the downwind side.

4.4.2. A warm front case

A warm front crossed Macquarie Island between 14 and 15 March 2010, arriving at roughly 0:00 UTC. The warm air pushes from the northwest at 2 m height (Figure 4.11a). (The ABoM MSLP for this case has been omitted, as no warm front was analysed given the remote location over the Southern Ocean.) At this time, the core of the cyclone is about 4 degrees to the west of Macquarie Island (Figure 4.11b). The MODIS image (22:00 UTC 14 March 2010) reveals cloud-top temperatures below 252 K over Macquarie Island, presumably from the large scale ascending motion (Figure 4.12).

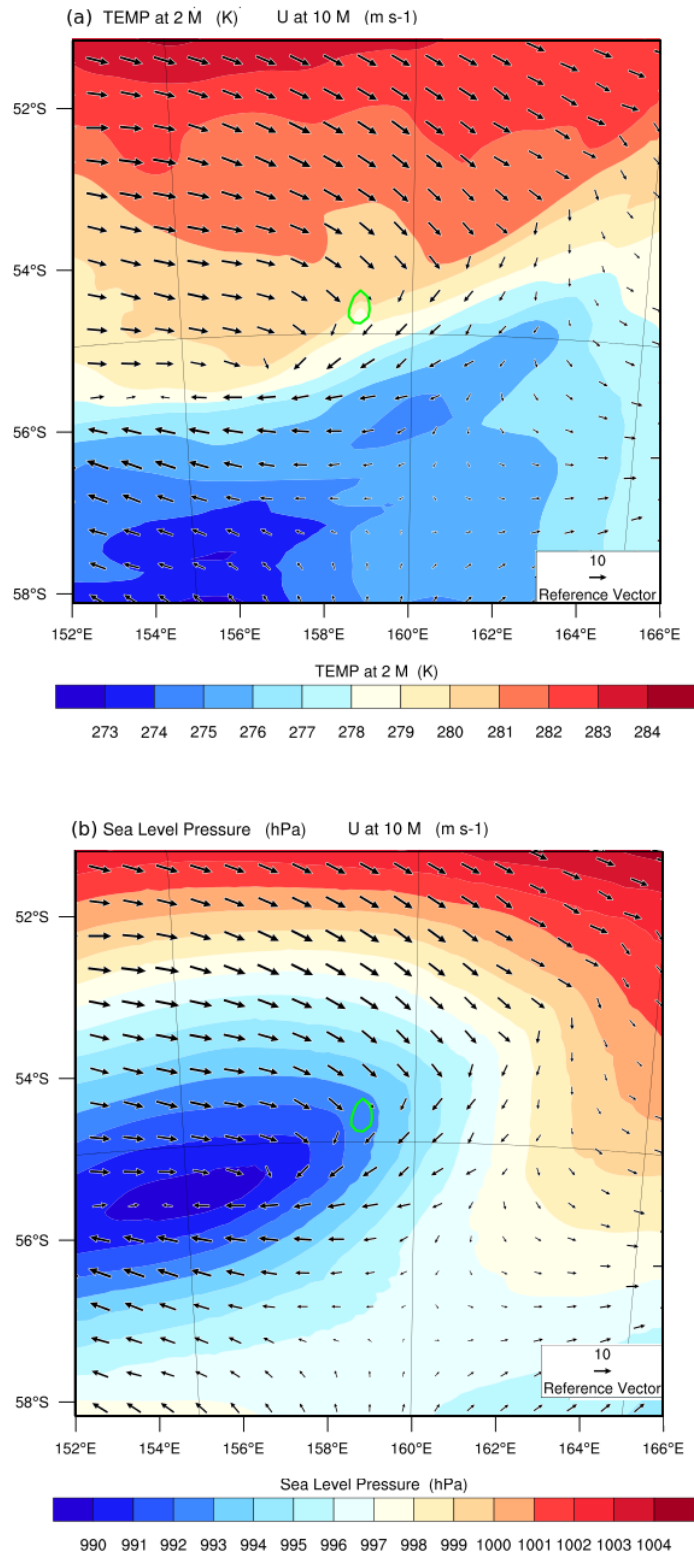


Figure 4.11. 2 m temperature (a) and MSLP (b) of a warm front passing Macquarie Island (the green circle) at 00:00 UTC 15 March 15 2010 from the 9 km WRF simulation.

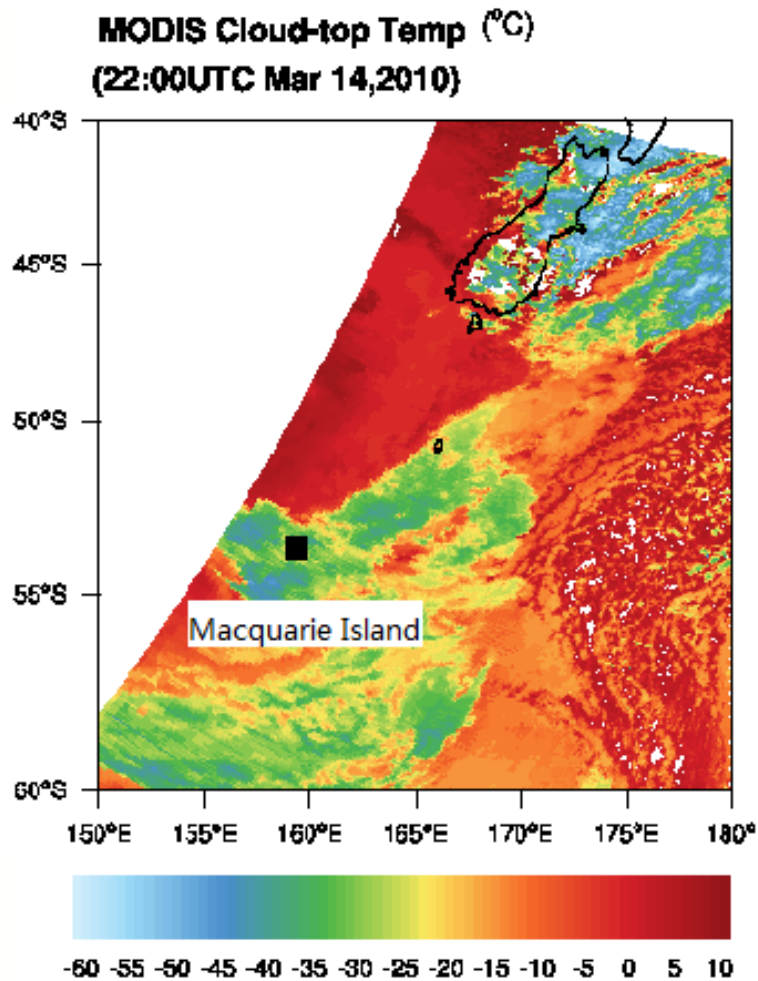


Figure 4.12. Cloud top temperature from MODIS at 22:00 UTC 14 March, 2010, with a warm front passing Macquarie Island (the black square).

From the 23:00 UTC 14 March 2010 sounding (Figure 4.13), a temperature inversion is evident at around 2 km (~800 hPa). Below this inversion, the air is saturated and stable. Above this inversion, the air remains saturated with the cloud field extending to heights of over 4 km. The wind direction changes from northwest to west from the surface to 2 km height and then remains westerly through the rest of the free troposphere.

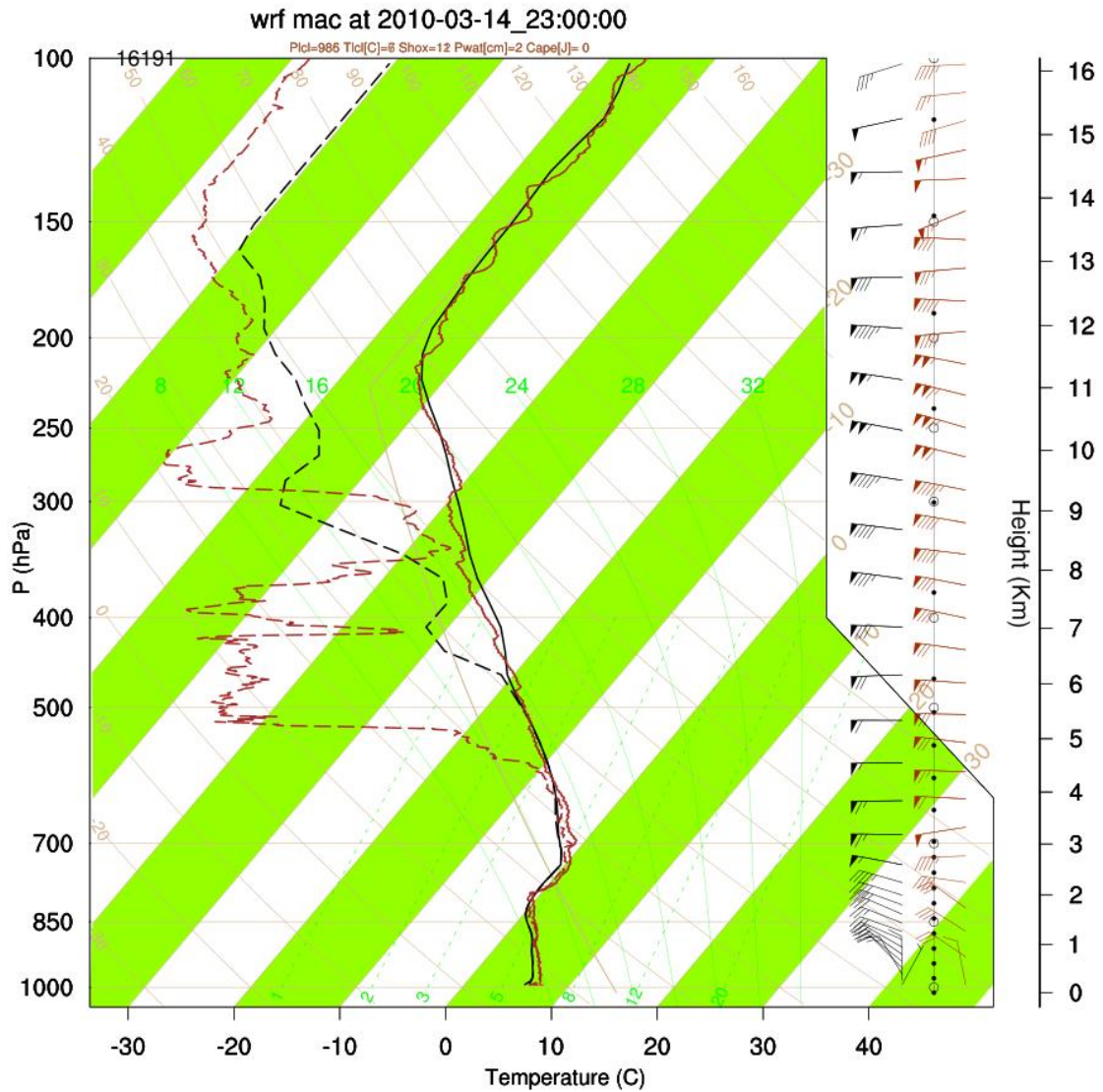


Figure 4.13. The Skew-T chart from the sounding (brown) and 100 m resolution WRF simulation with the terrain (black) for the warm front case at 23:00 UTC, 14 March, 2010.

Focussing on the surface observations (Figure 4.14), the precipitation begins at 16:00 UTC and reaches the maximum (2.7 mm h^{-1}) at 0:00 UTC, then decreases dramatically. The wind speed is around 5 m s^{-1} before 23:00 UTC, then increases

to above 10 m s^{-1} after the front. Later, at 08:00 UTC, the surface winds peak at $\sim 20 \text{ m s}^{-1}$. The surface winds are from the west before 18:00 UTC and then briefly become westerly (less than 5 m s^{-1}) and northerly in a transient wind field until 22:00 UTC. After the warm front passes Macquarie Island at $\sim 23:00$ UTC, the wind direction changes back to the west (Figure 4.14b). As the warm front approaches the station from 20:00 UTC 14 March to 00:00 UTC 15 March, the surface temperature increases from 4 to 8° C . The pressure decreases throughout much of this 24-hour period from 1005 to 985 hPa, reflecting the approaching cyclonic core.

Using these limited observations to evaluate the WRF simulation, we note the strong agreement in the sounding from the surface up to heights of 4 km (Figure 4.13). Above this height, the simulation is too moist with clouds inferred up to the further height of 6 km. Apparently, the deeper cloud in the WRF simulation does not lead to more precipitation. The simulated precipitation is largely consistent with the observations, although the peak intensity is slightly underestimated (2.0 mm hr^{-1}) and arrives an hour earlier at 23:00 UTC. The simulated pressure and temperature agree well with the observations.

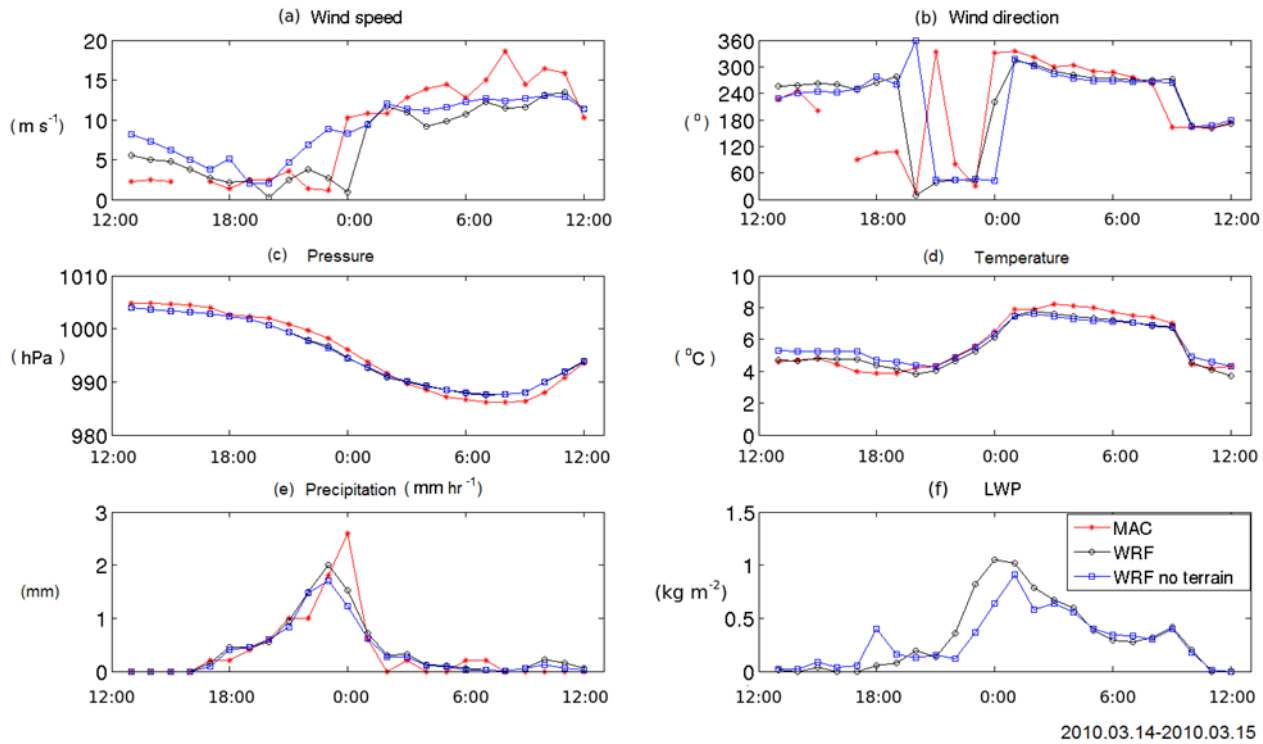


Figure 4.14. Wind speed, wind direction, pressure, temperature precipitation and liquid water path from surface weather records (MAC), and 100 m resolution WRF simulations with terrain and without terrain in a warm front case from 12:00 UTC 14 March, 2010 to 12:00 UTC 15 March, 2010.

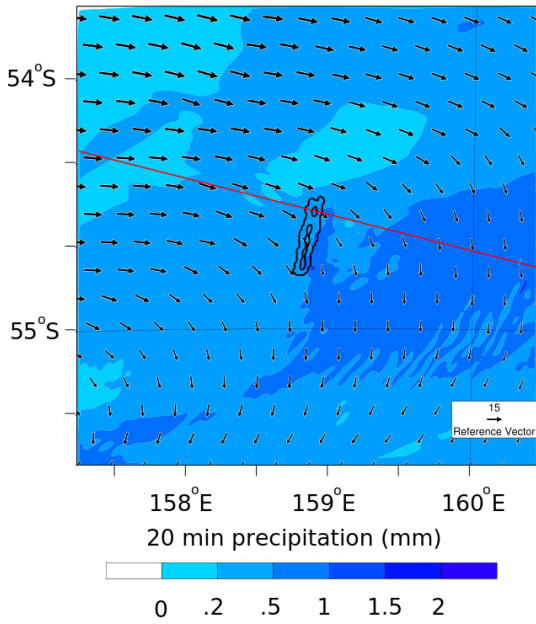
The simulation shows some skill in reproducing the surface wind (Figure 4.14a) except the wind direction shift occurred slightly earlier than observed (Figure 4.14b), and the simulated wind direction shift with terrain is one hour ahead of that without terrain. Looking at the difference between the simulations, the northerly wind is evidently blocked by the island from roughly 21:00 to 23:00 UTC, as seen from the lower wind speed with the terrain. Both the pressure and the temperature from the simulation and MAC match well (Figure 4.14c and 4.14d). The two simulations show that the clouds above the station are enhanced by the terrain (Figure 4.14f), especially when the winds are from the north, with

liquid water path increased by 0.4 kg m^{-2} at 00:00 UTC.

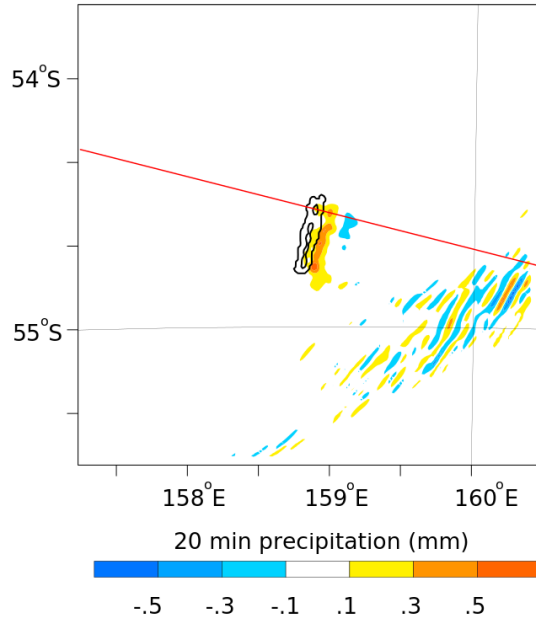
As before, the orographic effect is isolated by running two sets of simulations, with and without terrain. Again, the terrain effects are negligible on the surface precipitation at the station except for a slight enhancement from 22:00 to 00:00 UTC (Figure 4.14e) when the winds are from the north and northeast. Overall, the terrain effects in this case are stronger than in the first case, but the differences between the accumulated precipitation in the simulations with and without terrain is only approximately 5%, although the peak is increased by 12% in the 100m simulations at 22:00 UTC.

We now move away from a site-based analysis to a spatial-based analysis in order to examine the regional impacts of topography within the model. An orographic effect is observed on the surface precipitation immediately in the lee of the island, similar to the cold front case (Figure 4.15). At 23:20 UTC the warm front has just passed over the island and the wind has shifted back to the northwest and west. Precipitation is enhanced immediately downwind of the island. Consistent with the single point comparison (Figure 14), the MAC station is near the region of precipitation enhancement but is largely unaffected by the terrain (Figure 4.15d). The wave-like pattern in the lower right part of Figure 4.15b is caused by the horizontal displacement of the main convection system between the two simulations, which is with fragmental edge and very sensitive to perturbations.

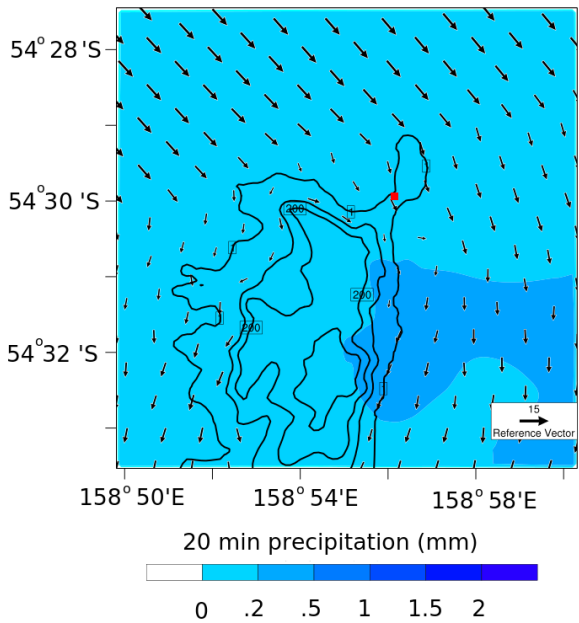
(a) Precipitation and wind field with terrain in 1 km resolution



(b) Difference in precipitation with and without terrain in 1 km resolution



(c) Precipitation and wind field with terrain in 100m resolution



(d) Difference in precipitation with and without terrain in 100 m resolution

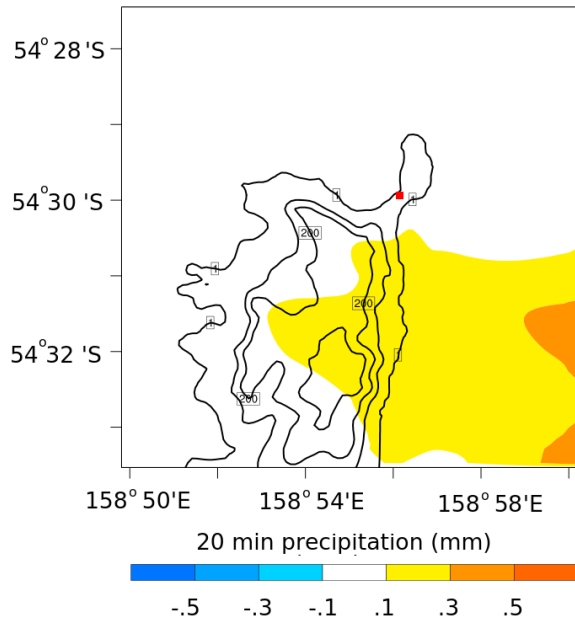


Figure 4.15. Precipitation and wind fields from WRF simulations for the cold front case at 23:20 UTC, 14 March, 2010. (a) The 20 min surface accumulated precipitation and the wind field from the 1 km domain at 300 m above ground. (b) The differences of the precipitation between the simulations with and without

terrain for the same domain (using precipitation in no terrain simulation subtract from precipitation in the terrain simulation). Red lines within Figure 4.15 (a and b) denote the cross sections shown in Figure 4.16. (c) and (d) The corresponding precipitation and the surface wind field from the 100 m domain at 50 m above ground. The red squares mark the location of the MAC station.

As in the previous case study, the structure of the frontal system at 23:20 UTC is further explored through a cross section (shown in red line within Figure 4.15a, b) along the mean postfrontal wind. This cross section also passes through the perturbation area of the precipitation. Downwind of the island, the simulations produce very shallow clouds and warm rain in the lowest kilometre and ice clouds between 3 and 7 km. Upwind of the island, the warm air is pushing up over the colder boundary layer air and clouds climb above 2 km in depth (Figure 16c). The airflow upstream is weakly blocked by the island (Figure 16h), which causes weak vertical motions that appear from approximately 10 km upwind from the island. Stronger vertical motions are triggered directly over the island, with clouds, ice and precipitation advected to the lee. The gravity waves are weaker and have not propagated far downwind horizontally along this cross section. We note that given the strong wind shifts occurring through this case study, the 'downwind' section of the cross section does not capture the air mass that had passed over the island.

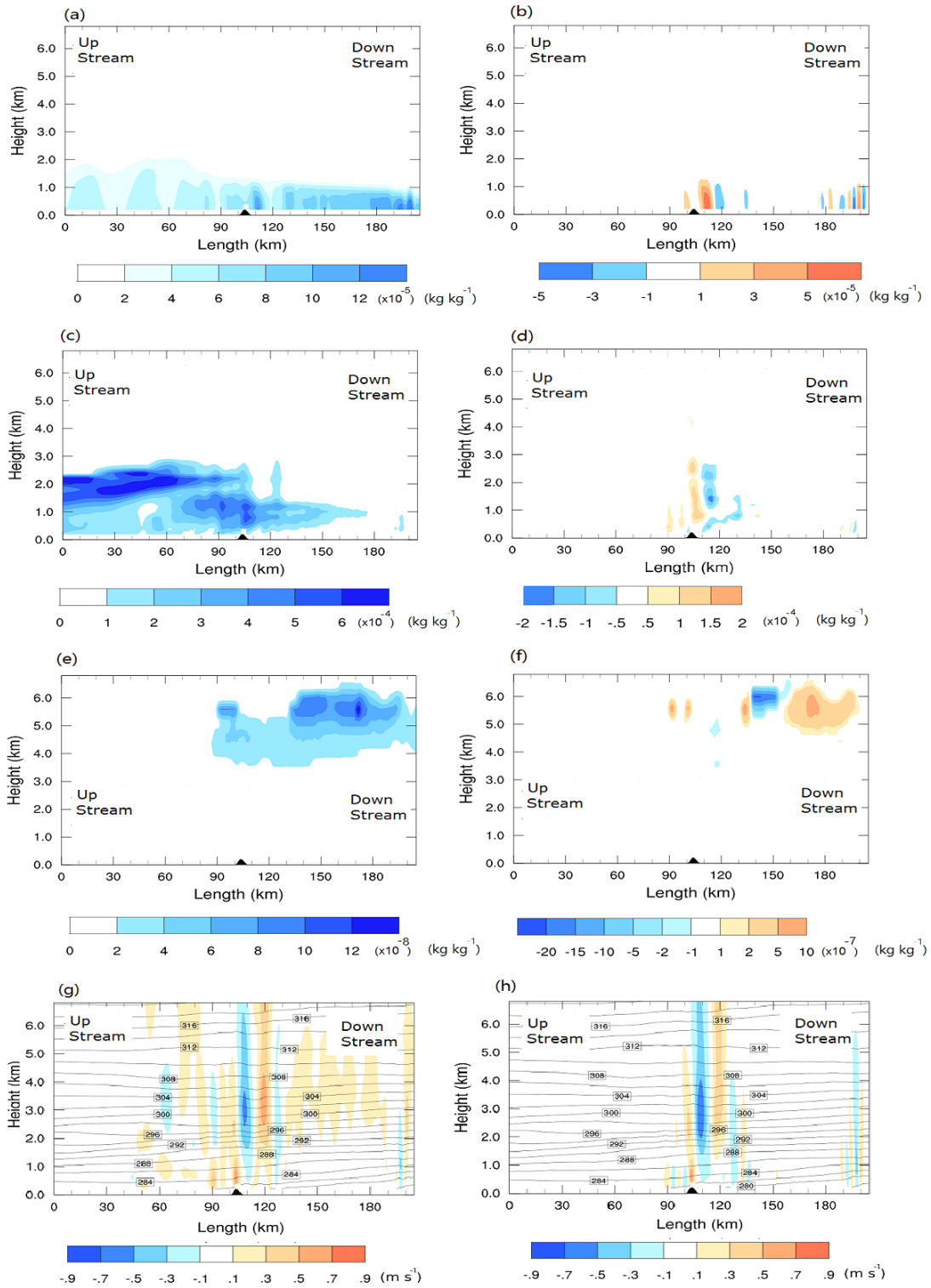


Figure 4.16. (a) Rain mixing ratio, (c) liquid water mixing ratio, (e) ice mixing ratio, and (g) vertical wind speed with potential temperature cross sections from the 1 km domain in the warm front case (with terrain) at 23:20 UTC, 14 March,

2010. Differences between the simulations with and without terrain are shown in the right column (b, d, f, h).

The Froude number (3-D) is 1.90 for this warm front case simulated at 23:00 UTC, which is considerably smaller than for the first case study. Looking at a later time (4:00 UTC, Figure 4.17), gravity waves are observed to have propagated approximately 60 km downwind.

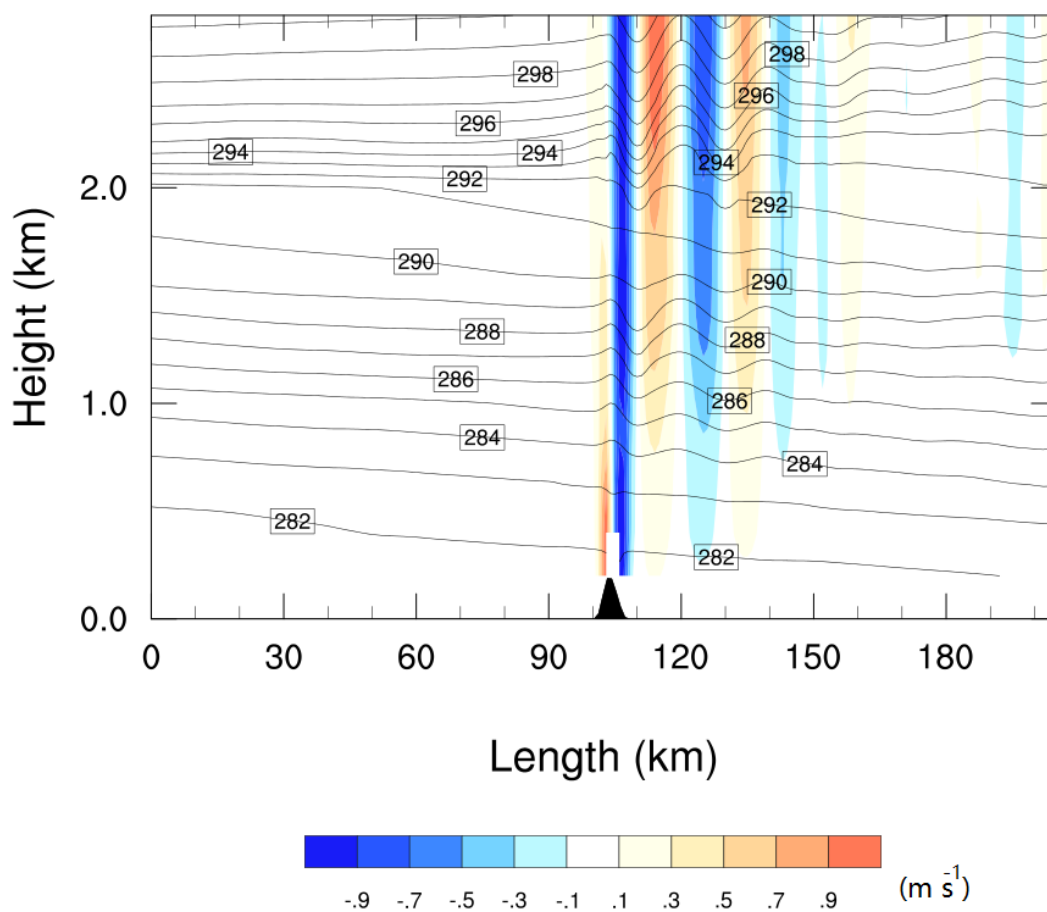


Figure 4.17. Vertical wind speed with potential temperature at 4 UTC, 14 March, 2010, from 1km resolution WRF simulation with terrain.

Looking up through the atmospheric column above MAC we find that the wind speeds from the WRF simulation with terrain are higher than those from the

WRF simulation without terrain (Figure 4.18a). The MAC sounding records are comparable with the wind speeds from the WRF simulation with terrain below 200 m, while more consistent with wind speeds from the WRF simulation without terrain from 200 m to 800 m, which suggests the terrain effects are slightly overestimated from 200 m to 800 m. ERA-I underestimates the wind speeds on all levels below 4000 m. The wind directions from all the products are largely consistent because the wind speeds are low and the terrain effects are weak (Figure 4.18b).

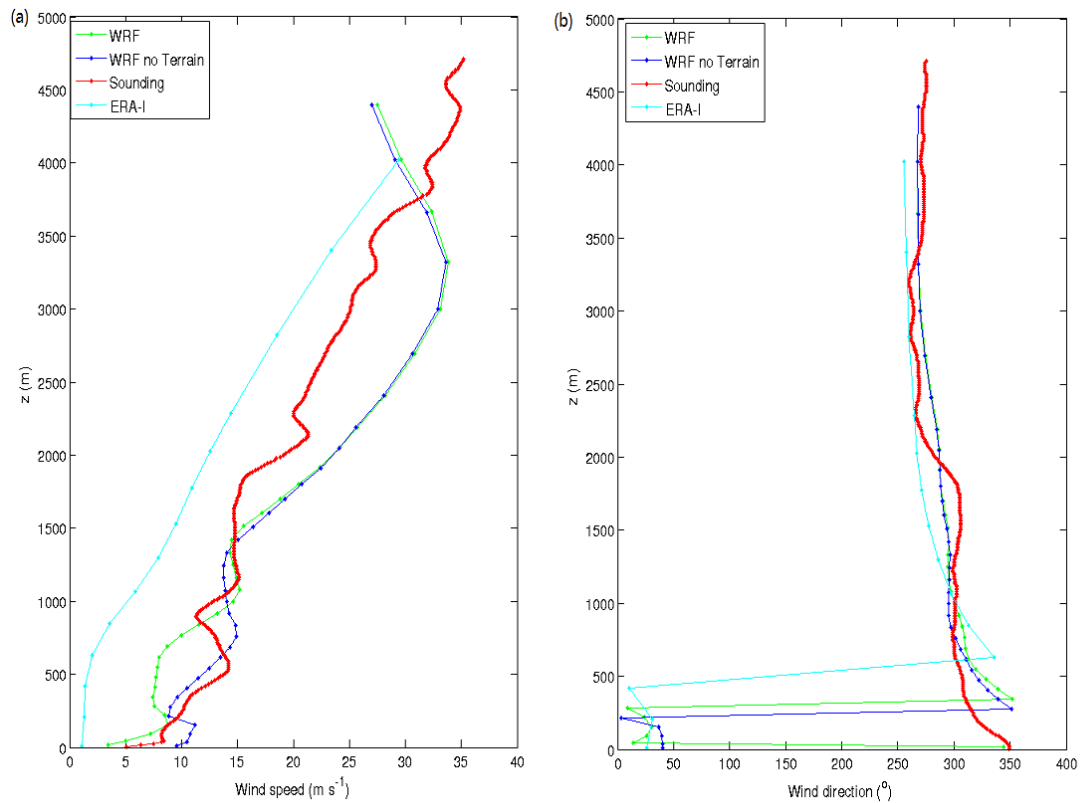


Figure 4.18. (a) wind speed and (b) wind direction from 100 m domain WRF simulations, MAC sounding and ERA-I over the station at 23:00 UTC, 14 March, 2010.

In summary, the simulation of the warm front precipitation is largely accurate

except for a slight underestimation of the precipitation peak at 23:00 UTC, while the wind direction simulation has larger errors around 18:00 UTC when the wind speed is less than 5 m s^{-1} . The Froude number (3-D) in this case is 1.90 from the simulation. The gravity waves are also triggered by the terrain. During the front passage, the gravity waves are weaker than those in the first case and propagate less than 50 km on the leeward side (Figure 4.17), due to the wind direction change, while they are observed to have propagated 60 km downwind 4 hours later. The orographic effect on the precipitation observed at MAC station, again, is negligible.

4.4.3. A drizzle case

The last two cases are both with wind from the open sea (north or west), while the main obstacle is on the south of the station. Fronts from the south are rare, so a non-frontal drizzle case on 30 May, 2009 was studied (Figure 4.19). A high-pressure system (sea surface pressure = 1042 hPa) is to the northwest of Macquarie Island, driving the wind from the southwest. The boundary layer is thinner than 1 km with wind shift from southwest near the surface to south on the top (Figure 4.20).

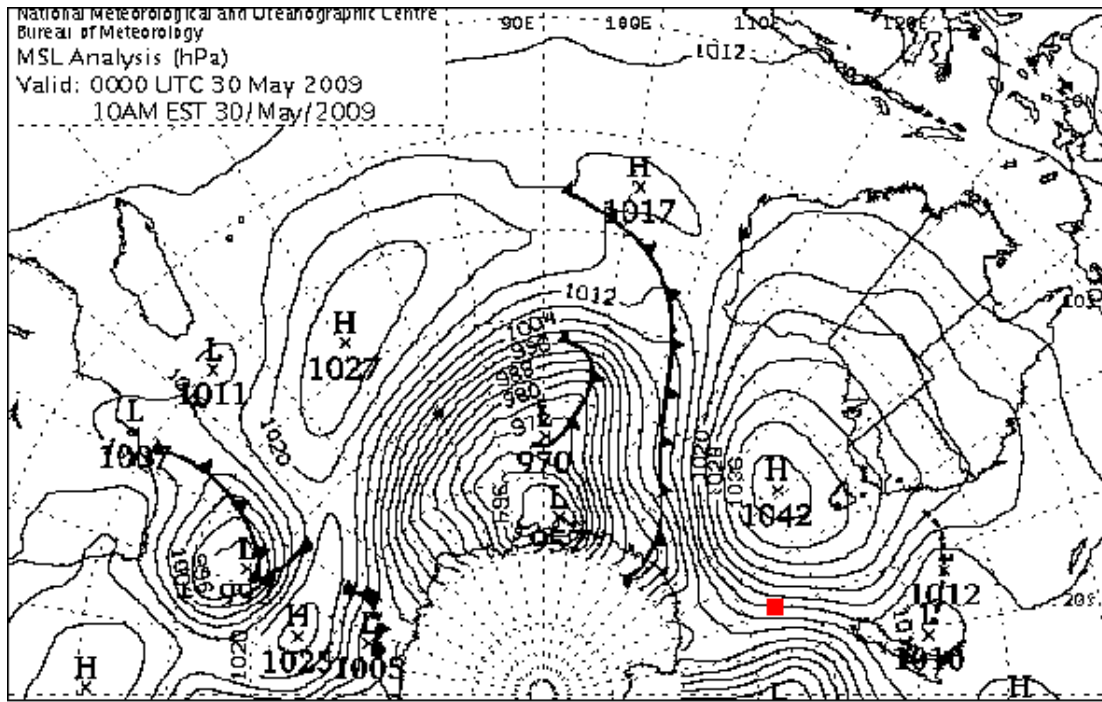


Figure 4.19 The ABoM Mean Sea Level Pressure (MSLP) chart of synoptic weather near Macquarie Island (the red point) at 00:00 UTC 30 May, 2009.

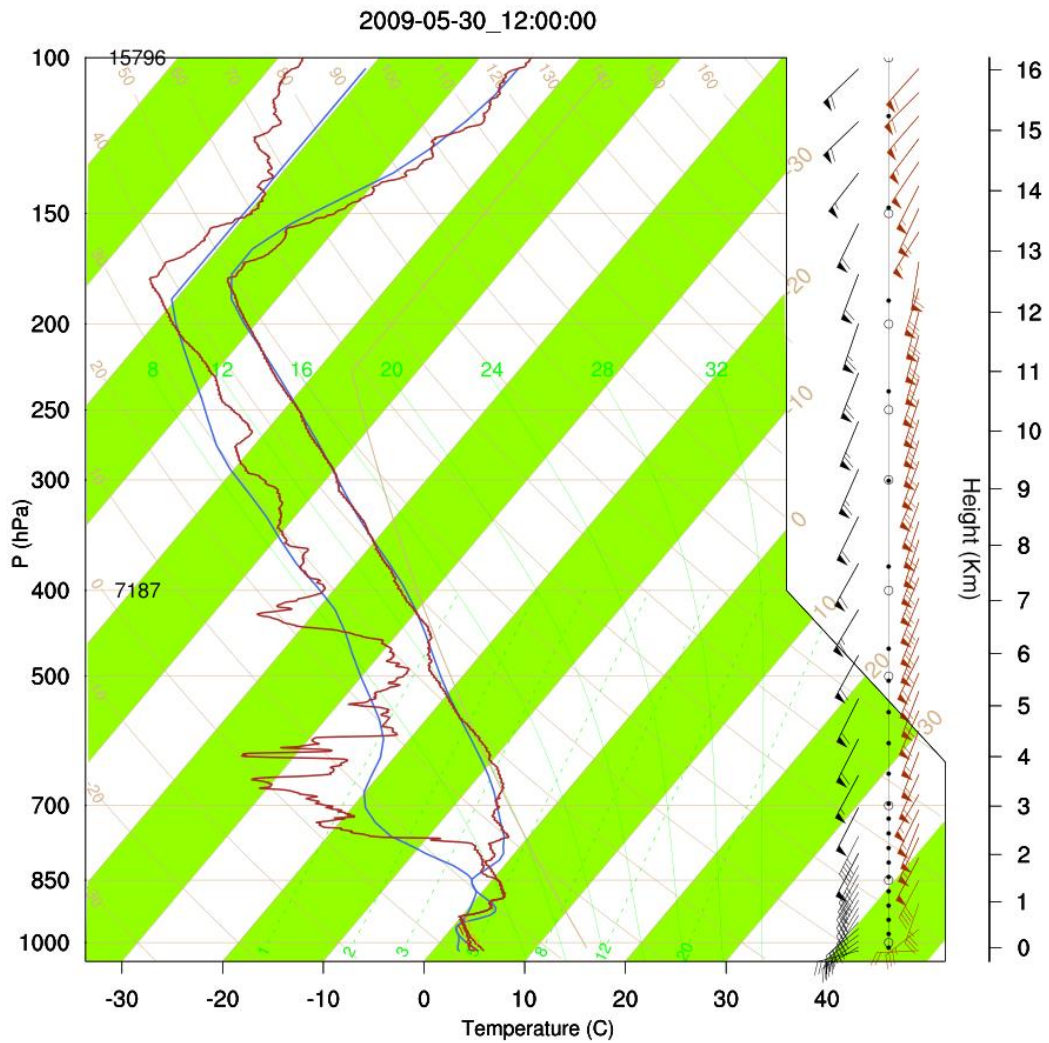


Figure 4.20. Skew T chart from sounding data (brown) and WRF simulation (blue) in a drizzle case, at 12 UTC 30 May, 2010.

Focussing on the surface observations (Figure 4.21), the precipitation less than 0.4 mm hr^{-1} starts at from 0:02 UTC, and continues to 11:00 UTC, with break at 3:00, 5:00 and 10:00 UTC. The wind consistently blows from the southwest (200 - 270 degree) from 0 to 10 UTC, with wind speeds between 5 and 10 m s^{-1} , while the sea surface pressure rise from 1020 to 1022 hPa. The 2m temperature

increases from less than 4.5 °C at 1:00 UTC to more than 5 degrees at 8 UTC, and then dropped to below 5 °C (Figure 4.21d). Discontinuous precipitation occurs from 1 UTC to 11 UTC with maximum of 0.4 mm hr⁻¹.

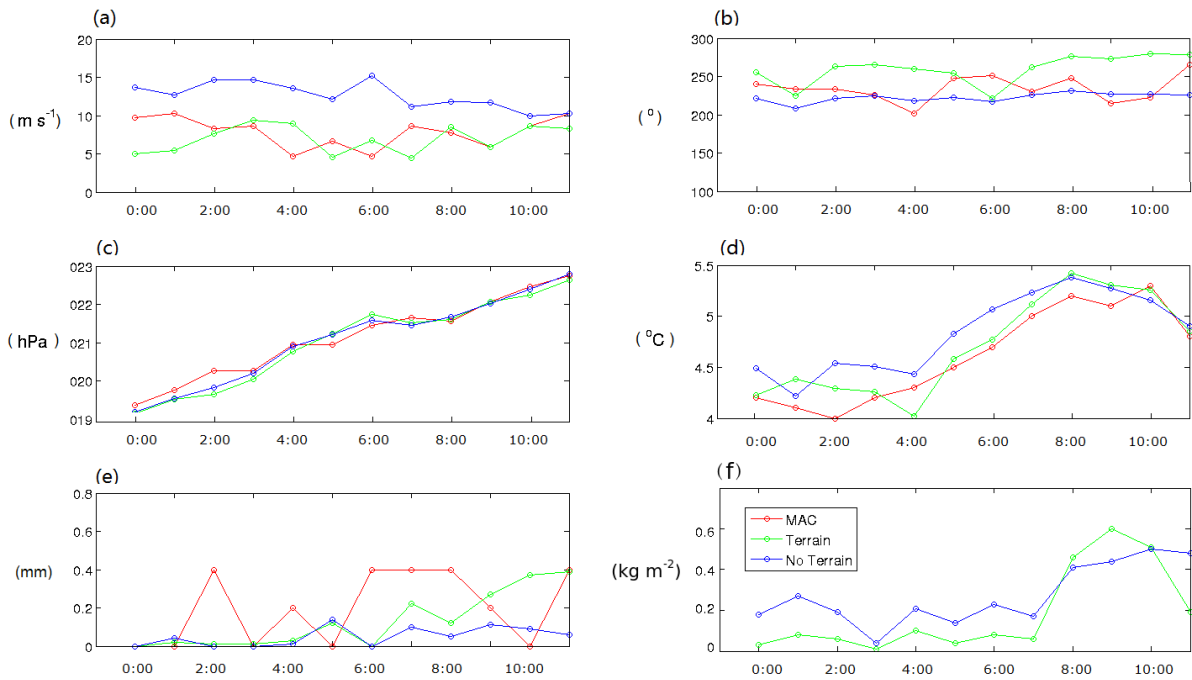


Figure 4.21 (a) Wind speed, (b) wind direction, (c) pressure, (d) temperature, (e) precipitation and (f) liquid water path from surface weather records (MAC), and 100 m resolution WRF simulations with terrain and without terrain in a drizzle case on 30 March, 2009.

Comparing the WRF simulations with MAC, temperature and moisture are simulated well in the boundary layer, but the moisture is underestimated between 3 and 5 km (Figure 4.20). The timing of precipitation is well simulated by WRF, but the intensity is underestimated (Figure 4.21e). The 2 m temperature (Figure 4.21d) is slightly overestimated for both simulations. The sea surface pressure (Figure 4.21c) is well simulated. The wind speed from the simulation

with the terrain is comparable with that from surface records (Figure 4.21a), while the wind direction is not accurately simulated (Figure 4.21b).

As before, the orographic effect is isolated by running two sets of simulations, with and without terrain. There is no significant difference between the simulated precipitation with and without terrain before 6:00 UTC, 30 March, 2009, while the precipitation from the simulation with terrain is remarkably higher than that without terrain after 7:00 UTC. The wind speed from the simulation without terrain is about twice of that with terrain, which suggests the orographic effects are strong because the main obstacle is on the upwind side of the island. The wind is from west in the simulation with terrain, while it is from southwest in the simulation without terrain. The difference between the simulated sea surface pressure with and without terrain is negligible. The liquid water path shows that clouds are blocked by the terrain from 0 UTC to 7 UTC, when the station is on the downwind end of the island. At 9 UTC, the liquid water path is enhanced by terrain, which may result from the clouds and precipitation over the top of the island are transported over the station.

Near the surface site, the precipitation is enhanced on the lee of the island in 100 resolution domains (Figure 4.22). This enhancement can also be seen in 1 km resolution domains (Figure 4.23).

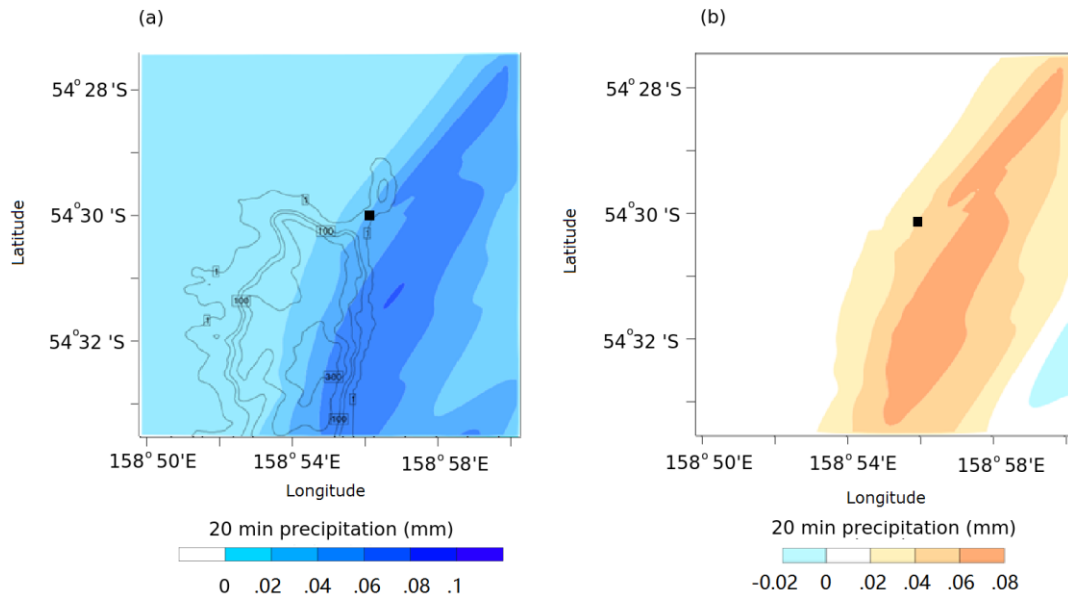


Figure 4.22. (a) 20 min precipitation from WRF simulations in 100 m resolution with terrain and (b) the difference in the precipitation with and without terrain in a drizzle case at 08:00 UTC, 30 May, 2009. The location of the ABoM station is shown by the black square.

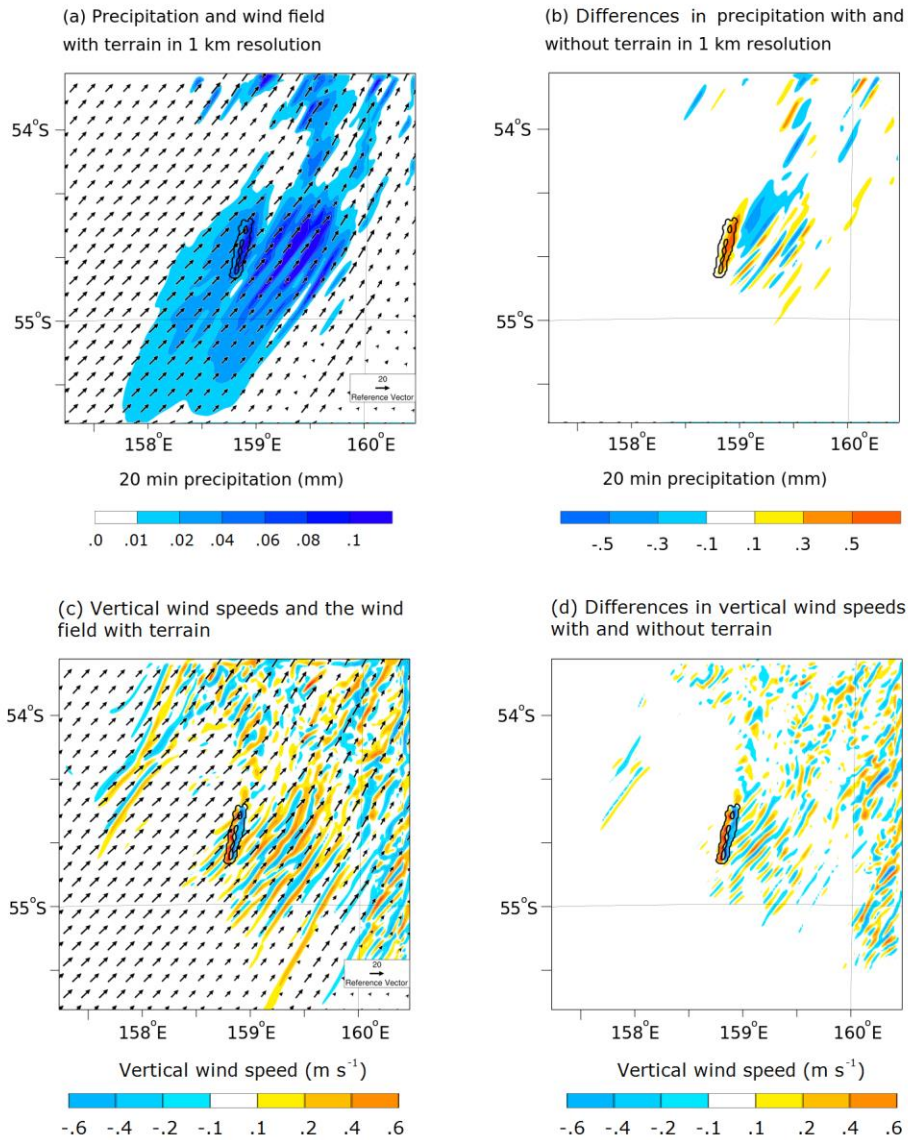


Figure 4.23. (a) 20 min precipitation from WRF products with terrain, (b) the difference in the precipitation with and without terrain in a drizzle case at 8:00 UTC, 30 May, 2009, (c) the wind field on 500 m height from WRF products with terrain, (d) the difference in the vertical wind with and without terrain.

The distribution of precipitation and vertical movement forms wave like pattern to the east of Macquarie Island (Figure 4.23). Corresponding pattern in cloud field is observed by MODIS (Figure 4.24) 8 hours earlier. This is a horizontal roll vortice or “cloud street” phenomenon, which is commonly observed in the PBL

over the SO (LeMone 1973). The depth of a vortex is usually on the order of 1–2 km which is generally the depth of the boundary layer, and a vortex pair usually has a lateral to vertical dimension ratio varies between 2:1 and 6:1 (Brown 1980). When the cold air advects from the southwest over warmer sea surface (Figure 4.25), the air near the sea surface is warmed and rises. This shallow convection can cause the formation of clouds, which are found at about 1 km above the sea surface in the cross-section of liquid water mixing ratio at 23 UTC 29 May, 2009 (Figure 4.26).

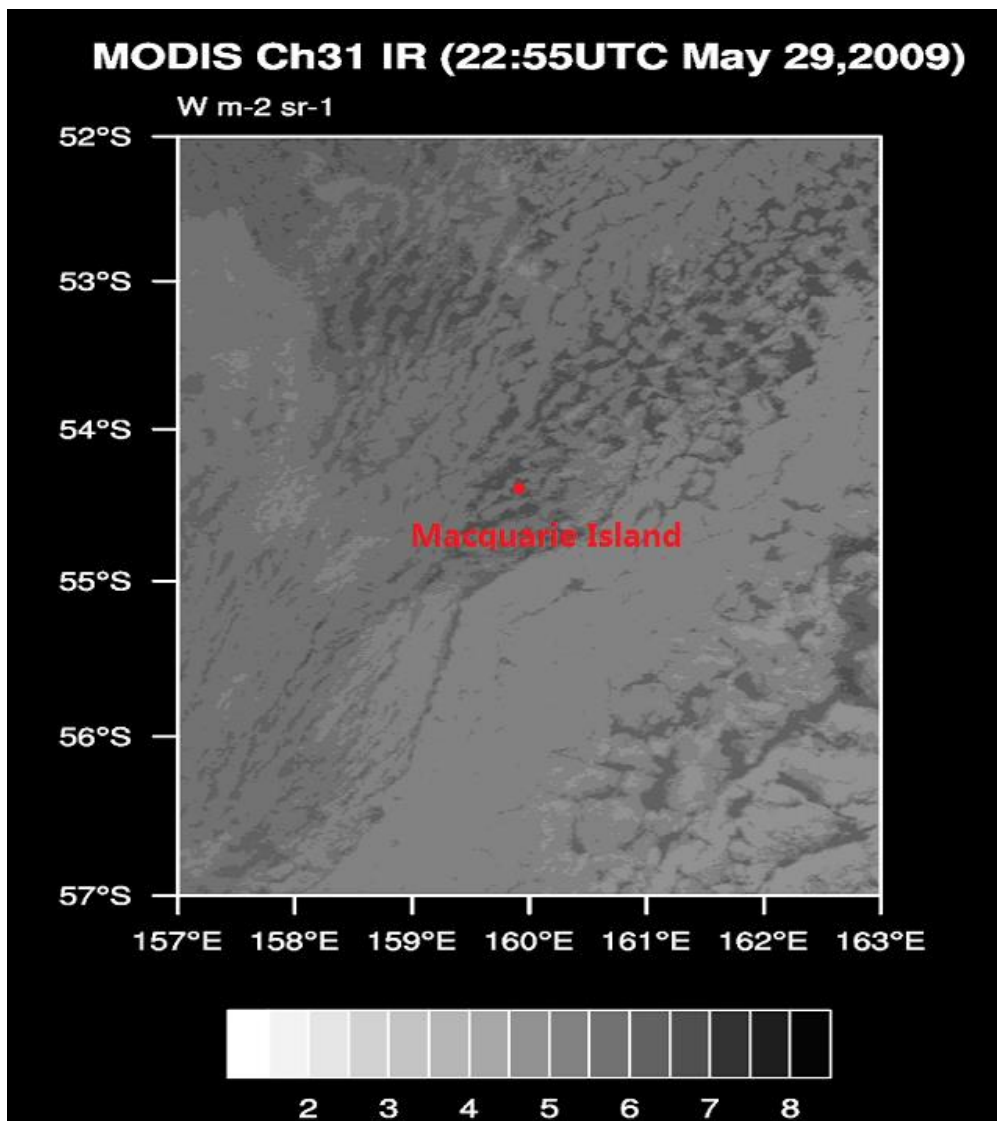


Figure 4.24. MODIS IR at 22:55 UTC 29 May, 2009

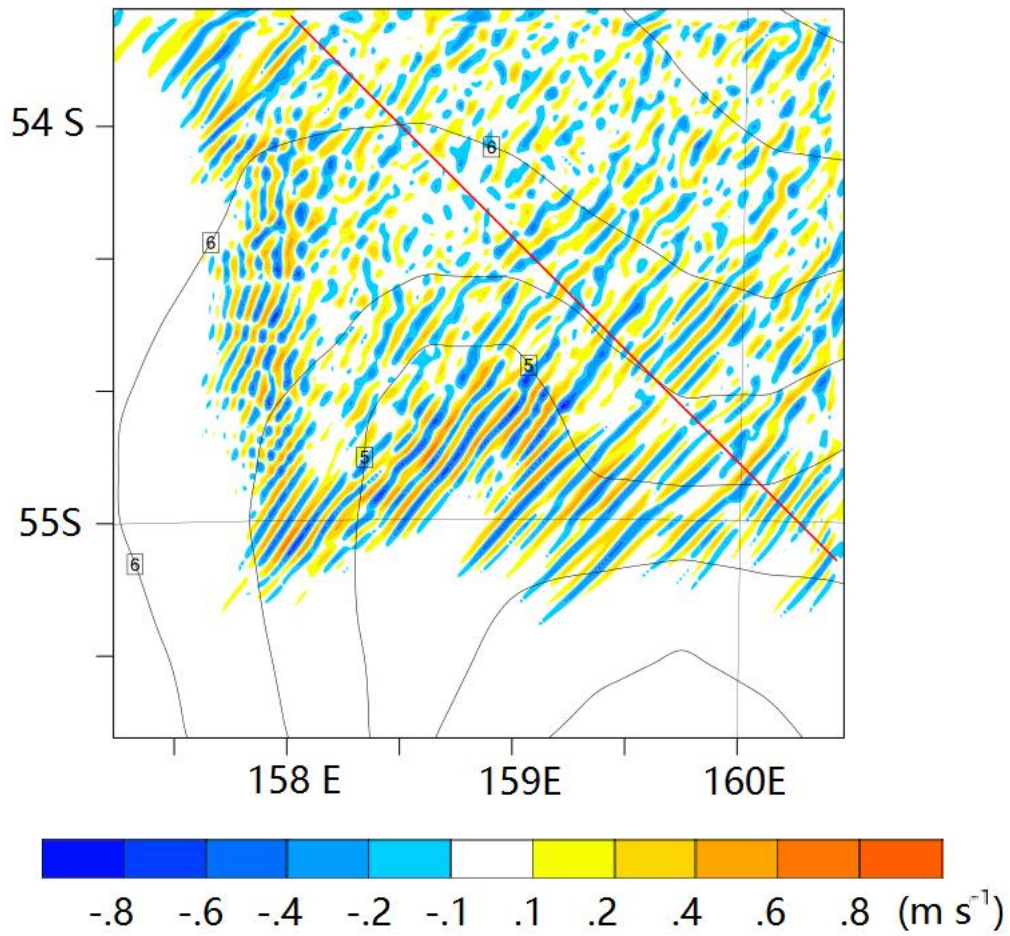


Figure 4.25. The vertical wind speed on 200m and sea surface temperature from the 3 km WRF resolution simulation at 23 UTC 29 May, 2009. The red line represents the location of cross-section in Figure 4.26.

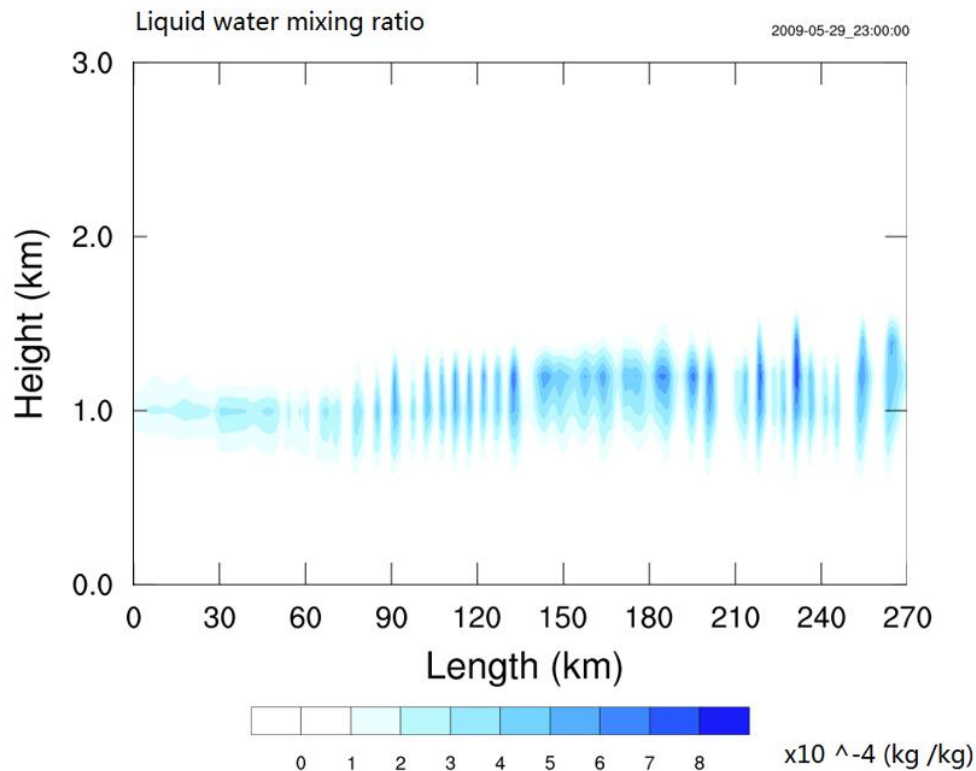


Figure 4.26. The cross-section of liquid water mixing ratio from the 3 km WRF resolution simulation at 23 UTC 29 May, 2009.

Looking up through the atmospheric column above MAC we find that, from surface to 100m height, the wind speeds from the WRF simulation with terrain are less than those from the WRF simulation without terrain, while the wind speeds from the WRF simulation without terrain are higher from 100 m to 400 m (Figure 4.27 a). The wind speeds from MAC sounding records are lower than the simulation results below 200m, and higher than them above 200m. ERA-I underestimates the wind speeds below 500 m. The wind directions are changed from 230 to 260 degree by the orography (Figure 4.27 b), from the southwest to west.

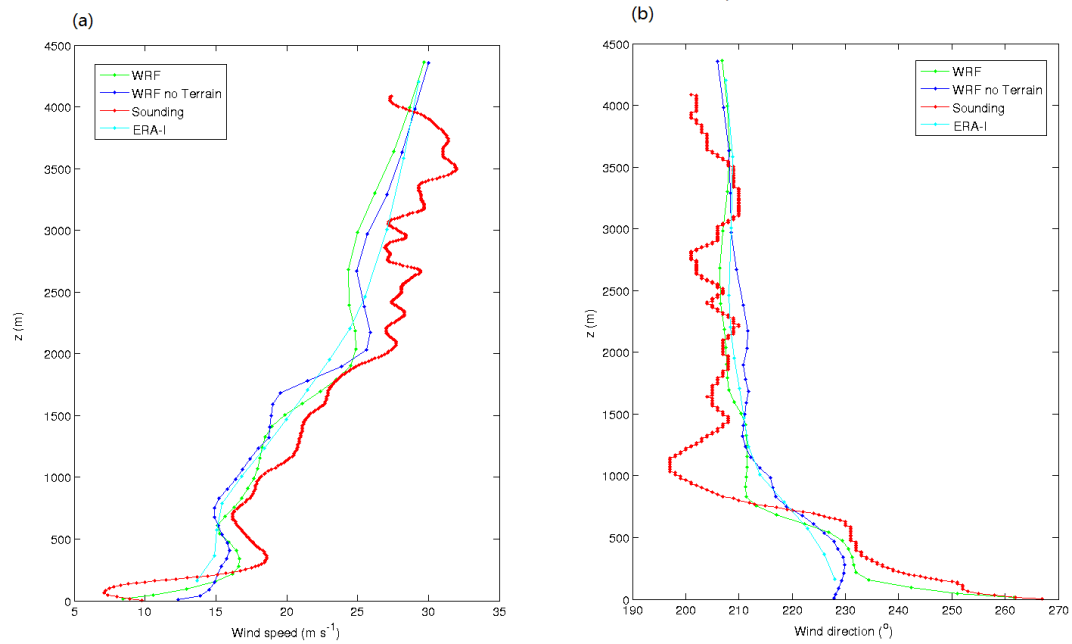


Figure 4.27. (a) Wind speed and (b) wind direction from 100 m domain WRF simulations, MAC sounding and ERA-I over the station at 12:00 UTC, 30 May, 2009.

In summary, the simulation of the southwest drizzle is accurate in time but not accurate in magnitude. Very shallow roll clouds were observed in the MODIS imagery most likely arising from the advection of cold southerly air over warmer sea surface temperatures. The high-resolution WRF simulations have some skill in capturing these dynamics. The Froude number (3-D) from the simulation is as large as 4.76, but winds from the southwest still turn approximately 40 degrees on 10 m height near the station. The orographic effect on the precipitation observed at MAC station is not negligible.

4.4.4. A cyclone case

While the frontal precipitation associated with cyclone activities dominates the

precipitation over the SO, the accumulation of the precipitation caused by cyclones passing directly overhead MAC is not as significant as that along the fronts (Figure 3.2b), so a coarser resolution (1 km) is used in this case. A cyclone passed over Macquarie Island from west on 6 May, 2009 (Figure 4.28). The sea level pressure in the core of the cyclone is 980 hPa. The air is saturated and stable in the boundary layer below 3km. The wind direction turns from south to west, from surface to 2 km (Figure 4.29).

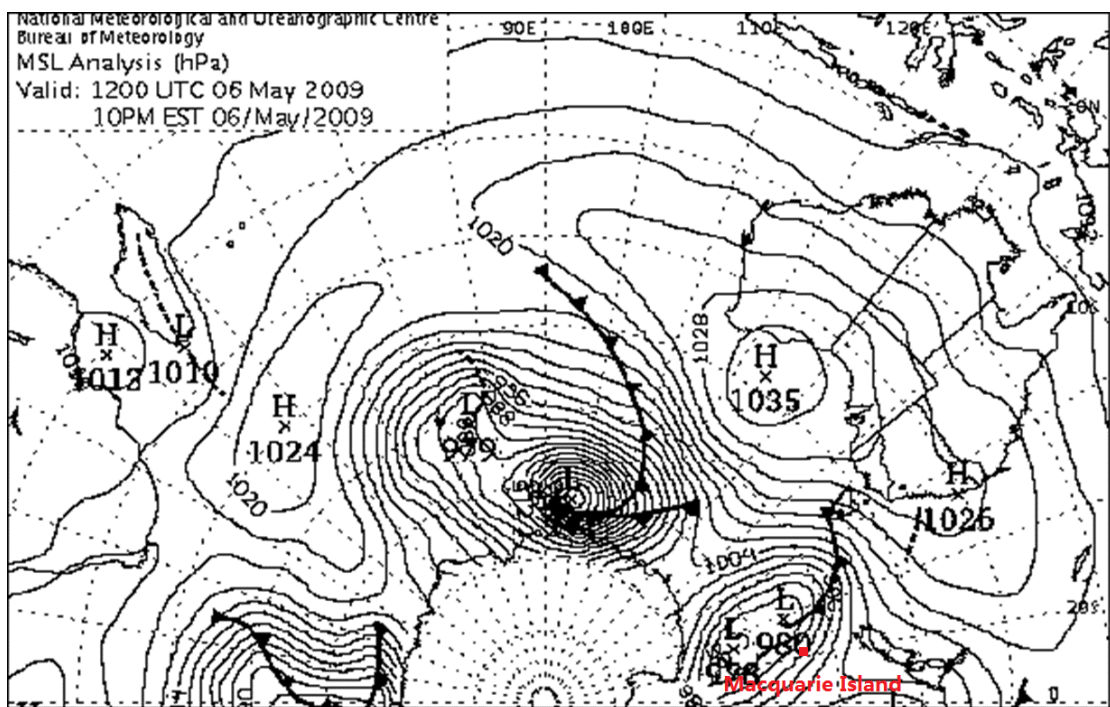


Figure 4.28 The ABoM Mean Sea Level Pressure (MSLP) chart showing a cyclone passing Macquarie Island (the red point) at 12:00 UTC 6 May, 2009.

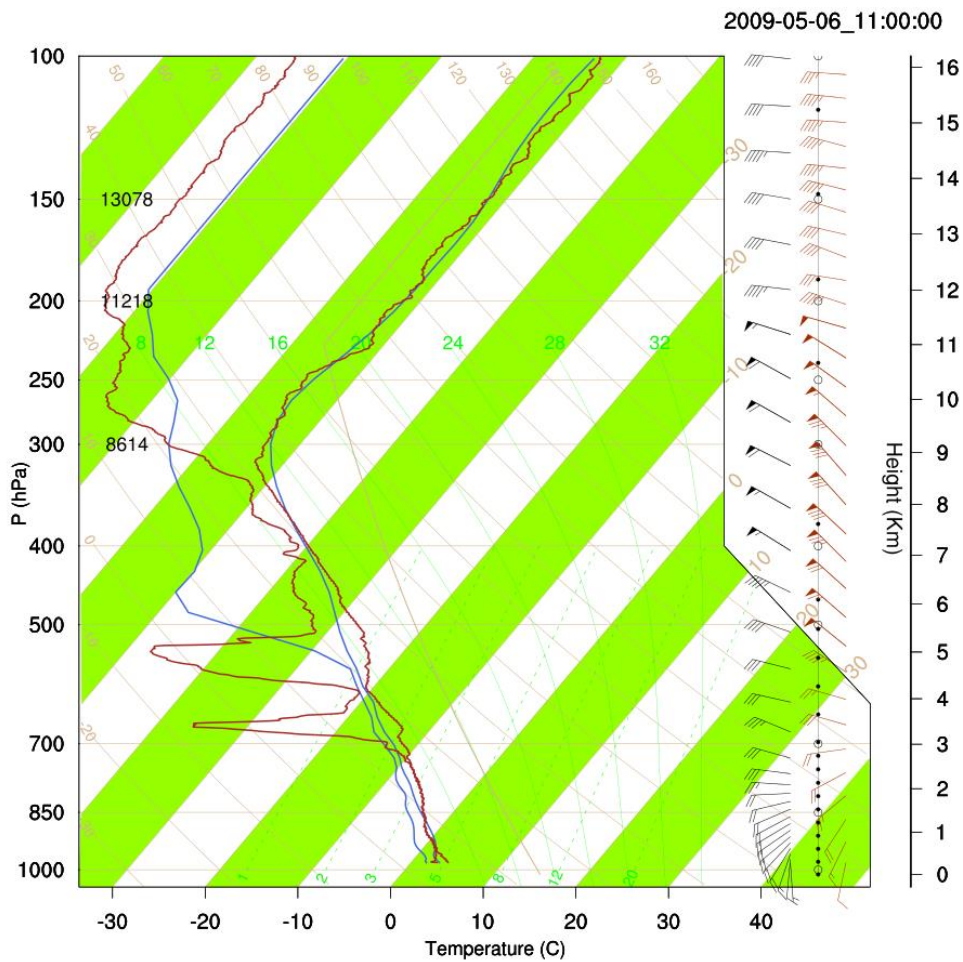


Figure 4.29 The Skew-T chart from the sounding (brown) and 1 km resolution WRF simulation with the terrain (blue) for the cyclonic case at 11:00 UTC 6 May, 2009.

This cyclone can be studied in two parts: the warm air mass and the cold air mass around the lowest pressure which arrives MAC station at 10 UTC (Figure 4.30c). The warm air mass reaches Macquarie Island first, then the cold air mass reaches the island after 10 UTC, consequently. The wind speed changes from approximately 10 m s^{-1} in the warm air mass to less than 5 m s^{-1} in the cold air mass, with wind direction changes from northwest to south. The temperature

drops more than 4 degrees from 9 UTC to 12 UTC. Most of the precipitation observed in the warm air mass before 10 UTC. The liquid water path shows more clouds in the cold air mass.

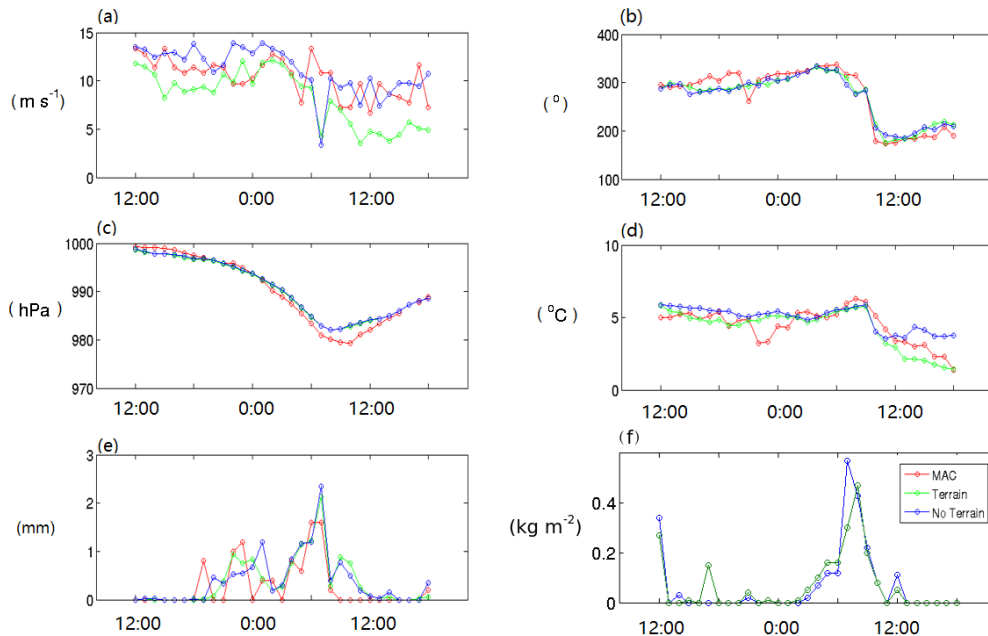


Figure 4.30. (a) Wind speed, (b) wind direction, (c) pressure, (d) temperature, (e) precipitation and (f) liquid water path from surface weather records (MAC), and 1km resolution WRF simulations with terrain and without terrain in a cyclone case from 12:00 UTC 5 May, 2009 to 18:00 UTC 6 May, 2009.

The simulation matches the sounding well below 3 km, with slight underestimate of the moisture (Figure 4.29). Above that, the moisture is not simulated well between 3 and 9 km. At the surface station (Figure 4.30), the precipitation in this case is well simulated, although the peak intensity is slightly overestimated at 7:00 UTC. The wind speed in WRF is largely consistent with MAC in the warm air mass, while underestimated in the cold air mass. The wind direction, temperature and pressure are all accurately simulated.

The terrain effect on the station are negligible on the precipitation (Figure 4.30e). The wind speed is reduced 2 m s^{-1} in the warm air mass and 5 m s^{-1} in the cold air mass, due to the orographic effects. The wind speed from the simulation with terrain is less than that from MAC in the cold air mass, suggesting that the orographic effects are overestimated.

Moving away from the surface site, the precipitation in the warm air mass is found enhanced in the lee, with a strong west wind (Figure 4.31). By contrast, the precipitation is enhanced in the windward side in the cold air mass, with a weak southerly wind (Figure 4.32).

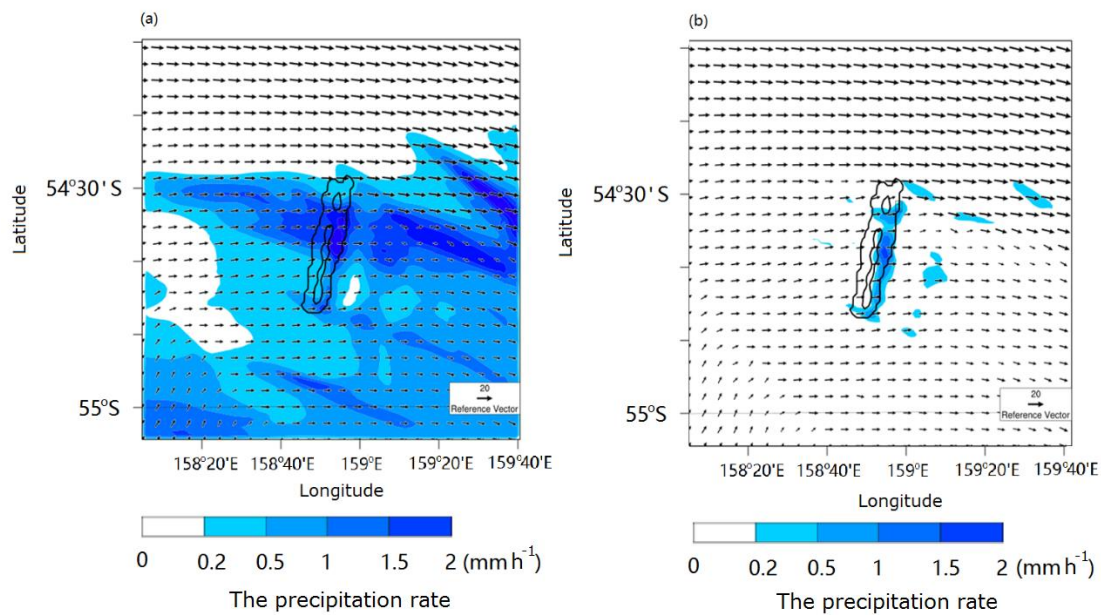


Figure 4.31. Precipitation and wind fields from WRF simulations with and without terrain at 8:00 UTC, 6 May, 2009. (a) The 30 min surface accumulated precipitation and the wind field from the 1 km domain at 300 m above ground. (b) The differences between the precipitation in the simulations with and without terrain for the same domain.

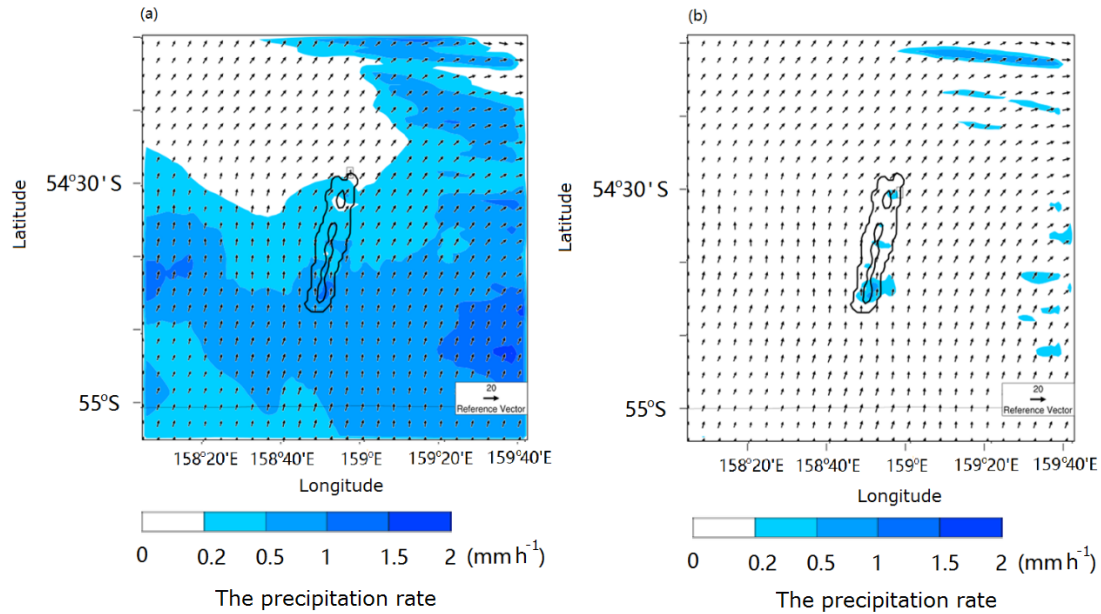


Figure 4.32. Precipitation and wind fields from WRF simulations with and without terrain at 11:00 UTC, 6 May, 2009. (a) The 30 min surface accumulated precipitation and the wind field from the 1 km domain at 300 m above ground. (b) The differences between the precipitation in the simulations with and without terrain for the same domain.

The precipitation in this case is well simulated, although the peak intensity is slightly overestimated at 9:00 UTC. The orographic effect on the precipitation is neglectable at MAC station. The wind speed is reduced 2 to 5 m s⁻¹ due to the orographic effects. The Froude number (3-D) from the simulation reduce from 4.44 in the warm air mass to in the 2.24 cold air mass. In both bands with different wind speeds and directions, precipitation over the station is almost not affected by the terrain.

4.5. Summary

In order to study the orographic forcing of Macquarie Island on the records of its

weather station, four representative case studies (a cold front, a warm front, drizzle and a mid-latitude cyclone) have been simulated using high-resolution numerical simulations both with and without terrain. Overall the simulations suggest that the orographic forcing on the precipitation record is negligible except for weak drizzle arriving with southwesterly winds. The station is well-positioned to be exposed to the most frequent precipitation events arriving from the north and west (e.g. the cold front case). The precipitation at the station can be perturbed when the air mass arrives from the south and southwest (e.g. the drizzle case), although this is commonly associated with weak precipitation during cold air advection.

Similarly, the orographic forcing on the surface winds observed at the station is also weak. The most negligible orographic forcing at the station occurs when the winds are from the northwest. For the cases simulated, the wind speed differences are less than 5 m s^{-1} if the winds are from the west or northwest, but can be larger for southerly and southwesterly winds. The wind direction differences are less than 20° for the northerly and westerly winds, but higher for the southerly winds. The orographic effects on the pressure and temperature are also negligible.

We conclude that the Macquarie Island weather station is well positioned for the observation of the marine meteorology, because the orographic effects are minimal not only for the winds, but also for the precipitation. The station is clearly exposed for the predominant strong northwesterly winds, and in the lee only for the southerly and southwesterly winds, which are rarely associated with strong frontal precipitation.

Away from the station, the island represents a potential obstacle to the boundary layer winds. Analysis of the fluid dynamics show that the terrain can cause vertical motion that enhances the clouds aloft when the $Fr > 1$, and the main enhancement on the precipitation is normally transferred to the leeward. Flow field blocking is also possible with $Fr < 1$, with weak northerly and southerly winds (not shown).

The gravity waves on the downwind side caused by the island could propagate from surface to tropopause, extending more than 50 km downwind if the wind direction does not change (Figure 4.7g). For the study using UASs to investigate the dynamical processes and aerosol/cloud interactions around Macquarie Island in the future, the flow field distortion must be appreciated. The terrain may also affect the measurements on the upwind side when the wind is weak, by creating a high-pressure zone (less than 10 km from the island) in front of the island and enhancing the clouds and precipitation by lifting the air (Figure 4.16). These simulations can provide guidance for choosing where to operate UASs around the island; generally speaking, operations should be held 10 km upwind of the island or to the north if the flow is from the west.

The high-resolution WRF simulation has some skills in capturing the dynamics of low level clouds and weak convection in the non-frontal drizzle case, but underestimates the magnitude of the precipitation. Furthermore, the post-frontal low level clouds are missing in the cold front case, with an underestimation of the moisture flux from the sea surface. The limitation of the model need to be improved in the future studies with a further understanding of the microphysics of low level clouds and drizzle.

5. An analysis of the Froude number over Macquarie Island

The high-resolution simulations from Chapter 4 were of four “typical” synoptic patterns associated with precipitation at the station on Macquarie Island. In all four cases, the Froude number was larger than 1 and the air flow was not significantly blocked by the island. The atmosphere largely passed over the mountain rather than around it. In this chapter a climatology of the Froude number of Macquarie Island is developed to further explore how representative these case studies were. The historic sounding archive from Macquarie Island is employed to develop this climatology.

5.1 Definitions of 2-D and 3-D Froude number

The effect of orography on meteorology has commonly been expressed through the Froude number ($Fr = U/NH$), where U (m s^{-1}) is the cross mountain wind speed, N (s^{-1}) is the Brunt–Väisälä frequency and H (m) is the mountain height, which is the ratio of the inertial force to the gravitation force (e.g. Smolarkiewicz and Rotunno, 1989) or its inverse, a nondimensional mountain height (Smith 1989). The *moist-N* was calculated with the expression in Kirshbaum and Durran (2004):

$$N_m^2 = \frac{g}{T} \left(\frac{dT}{dz} + \Gamma \right) \left(1 + \frac{Lq_s}{RT} \right) - \frac{g}{1 + q_w} \frac{dq_w}{dz}$$

where T is the temperature, R is the ideal gas constants for dry air, L is the latent heat of condensation of water, q_s is the saturation mixing ratio, q_w is the total water mixing ratio, and Γ is the moist adiabatic lapse rate.

The Froude number (Fr) has been used for defining whether an air flow passes over or around a mountain/obstacle. When $Fr > 1$, the current is forced over the mountain, as a result, gravity waves and lee waves are common. When the $Fr < 1$, the magnitude of any gravity wave is drastically reduced and the flow is primarily disturbed horizontally rather than vertically, in which case horizontal vortex streets can occur on the lee of the mountain (Schär and Durran, 1997). The mountain horizontal aspect ratio ($\gamma=a/b$, a and b are, respectively, the half-widths of the mountain in the x and y directions) is another key parameter that represents the effects of the mountain shape on the flow field. Smith (1989) revealed the cooperative effects of the Froude number and the horizontal aspect ratio and distinguished two kinds of curves for large and small horizontal aspect ratios.

The mean N_m and mean wind speed from 50 to 400 m over the MAC site location in no-terrain simulations were used to calculate the Froude number. Theoretically, the Froude number is calculated in a 2-D framework using the cross-mountain wind speed (Miglietta and Buzzi 2001; Colle 2004), which is in our case the wind component perpendicular to the island ridge (279 degree). While such a perspective may be appropriate for the orographic forcing about the island as a whole, it is of limited meaning for a station located on the far northern tip of the island. For a single peak island or complex terrain with small horizontal aspect ratio (Smolarkiewicz et al. 1988), 3-D Froude number is calculated using mean wind speeds instead of the cross-mountain wind speeds. In our cases, the 2-D Froude number is used to see the terrain effects around the

whole island. We also consider the 3-D Froude number, which is used to estimate the terrain effects of the 250 m hill to the southwest of the station.

5.2 The Froude number of the four case studies

The Froude number has been calculated for the four cases in their highest resolution, which preserve the most orographic information. For all the cases in this study (a cold front, a warm front, a drizzle and a cyclone case), the 3-D Froude number is larger than 1 (Table 5.1). The Froude number from WRF matches that from MAC, except for only one value in the warm air mass of the cyclone case. This Froude number is 4.44 from the simulation, and is larger than the result from MAC (2.99). The overestimation of the mean wind speed accounts for this error.

The Brunt–Väisälä frequency ranges between 0.0128 and 0.0196 (s^{-1}), while the mean wind speed varies in a wider range between 8.2 and 24.8 ($m s^{-1}$), as a result, the wind speed dominates the value of the Froude number. During the passage of the cold front on 09 Oct 2008, the 3-D Froude number from MAC decrease from 5.29 to 4.54, with the wind speed changes from 24.8 to 22.5 ($m s^{-1}$). For the warm front case, the Froude number increases from 2.23 to 4.64, with the wind speed increases from 9.5 to 18.3 ($m s^{-1}$). Froude number changes little over the time of the passage of the high pressure system. Finally, in the cyclone case the Froude number decreases from 2.99 in the warm air mass to 2.26 in the cold air mass, with the wind speed decreases from 11.1 to 8.2 ($m s^{-1}$).

| Case | Section | Time(UTC) | Wind direction on 500m | Data source | Mean Wind speed (m s^{-1}) | Mean N (s^{-1}) | Fr (3-D) |
|------------|--------------------|---------------------|------------------------|-------------|---------------------------------------|----------------------------|----------|
| Cold front | Pre-front | 12:00 09/10/2008 | NW | MAC | 24.8 | 0.0187 | 5.29 |
| | | | | WRF | 22.5 | 0.0171 | 5.26 |
| | Post-front | 23:00 09/10/2008 | W | MAC | 21.9 | 0.0193 | 4.54 |
| | | | | WRF | 22.3 | 0.0183 | 4.86 |
| Warm front | Pre-front | 23:00 14/03/2010 | N | MAC | 9.5 | 0.0171 | 2.23 |
| | | | | WRF | 9.3 | 0.0196 | 1.90 |
| | Post-front | 11:00 15/03/2010 | W | MAC | 18.3 | 0.0158 | 4.64 |
| | | | | WRF | 13.4 | 0.0164 | 3.28 |
| Drizzle | | 12:00 30/05/2009 | SW | MAC | 14.6 | 0.0157 | 3.80 |
| | | | | WRF | 14.8 | 0.0128 | 4.76 |
| Cyclone | Warm air mass | 00:00 06/05/2009 | NW | MAC | 11.1 | 0.0148 | 2.99 |
| | | | | WRF | 18.3 | 0.0165 | 4.44 |
| | Cold warm air mass | 12:00 06/05/2009 | S | MAC | 8.2 | 0.0145 | 2.26 |
| | | | | WRF | 9.2 | 0.0164 | 2.24 |

Table 5.1. Froude numbers in the cold front, warm front, drizzle and cyclone case study, calculated from MAC and WRF.

5.3 A climatology of the Froude number

A climatology of the 2-D and 3-D Froude numbers has been produced from the MAC soundings from 2003 to 2010 (Figure 5.1a). 93.5% of the 3-D Froude numbers are larger than 1, which suggests that in the majority of cases the 250 m ridge near the station does not strongly block the flow, and motion across the ridge, rather than around it, is common. For the 2-D analysis, there are accordingly more cases (5.6%) with the Froude numbers less than 1 as the cross-mountain wind U is reduced. This suggests that the upstream blocking is

relatively more common upwind of the main ridge of the island away from the station.

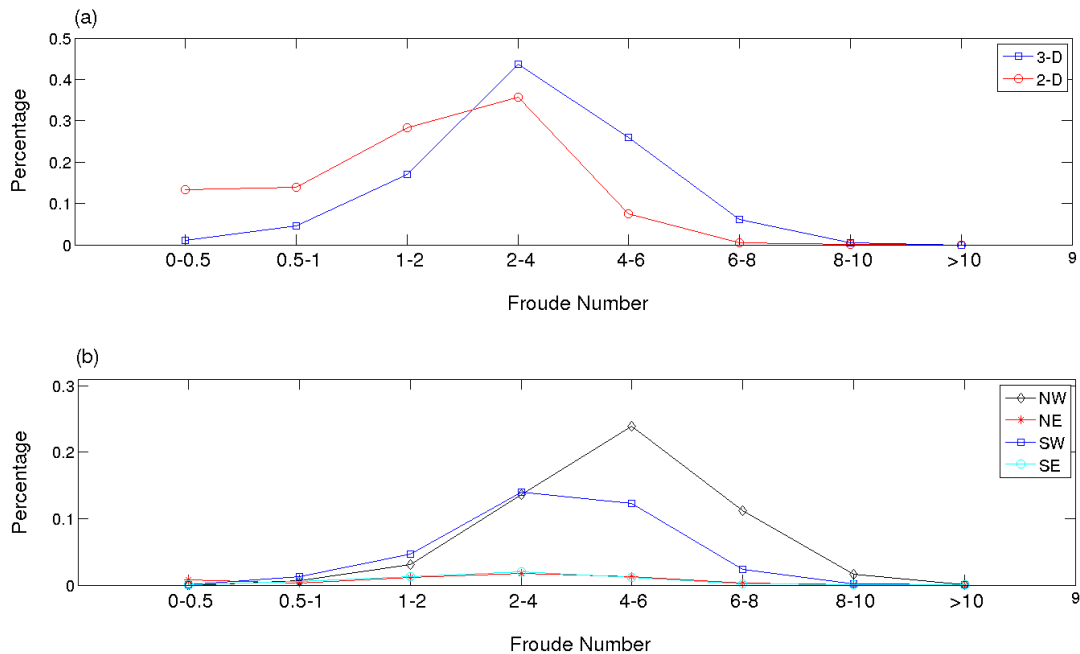


Figure 5.1. (a) The Probability Density Function (PDF) of the Froude number from the MAC soundings. (b) The PDF of the 3-D Froude number in four wind directions on 850 hPa from the MAC soundings. NW represents winds between 270 and 360 degree, and the rest may be deduced by analogy.

The observations at the weather station can be affected by the orography in cases when $Fr < 1$ and winds are northwesterly, or cases when $Fr > 1$ and winds are southwesterly. The former is very rare (1.4%) (Figure 5.1b), while the latter is relatively common (33.6%), but normally associated with drizzle or no precipitation. Orographic effects on the precipitation records of the station in other cases are nearly negligible. For example, most frontal precipitation at MAC has been found associated with northwesterly winds and $Fr > 1$, as shown in the

cold and warm front cases in Chapter 4 (53.5%), which leads to minimal orographic effects on the precipitation observation at the station.

Our understanding of the orographic effects over Macquarie Island is limited by sparse observations and a generalization of the dominant meteorology. Certainly extraordinary precipitation events do arise, as detailed in Wang et al. (2015). To further generalize the orographic effect on the precipitation records at MAC station, the 3-h surface records from MAC (and ERA-I) are presented (Figure 5.2). (Note that a full precipitation rose is presented in Figure 2.5). For the MAC records with northwesterly wind, no precipitation is observed 40% of the total time from 2003 to 2011, while precipitation is observed in 24% of the time. No significant orographic effect is expected on the surface precipitation at the station during this 64% of time. For the southwesterly wind sector, no precipitation is observed in 16% of the time, while precipitation is observed in 10% of the time. During these times orographic effects may be present at the station. Northeasterly and southeasterly winds are rare. For ERA-I, which does not include the terrain, southwesterly winds are more common, occurring 35% of the time. As discussed in Chapter 2, this suggests that a portion of the southwesterly surface winds is forced around the ridge located to the southwest of the station.

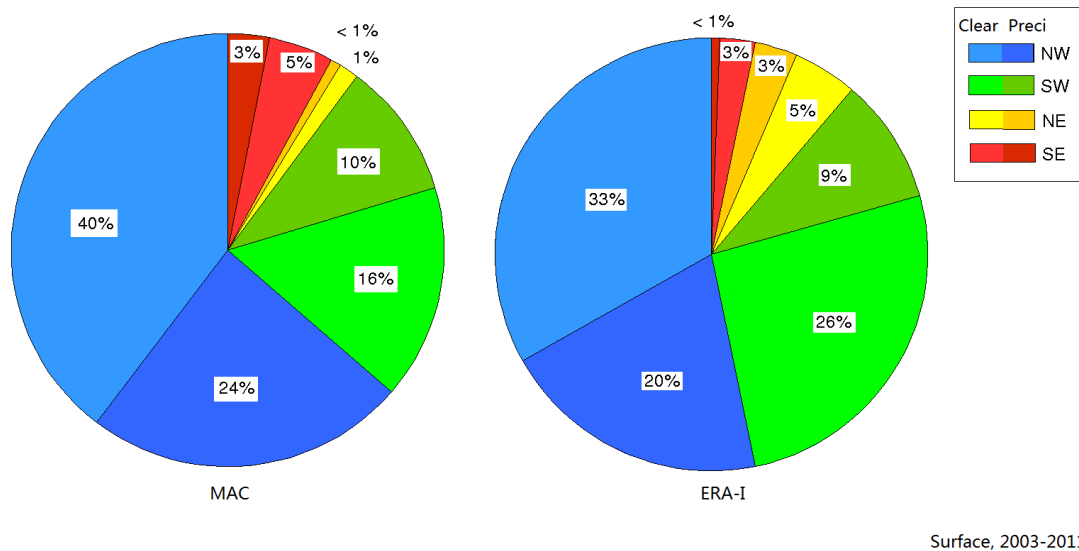


Figure 5.2. Pie chart diagram showing the frequency of winds from different sectors with and without precipitation (from 2003 to 2011), from (a) MAC and (b) ERA-I. NW represents winds between 270 and 360 degree, and the rest may be deduced by analogy.

5.4 Summary

A climatology of the Froude number over Macquarie Island has been constructed using the MAC soundings from 2003-2010. Looking first at the 3-D Froude numbers, approximately 93.5% of the soundings have Froude number larger than one, suggesting that upstream blocking is not a primary concern, and much of the boundary layer flow passes over the island.

When broken into sectors, the 3-D Froude number is particularly large when the flow arrives from northwest, which is most frequent. Given that the station is cleanly exposed to the wind when they are from the northwest, little orographic effect is anticipated during these times. This is consistent with the numerical simulations of the cold and warm front case studies (Chapter 4.) When the wind

is from the southwest, it is still common for the 3-D Froude number to be larger than one, suggesting that leeside convergence is possible and precipitation may be enhanced at the station. This is consistent with the numerical simulations for the drizzle case study. Seeing as drizzle is common for post-frontal flow from the southwest (Chapter 3), this orographic enhancement contributes only weakly to the annual precipitation. A crude calculation suggests that does not account for the difference between ERA-I and the MAC annual precipitation records (Chapter 2.)

Turning our attention from the station alone to the island as a whole, a climatology of the 2-D Froude number has also been produced. As only the normal wind component is used in this calculation, the 2-D Froude number will always be greater than or equal to the 3-D Froude number. This difference, however, is not substantial, as westerly winds are most common at Macquarie Island (Chapter 2). For the 2-D Froude number, 94.4% of the soundings are still larger than one, suggesting the boundary layer air passes over the island and convergence is observed in the lee of the island. Approximately 5.6% of the soundings have the 2-D Froude number less than 1, suggesting that upwind blocking is prevalent.

6. Conclusions

6.1. A climatology of the precipitation over the Southern Ocean

Precipitation over the Southern Ocean is a critical component of the Earth's water and energy cycle. Thus, understanding its characteristics and mechanisms is a vital step towards improving climate modeling and predictions. Given that spaceborne sensors remain the only tool for wide-spread observations over this remote region, there is a pressing need for a better validation and characterization of satellite retrieval products. This is particularly true when a new standard of spaceborne precipitation measurement is made through the integration of next-generation products (e.g. Global Precipitation Measurement). A surface station on Macquarie Island (54.50°S 158.94°E) in the midst of the SO, with observation records since 1948, has increasing value in recent years in helping develop an understanding of the meteorology over the SO. For example, Adams (2009) reported a 35% increase in surface precipitation from 1971-2008 based on the observations. In this research, a climatology of the precipitation (frequency and intensity) over the Southern Ocean was built with the records in Macquarie Island. The ground-based measurements were compared with the precipitation products from CloudSat products and ERA-I to evaluate their performance.

The annual cycle of the MAC precipitation records from 1979 to 2011 displays a peak in March, but the variability of precipitation is relatively moderate for the

rest of the year. ERA-I also records a peak in March, but the variability is much greater throughout the year. The average annual precipitation from 1979 to 2011 is 1023 mm per year for MAC, and 953 mm per year for ERA-I, which is underestimated by approximately 6.8 %.

The frequency of occurrence for the 3-h MAC precipitation record from 2003 to 2011 is 36.4%. The frequency of the light precipitation ($0.066 \leq P < 0.5 \text{ mm hr}^{-1}$) in MAC is 29.7%, while the frequency of the heavy precipitation ($P \geq 1.5 \text{ mm hr}^{-1}$) is 1.1%. For ERA-I, the frequency of the precipitation is lower (31.9%), with less light precipitation is 27.6%, and the heavy precipitation is 0.3%. However, ERA-I produces a considerable amount (43.9%) of drizzle. This drizzle is below the detectable threshold of MAC.

The frequency for the CPR (the Cloud Profiling Radar; Stephens et al. 2002) PC (2C-COLUMN-PRECIP; Haynes et al. 2009) rain is 30.5%. The mean rain rate of 'certain' radar columns is 1.24 mm h^{-1} . This value is larger than the segment mean rain rate because it excludes the clear radar columns in rain segments, which are common. A precipitation rate is not available in CloudSat products when the precipitation is deemed to be either mixed-phase or glaciated. CPR products in 176 segments that passed over Macquarie Island from 2007 to 2010 were analyzed, including only warm rain, which may have led to a seasonal bias in the results. The mean rain rates of 'probable' and 'possible' radar columns are 0.28 and 0.13 mm h^{-1} , respectively.

MAC and CloudSat products match up each other approximately 90% of agreement in precipitation occurrence detection, at 1-h and $\sim 0.5^\circ$ resolution.

The PC product shows greater skill for light precipitation than the RP product primarily because it has a higher frequency as the algorithm includes 'probable' precipitation radar columns, whereas the RP product only includes 'certain'.

Heavy precipitation is more commonly associated with fronts (80%) than otherwise. It was further noted results obtained from the analysis of different definitions of fronts were commonly inconsistent over the Southern Ocean, especially for weaker events. Also a non-trivial fraction of the heavy precipitation is not closely associated with frontal systems.

Two cases studies have been examined to explore the relation between the heavy precipitation and the synoptic meteorology. For both cases, heavy precipitation is found in the various observation and model records (MAC, CloudSat, ERA-I), but a frontal passage or a cyclonic low is not identified in either case. This highlights the difficulties in accurate identification of fronts over the Southern Ocean. Also, a type of heavy precipitation was found on the outskirts of the high systems, which transported the moisture from the warmer waters far to the north.

Ekman spirals, which have been reported in the PBL over the SO, have also been found over Macquarie Island (Hande et al. 2012b). These spirals are approximately 400 meters deep. The local orography, however, does effect the observation of the spiral, especially through the lowest 200 m above the surface, where a ridge to the southeast of the station can divert the heading of the low-level winds. The boundary layer flow from a southerly or southwesterly heading can be split by the island, and forced to turn clockwise or anti-clockwise. The

former amplifies the Ekman turning, while the latter offsets the Ekman spiral effects.

6.2. WRF simulations on the orographic effects of Macquarie Island

Given the discrepancies between the ERA-I and the MAC precipitation records, it is necessary to consider whether the MAC records are subject to orographic enhancement. The orographic effects on the meteorology records at Macquarie Island weather station have been studied, using high-resolution numerical simulations (WRF) for four cases (a cold front, a warm front, drizzle and a mid-latitude cyclone). In order to isolate the orographic effects, each case has been simulated twice, with and without terrain. This preliminary study shows that the orographic forcing on the precipitation record is not significant for the frontal and cyclone case, but non-negligible in the drizzle case, with the southwest wind.

The Froude number, which is a ratio of the inertial forcing against buoyant forcing, is calculated to diagnose whether the boundary layer air flow pass across the island rather than around it. The 3-D Froude numbers are commonly found to be larger than 1 from the MAC soundings from 2003 to 2010, which suggests that much of the boundary layer winds pass over the island instead of being blocked and that precipitation is most commonly enhanced in the lee of the island. Most precipitation associated with fronts and cyclones is associated with the north or northwest winds. In these cases, the MAC station is on the upwind side, so hardly affected by the orography. In the southwesterly wind cases, however, the MAC station is on the leeward side, and precipitation at the station

can be perturbed by the vertical air motion across the island. Precipitation arriving with southwesterly winds is observed in 10% of the time, which is commonly associated with low-level clouds and weak convection during cold air advection over the warmer sea surface.

While our limited evaluation process finds that the WRF simulations have captured the dominant meteorology of the four case studies, it is still possible that other important precipitation processes (e.g. embedded convection or a seeder-feeder mechanism) have not been captured. Unfortunately, there is little means to either confirm or reject the presence of these processes.

In the WRF simulations of the two frontal cases, when the winds are from the west or northwest, the orographic effects on the surface wind speeds are weak. The differences between the surface wind speeds from the simulations with and without terrain are less than 5 m s^{-1} . The wind speed differences are larger for the southwesterly winds, and the wind direction can shift 40 degrees, even when the 3-D Froude number is larger than 1. The orographic effects on the pressure and temperature are not significant.

On Macquarie Island, the current weather station is well located. The orographic effects at MAC are minimal for both the precipitation and winds for the majority of the meteorology experienced.

Looking beyond the surface station, the vertical motion triggered by terrain can enhance the warm and ice clouds over the island, when the 2-D Froude number is much greater than one. The precipitation generated by the enhanced clouds over the top of island is commonly transported to the leeward side of the island.

While, flow field blocking with 2-D Froude number much less than one is rare, but possible with weak northerly and southerly winds.

The gravity waves caused by the orography of Macquarie Island can propagate horizontally more than 100 km downwind in some cases, when the wind is strong enough ($> 15 \text{ m s}^{-1}$), which has been confirmed by airborne observations in DEEPWAVE (Fritts et al. 2015). The gravity waves can penetrate the tropopause with a vertical wind speed of 0.4 m s^{-1} . The air is lifted in a high-pressure zone on the upwind side, less than 10 km from the island, where the clouds and precipitation can be enhanced.

6.3. Future directions

The Global Precipitation Measurement (GPM) mission is the next generation of space borne observations on the precipitation over the SO, based on the Core Observatory satellite provided by NASA and JAXA (Hou et al. 2014). This satellite was launched in February 2014, to a non-Sun-synchronous orbit that covers the Earth from 65°S to 65°N . The Dual-frequency Precipitation Radar (DPR) on the satellite is more sensitive than its TRMM (Tropical Rainfall Measuring Mission; Berg et al. 2010) predecessor especially in the measurement of light rainfall and snowfall in high latitude regions. Rain/snow determination is accomplished by using the differential attenuation between the Ku-band and the Ka-band frequencies. The GPM precipitation products can be compared with those from CloudSat and the surface observations. An analysis of the GPM products could improve the climatology of the precipitation over the SO.

Adams (2009) found a 35% increase in the annual precipitation over a 38-year period from 1971-2008 over the SO, which not evident in the ERA-40 reanalysis. The annual ERA-I precipitation (953 mm) is found to underestimate the annual MAC precipitation (1023 mm) by 6.8 % from 1979 to 2011. This discrepancy cannot be explained by an orographic effect and needs to be further explored in future studies.

A strong precipitation event over Macquarie Island has been found to be independent of either fronts or cyclones, rather in the outskirts of a high-pressure system. The moisture flux from the north may contribute to this kind of strong precipitation, but the mechanism still need to be further explored.

Unmanned aerial system (UAS) observations in the planetary boundary layer over Macquarie Island in the future should avoid the gravity waves on the downwind side and the high-pressure zone on the upwind side. The case studies in Chapter 4 can provide guidance for choosing where to operate UASs around the island. Operations should avoid the downwind side during strong westerly winds, and should also be held 10 km upwind of the island, if the winds are from the north or south.

References

- Adams, N., 2009: Climate trends at Macquarie Island and expectations of future climate change in the sub-Antarctic. *Pap. Proc. Roy. Soc. Tasmania*, **143**, 1-8.
- Adler, R. F. and Coauthors, 2003: The version-2 global precipitation climatology project (GPCP) monthly precipitation analysis (1979-present). *J. Hydrometeorol.*, **4(6)**, 1147-1167.
- Ahrens, C.D., 2007: *Meteorology today: an introduction to weather, climate, and the environment. Cengage Learning*, 296.
- Bates, T. S., B. J. Huebert, J. L. Gras, F. B. Griffiths, and P. A. Durkee, 1998: International global atmospheric chemistry (IGAC) project's first aerosol characterization experiment (ACE 1): overview. *J. Geophys. Res.*, **103(D13)**, 16297-16318, doi: 10.1029/97JD03741.
- , and Coauthors, 1998: Processes controlling the distribution of aerosol particles in the lower marine boundary layer during the First Aerosol Characterization Experiment (ACE 1). *J. Geophys. Res.*, **103(D13)**, 16369-16383.
- Berg, W., T. L'Ecuyer, and J. M. Haynes, 2010: The Distribution of Rainfall over Oceans from Spaceborne Radars. *J. Climate.*, **49**, 535-543.
- Bigg, E. K., 2007: Sources, nature, and influence on climate of marine airborne particulates. *Environ. Chem.*, **4**, 155–161.
- Bennartz, R., 2007: Global assessment of marine boundary layer cloud droplet number concentration from satellite. *J. Geophys. Res.*, **112**, D02201, doi:10.1029/2006JD007547.
- Berry, G., M. J. Reeder, and C. Jakob, 2011: A global climatology of atmospheric fronts. *Geophys. Res. Lett.*, **38**, L04809, doi:10.1029/2010GL046451.
- Bodas-Salcedo, A., K. D. Williams, P. R. Field, and A. P. Lock, 2012: The surface downwelling solar radiation surplus over the Southern Ocean in the Met Office model: The role of midlatitude cyclone clouds. *J. Climate*, **25(21)**, 7467-7486.
- Boers, R., J. B. Jensen, P. B. Krummel, and H. Gerber, 1996: Microphysical and short-wave radiative structure of wintertime stratocumulus clouds over the Southern Ocean. *Q. J. Roy. Meteor. Soc.*, **122(534)**, 1307-1339.
- , and P. B. Krummel, 1998: Microphysical properties of boundary layer clouds over the Southern Ocean during ACE 1. *J. Geophys. Res.*, **103(D13)**, 16651-16663, doi: 10.1029/97JD03280.
- Brown, R.A., 1980: Longitudinal Instabilities and Secondary Flows in the Planetary Boundary Layer: A Review". *Rev. of Geophysics and Space Physics*, **18 (3)**, 683–697, doi:10.1029/RG018i003p00683.

- Browning, K. A., F. F. Hill, and C. W. Pardoe, 1974: Structure and mechanism of precipitation and the effect of orography in a wintertime warm sector. *Q. J. Roy. Meteor. Soc.*, **100(425)**, 309-330, doi: 10.1002/qj.49710042505.
- Burrows J.P., Platt U., Borrell P., 2011: The Remote Sensing of Tropospheric Composition from Space. *Springer Berlin Heidelberg*, 243.
- Catto, J. L., Jakob, C., Berry, G., and N. Nicholls, 2012: Relating global precipitation to atmospheric fronts. *Geophys. Res. Lett.*, **39(10)**, L10805, doi:10.1029/2012GL051736.
- , ——, and N. Nicholls, 2013: A global evaluation of fronts and precipitation in the ACCESS model. *Aust. Meteor. Oceanogr. J.*, **63**, 191-203.
- Charlson, R. J., J. E. Lovelock, M. O. Andreae, and S. G. Warren, 1987: Oceanic phytoplankton, atmospheric sulphur, cloud albedo and climate. *Nature*, **326(6114)**, 655-661.
- Chen, F., and J. Dudhia, 2001: Coupling an advanced land surface-hydrology model with the Penn State-NCAR MM5 modeling system. Part I: Model implementation and sensitivity. *Mon. Wea. Rev.*, **129(4)**, 569-585. doi: 10.1175/1520-0493(2001)129<0569:CAALSH>2.0.CO;2.
- Chubb, T. H., J. B. Jensen, S. T. Siems, and M. J. Manton, 2013: In situ observations of supercooled liquid clouds over the Southern Ocean during the HIAPER Pole-to-Pole Observation campaigns. *Geophys. Res. Lett.*, **40**, 5280-5285, doi:10.1002/grl.50986.
- , Y. Huang, J. B. Jensen, T. Campos, S. T. Siems and M. J. Manton, 2016: Observations of high droplet number concentrations in Southern Ocean boundary layer clouds. *Atmos. Chem. Phys.*, **16**, 971-987, doi:10.5194/acp-16-971-2016.
- Colle B. A., 2004: Sensitivity of Orographic Precipitation to Changing Ambient Conditions and Terrain Geometries: An Idealized Modeling Perspective. *J. Atmos. Sci.*, **61**, 588–606, doi: 10.1175/1520-0469(2004)061<0588:SOOPTC>2.0.CO;2.
- Dee, D., and Coauthors, 2011: The ERA-Interim reanalysis: Configuration and performance of the data assimilation system. *Quart. J. Roy. Meteor. Soc.*, **137**, 553–597, doi:10.1002/qj.828.
- Delanoë, J., and R. J. Hogan, 2010: Combined CloudSat-CALIPSOMODIS retrievals of the properties of ice clouds. *J. Geophys. Res.*, **115**, D00H29, doi:10.1029/2009JD012346.
- Ellis, T. D., T. L'Ecuyer, J. M. Haynes, and G. L. Stephens, 2009: How often does it rain over the global oceans? The perspective from CloudSat. *Geophys. Res. Lett.*, **36**, L03815, doi:10.1029/2008GL036728.
- Farr, T. G. and Coauthors, 2007: The Shuttle Radar Topography Mission, *Rev. Geophys.*, **45**, RG2004, doi:10.1029/2005RG000183.

- Facchini, M. C. and Coauthors, 2008: Primary submicron marine aerosol dominated by insoluble organic colloids and aggregates. *Geophys. Res. Lett.*, **35**, L17814.
- Franklin, C. N., Z. Sun, D. Bi, M. Dix, H. Yan, and A. Bodas-Salcedo, 2013: Evaluation of clouds in ACCESS using the satellite simulator package COSP: Global, seasonal, and regional cloud properties. *J. Geophys. Res.*, **118**, 732–748, doi:10.1029/2012JD018469.
- Fritts, D. C. and Coauthors, 2015: The Deep Propagating Gravity Wave Experiment (DEEPWAVE): An airborne and ground-based exploration of gravity wave propagation and effects from their sources throughout the lower and middle atmosphere. *Bull. Amer. Meteor. Soc.*, e-view, doi: 10.1175/BAMS-D-14-00269.1.
- Gultepe, I., and G. A. Isaac, 2004: Aircraft observations of cloud droplet number concentration: Implications for climate studies. *Q. J. Roy. Meteor. Soc.*, **130(602)**, 2377-2390.
- Gras, J. L., 1995: CN, CCN and particle size in Southern Ocean air at Cape Grim. *Atmos. Res.*, **35**, 233-251, doi:10.1016/0169-8095(94)00021-5.
- Hande, L. B., S. T. Siems, M. J. Manton, and D. Belusic, 2012: Observations of wind shear over the Southern Ocean. *J. Geophys. Res.*, **117**, D12206, doi:10.1029/2012JD017488.
- , ———, and ———, 2012: Observed trends in wind speed over the Southern Ocean. *Geophys. Res. Lett.*, **39**, L11802, doi:10.1029/2012GL051734.
- Haynes, J. M., T. S. L'Ecuyer, G. L. Stephens, S. D. Miller, C. Mitrescu, N. B. Wood, and S. Tanelli, 2009: Rainfall retrieval over the ocean with spaceborne W-band radar. *J. Geophys. Res.*, **114**, D00A22, doi:10.1029/2008JD009973.
- Hu, Y. X., and Coauthors, 2009: CALIPSO/CALIOP Cloud Phase Discrimination Algorithm. *J. Atmos. Oceanic Technol.*, **26**, 2293–2309, doi:10.1175/2009JTECHA1280.1.
- Hong, S. Y., and J. J. Lim, 2006: The WRF single-moment 6-class microphysics scheme (WSM6). *Asia-pac. J. Atmos. Sci.*, **42(2)**, 129-151.
- Hou, A.Y., and Coauthors, 2014: The global precipitation measurement mission. *Bull. Amer. Meteor. Soc.*, **95(5)**, 701-722.
- Houze, R. A. 2012: Orographic effects on precipitating clouds. *Rev. Geophys.*, **50(1)**, doi: 10.1029/2011RG000365.
- Hoskins, B. J., and K. I. Hodges, 2005: A new perspective on Southern Hemisphere storm tracks. *J. Climate*, **18(20)**, 4108-4129.
- Hu, Yongxiang and Coauthors, 2009: CALIPSO/CALIOP cloud phase discrimination algorithm. *J. Atmos. Oceanic Technol.*, **26(11)**, 2293-2309.
- Huang, Y., S. T. Siems, M. J. Manton, A. Protat, and J. Delanoë, 2012a: A study on the low-altitude clouds over the Southern Ocean using the DARDAR-MASK. *J.*

- Geophys. Res.*, **117**, D18204, doi:10.1029/2012JD017800.
- , ——, ——, L. B. Hande, and J. M. Haynes, 2012b: The Structure of Low-Altitude Clouds over the Southern Ocean as Seen by CloudSat. *J. Climate*, **25**, 2535-2546, doi:10.1175/JCLI-D-11-00131.1.
- , S. T. Siems, M. J. Manton, and G. Thompson, 2014: An Evaluation of WRF Simulations of Clouds over the Southern Ocean with A-Train Observations. *Mon. Wea. Rev.*, **142**(2), 647-667, doi: 10.1175/MWR-D-13-00128.1.
- , C. N. Franklin, S. T. Siems, M. Manton, T. Chubb, A. Lock, and A. Klekociuk, 2015: Evaluation of Boundary Layer Cloud Forecasts over the Southern Ocean in a Limited-area Numerical Weather Prediction System using In-situ, Space-borne and Ground-based Observations. *Q. J. Roy. Meteor. Soc.*, **141**(691), 2259–2276, doi: 10.1002/qj.2519.
- Hudson, J. G., Y. Xie and S. Yum, 1998: Vertical distributions of cloud condensation nuclei spectra over the summertime Southern Ocean. *J. Geophys. Res.*, **103**(D13), 16609-16624.
- and ——, 1999: Vertical distributions of cloud condensation nuclei spectra over the summertime northeast Pacific and Atlantic Oceans. *J. Geophys. Res.*, **104**(D23), 30219-30229, doi: 10.1029/1999JD900413.
- Huffman, G. J. and Coauthors, 1997: The global precipitation climatology project (GPCP) combined precipitation dataset. *Bull. Amer. Meteor. Soc.*, **78**(1), 5-20.
- Hwang, Y. T. and D. M. Frierson, 2013: Link between the double-Intertropical Convergence Zone problem and cloud biases over the Southern Ocean. *Proc. U.S. Nav. Inst.*, **110**(13), 4935-4940.
- Iacono, M. J., J. S. Delamere, E. J. Mlawer, M. W. Shephard, S. A. Clough, and W. D. Collins, 2008: Radiative forcing by long-lived greenhouse gases: Calculations with the AER radiative transfer models. *J. Geophys. Res.*, **113**(D13), doi: 10.1029/2008JD009944.
- Johansson, B., and D. Chen, 2003: The influence of wind and topography on precipitation distribution in Sweden: Statistical analysis and modelling. *Int. J. Climatol.*, **23**(12), 1523-1535, doi: 10.1002/joc.951.
- Jovanovic, B., K. Braganza, D. Collins and D. Jones, 2012: Climate variations and change evident in high-quality climate data for Australia's Antarctic and remote island weather stations. *Aust. Meteor. Oceanogr. J.*, **62**, 247-261.
- Korhonen, H. and Coauthors, 2010: Aerosol climate feedback due to decadal increases in Southern Hemisphere wind speeds. *Geophys. Res. Lett.*, **37**(2), L02805, doi:10.1029/2009GL041320.
- Jennings, S. G., M. Geever, and T. C. O'Connor, 1998: Coastal CCN measurements at Mace Head with enhanced concentrations in strong winds. *Atmos. Res.*, **46**(3), 243-252.

- Jensen, J. B., S. Lee, P. B. Krummel, J. Katzfey and D. Gogoasa, 2000: Precipitation in marine cumulus and stratocumulus.: Part I: Thermodynamic and dynamic observations of closed cell circulations and cumulus bands. *Atmos. Res.*, **54(2)**, 117-155.
- Kanitz, T., P. Seifert, A. Ansmann, R. Engelmann, D. Althausen, C. Casiccia, and E. G. Rohwer, 2011: Contrasting the impact of aerosols at northern and southern midlatitudes on heterogeneous ice formation. *Geophys. Res. Lett.*, **38(17)**, doi: 10.1029/2011GL048532.
- Kirshbaum, D. J., and D. R. Durran, 2004: Factors governing cellular convection in orographic precipitation. *J. Atmos. Sci.*, **61(6)**, 682-698, doi: 10.1175/1520-0469(2004)061<0682:FGCCIO>2.0.CO;2.
- Lebsock, M. D. and T. S. L'Ecuyer, 2011: The Retrieval of Warm Rain from CloudSat *J. Geophys. Res.*, **116**, doi:10.1029/2011JD016076.
- Lebsock, M. D., T. S. L'Ecuyer and G. L. Stephens, 2011: Detecting the ratio of rain and cloud water in low-latitude shallow marine clouds. *J. Appl. Meteor. Climatol.*, **50(2)**, 419-432.
- Leck, C. and E. K. Bigg, 2005: Evolution of the marine aerosol—a new perspective. *Geophys. Res. Lett.* **32**, L19803.
- LeMone, M., 1973: The Structure and Dynamics of Horizontal Vorticities in the Planetary Boundary Layer. *J. Atmos. Sci.*, **30 (6)**, 1077–1091, doi:10.1175/1520-0469(1973)030<1077:TSADOH>2.0.CO;2.
- Ma, L. M. and Z. M. Tan, 2009: Improving the behavior of the cumulus parameterization for tropical cyclone prediction: Convection trigger. *Atmospheric Research*, **92(2)**, 190-211.
- Mace, G. G., R. Marchand, Q. Zhang, and G. Stephens, 2007: Global hydrometeor occurrence as observed by Cloudsat: Initial observations from summer 2006, *Geophys. Res. Lett.*, **34**, L09808, doi:10.1029/ 2006GL029017.
- Mann, G. W. and Coauthors, 2010: Description and evaluation of GLOMAP-mode: a modal global aerosol microphysics model for the UKCA composition-climate model. *Geosci. Model Dev.*, **3(2)**, 519-551.
- Marchand, R. T., J. Haynes, G. G. Mace, T. Ackerman, and G. Stephens, 2009: A comparison of simulated cloud radar output from the multiscale modeling framework global climate model with CloudSat cloud radar observations, *J. Geophys. Res.*, **114**, D00A20, doi:10.1029/2008JD009790.
- Miglietta, M. M., and A. Buzzi, 2001: A numerical study of moist stratified flows over isolated topography. *Tellus A*, **53(4)**, 481-499.
- Mitrescu, C., T. L'Ecuyer, J. M. Haynes, S. D. Miller, and F. J. Turk, 2010: CloudSat Precipitation Profiling Algorithm - Model Description. *J. Appl. Meteor. and Climatol.* **49**, 991-1003, doi:10.1175/2009JAMC2181.1.

- Mlawer, E. J., S. J. Taubman, P. D. Brown, M. J. Iacono, and S. A. Clough, 1997: Radiative transfer for inhomogeneous atmospheres: RRTM, a validated correlated-k model for the longwave. *J. Geophys. Res.*, **102(D14)**, 16663-16682, doi: 10.1029/97JD00237.
- Moncrieff, M. W., D. E. Waliser, M. J. Miller, M. A. Shapiro, G. R. Asrar, and J. Caughey, 2012: Multiscale convective organization and the YOTC virtual global field campaign. *Bull. Amer. Meteor. Soc.*, **93(8)**, 1171-1187, doi: 10.1175/BAMS-D-11-00233.1.
- Morrison, A. E., S. T. Siems, M. J. Manton, and A. Nazarov, 2010: A modeling case study of mixed-phase clouds over the Southern Ocean and Tasmania. *Mon. Wea. Rev.*, **138(3)**, 839-862, doi: 10.1175/2009MWR3011.1.
- , ———, ———, 2011: A Three-Year Climatology of Cloud-Top Phase over the Southern Ocean and North Pacific. *J. Climate*, **24**, 2405-2418, doi:10.1175/2010JCLI3842.1.
- Murphy, D. M., and Coauthors, 1998: Influence of sea-salt on aerosol radiative properties in the Southern Ocean marine boundary layer. *Nature*, **392**, 62-65, doi:10.1038/32138.
- Naud, C.M., D.J. Posselt, and S.C. van den Heever, 2012: Observational analysis of cloud and precipitation in midlatitude cyclones: Northern versus southern hemisphere warm fronts. *J. Climate*, **25**, 5135-5151, doi:10.1175/JCLI-D-11-00569.1.
- Nugent, A. D., R. B. Smith and J. R. Minder, 2014: Wind speed control of tropical orographic convection. *J. Atmos. Sci.*, **71(7)**, 2695-2712.
- O'Dowd and Coauthors, 2004: Biogenically driven organic contribution to marine aerosol. *Nature*, **431(7009)**: 676-680.
- Pfeifroth, U., R. Mueller, and B. Ahrens, 2013: Evaluation of Satellite-Based and Reanalysis Precipitation Data in the Tropical Pacific. *J. Appl. Meteor. Climatol*, **52**, 634-644, doi: 10.1175/JAMC-D-12-049.1.
- Platnick, S., M. D. King, S. A. Ackerman, W. P. Menzel, B. A. Baum, J. C. Riedi, R. and A. Frey, 2003: The MODIS cloud products: Algorithms and examples from Terra, *IEEE Trans. Geosci. Remote Sens.*, **41(2)**, 459-473.
- Quinn, P. K., and T.S. Bates, 2011: The case against climate regulation via oceanic phytoplankton sulphur emissions. *Nature*, **480(7375)**, 51-56.
- Rasmussen, R. M., P. Smolarkiewicz, and J. Warner, 1989: On the dynamics of Hawaiian cloud bands: Comparison of model results with observations and island climatology. *J. Atmos. Sci.*, **46(11)**, 1589-1608, doi: 10.1175/1520-0469(1989)046<1589:OTDOHC>2.0.CO;2.
- , I. Geresdi, G. Thompson, K. Manning and E. Karplus, 2002: Freezing drizzle formation in stably stratified layer clouds: The role of radiative cooling of cloud droplets, cloud condensation nuclei, and ice initiation. *J. Atmos. Sci.*, **59(4)**, 837-860.

- Rienecker, M. M. and Coauthors, 2011: MERRA: NASA's modern-era retrospective analysis for research and applications. *J. Climate*, **24(14)**, 3624-3648.
- Rosenfeld, D. and Coauthors, 2013: The common occurrence of highly supercooled drizzle and rain near the coastal regions of the western United States. *J. Geophys. Res.*, **(118)17**, 9819-9833.
- Russell, L.M. and Coauthors, 1998: Bidirectional mixing in an ACE 1 marine boundary layer overlain by a second turbulent layer. *J. Geophys. Res.*, **103(D13)**, 16411-16432.
- Ryan B. F. and K. J. Wilson, 1985: The Australian Summertime Cool Change. Part III: Subsynoptic and Mesoscale Model. *Mon. Wea. Rev.*, **113**, 224–240, doi: 10.1175/1520-0493(1985)113<0224:TASCCP>2.0.CO;2.
- , and W. D. King, 1997: A critical review of the Australian experience in cloud seeding. *Bull. Amer. Meteor. Soc.*, **78(2)**, 239-254.
- Schär, C., and D. R. Durran, 1997: Vortex formation and vortex shedding in continuously stratified flows past isolated topography. *J. Atmos. Sci.*, **54(4)**, 534-554, doi: 10.1175/1520-0469(1997)054<0534:VFAVSI>2.0.CO;2.
- Stephens, G. L., and Coauthors, 2002: The CloudSat mission and the A-Train. *Bull. Amer. Meteor. Soc.*, **83**, 1771-1990, doi:10.1175/BAMS-83-12-1771.
- , T. L'Ecuyer, R. Forbes, A. Gettleman, J.-C. Golaz, A. Bodas-Salcedo, K. Suzuki, P. Gabriel, and J. Haynes, 2010: Dreary state of precipitation in global models. *J. Geophys. Res.*, **115**, D24211, doi:10.1029/2010JD014532.
- Simmonds, I., and K. Keay, 2000: Mean Southern Hemisphere extratropical cyclone behavior in the 40-year NCEP-NCAR reanalysis. *J. Climate*, **13(5)**, 873-885, doi: 10.1175/1520-0442(2000)013<0873:MSHECB>2.0.CO;2.
- Skamarock, W. C., and J. B. Klemp, 2008: A time-split nonhydrostatic atmospheric model for weather research and forecasting applications. *J. Comput. Phys.*, **227(7)**, 3465-3485, doi: 10.1016/j.jcp.2007.01.037.
- Smith, R. B. 1979: The influence of mountains on the atmosphere. *Adv. Geophys.*, **21**, 87-230.
- , 1989: Hydrostatic airflow over mountains. *Adv. Geophys.*, **31**, Academic Press, 1–41.
- Smolarkiewicz, P. K., R. M. Rasmussen, and T. L. Clark, 1988: On the dynamics of Hawaiian cloud bands: Island forcing. *J. Atmos. Sci.*, **45(13)**, 1872-1905, doi: 10.1175/1520-0469(1988)045<1872:OTDOHC>2.0.CO;2.
- , and R. Rotunno, 1989: Low Froude number flow past three-dimensional obstacles. Part I: Baroclinically generated lee vortices. *J. Atmos. Sci.*, **46(8)**, 1154-1164, doi: 10.1175/1520-0469(1989)046<1154:LFNFPT>2.0.CO;2.

- Spracklen, D. V., K. J. Pringle, K. S. Carslaw, M. P. Chipperfield and G. W. Mann, 2005: A global off-line model of size-resolved aerosol microphysics: I. Model development and prediction of aerosol properties. *Atmos. Chem. Phys. Discuss.*, **5(1)**, 179-215.
- Streten, N. A. 1988: The climate of Macquarie Island and its role in atmospheric monitoring. *Pap. Proc. Roy. Soc. Tasmania*, **122 (1)**, 91-106.
- Thompson, G., P. R. Field, R. M. Rasmussen, and W. D. Hall, 2008: Explicit forecasts of winter precipitation using an improved bulk microphysics scheme. Part II: Implementation of a new snow parameterization. *Mon. Wea. Rev.*, **136(12)**, 5095-5115, doi: 10.1175/2008MWR2387.1.
- Trenberth, K. E., 1991: Storm tracks in the Southern Hemisphere. *J. Atmos. Sci.*, **48(19)**, 2159-2178.
- , and J. T. Fasullo, 2010: Simulation of present-day and twenty-first-century energy budgets of the southern oceans. *J. Climate*, **23**, 440-454, doi:10.1175/2009JCLI3152.1.
- Tsukernik, M., and A. H. Lynch, 2013: Atmospheric Meridional Moisture Flux over the Southern Ocean: A Story of the Amundsen Sea. *J. Climate*, **26**, 8055-8064, doi:10.1175/JCLI-D-12-00381.1.
- Uppala, S.M. and Coauthors, 2005: The ERA-40 re-analysis. *Q. J. Roy. Meteor. Soc.*, **131(612)**, 2961-3012.
- Vinoth, J., and I. R. Young, 2011: Global estimates of extreme wind speed and wave height, *J. Climate*, **24(6)**, 1647–1665, doi:10.1175/2010JCLI3680.1.
- Wang, Z., S. Siems, D. Belusic, M. Manton and Y. Huang, 2015: A Climatology of the Precipitation over the Southern Ocean as observed at Macquarie Island. *J. Appl. Meteor. Climatol.*, **54**, 2321–2337, doi: 10.1175/JAMC-D-14-0211.1.
- Watson, C. D. and T. P. Lane, 2012: Sensitivities of Orographic Precipitation to Terrain Geometry and Upstream Conditions in Idealized Simulations. *J. Atmos. Sci.*, **69**, 1208–1231, doi: 10.1175/JAS-D-11-0198.1.
- Wofsy, S. C., 2011: HIAPER Pole-to-Pole Observations (HIPPO): fine-grained, global-scale measurements of climatically important atmospheric gases and aerosols. *Philos. Trans. A. Math. Phys. Eng. Sci.*, **369(1943)**, 2073-2086, doi: 10.1098/rsta.2010.0313.
- Wyngaard, J. C., 2004: Toward numerical modeling in the “Terra Incognita”. *J. Atmos. Sci.*, **61(14)**, 1816-1826. doi: 10.1175/1520-0469(2004)061<1816:TNMITT>2.0.CO;2.
- Yuan, J. and R. L. Miller, 2002: Seasonal variation in precipitation patterns to the global ocean: An analysis of the GPCP version 2 data set. *Global Biogeochem. Cycles.*, **16(4)**, 1103, doi:10.1029/2001GB001458, 2002.

Yum, S. S. and J. G. Hudson, 2004: Wintertime/summertime contrasts of cloud condensation nuclei and cloud microphysics over the Southern Ocean. *J. Geophys. Res.*, **109**, D06204, doi:10.1029/2003JD003864.

Zhang, X. and Y. Feng, 2004: RCLimDex User Manual. <http://cccma.seos.uvic.ca/ETCCDMI/RCLimDex/RCLimDexUserManual.doc>.